

Ellipsometric Determination of Cation Disorder in Magnetically Ordered Spinel Ferrite Thin Films

Der Fakultät für Physik und Geowissenschaften
der Universität Leipzig
genehmigte

DISSERTATION

zur Erlangung des akademischen Grades
Doctor rerum naturalium
Dr. rer. nat.



vorgelegt von
M. Sc. Vitaly Zviagin
geboren am 23. Dezember 1989 in Kharkiv, Ukraine

Gutachter: Prof. Dr. Marius Grundmann (Universität Leipzig)
Dr. Stefan Zollner (New Mexico State University)

Tag der Verleihung: 08.07.2019

Bibliographische Beschreibung:

Zviagin, Vitaly

Ellipsometric Determination of Cation Disorder in Magnetically Ordered Spinel Ferrite Thin Films

Universität Leipzig, Dissertation

140 S., 199 Lit., 55 Abb., 8 Tab.

Referat:

In dieser Arbeit wird die kationische Verteilung in der Spinel-Ferrite-Struktur im Zusammenhang mit magnetischen Eigenschaften spektroskopisch untersucht. Die Ferrite-Dünnschichten wurden mit gepulster Laserabscheidung bei verschiedenen Züchtungstemperaturen und Atmosphären hergestellt und nachfolgend thermisch behandelt. Die strukturellen Eigenschaften werden mit verschiedenen Methoden untersucht, um Information zur Kristallografischen Qualität zu erhalten. Die dielektrische Funktion wird mittels empirisch gewählten analytischen Funktionen modelliert und zeigt elektronische Übergänge zwischen d-Orbitalen der Fe^{2+} -Kationen und Übergänge von Sauerstoff 2p zu Eisen und Zink 3d und 4s-Orbitalen. Die magneto-optischen Eigenschaften bestätigen die Zuordnung der festgestellten Übergänge, die lokaler kationischer Unordnung und Inversion zugeordnet werden können.

Mit zunehmender Züchtungstemperatur wird die magnetische Antwort niedriger. Die Abnahme der ferrimagnetischen Ordnung wird mit der Abnahme der Oszillator-Stärke von den Übergängen, die tetraedrische Fe^{3+} -Kationen involvieren, korreliert. Durch Ausheizen in Argon bei Temperaturen, die niedriger als die Züchtungstemperatur sind, steigt die magnetische Ordnung, was durch Sauerstoff-Vakanzen erklärt werden kann. Bei höheren thermischen Behandlungstemperaturen wird spektroskopisch eine Umkristallisation der ionischen Verteilung festgestellt und zu der entsprechenden Abnahme der Stärke der magnetischen Antwort korreliert.

Die kationische Verteilung in der Oberfläche und im gesamten Dünnfilm wird anhand von XPS- und dielektrische Funktion-Spektren als Funktion der Zink-Konzentration untersucht. Der Unterschied in der Konfigurationsverteilung in Dünnfilmen, die hauptsächlich in der inversen Konfiguration auftreten zu Dünnfilmen in normaler Spinel-Struktur, drückt sich in einer schwächeren magnetischen Ordnung aus. Unsere Ergebnisse zeigen eine mögliche defektreiche Konfiguration in der Oberfläche, die in den normalen Spinelen zu einer stärkeren magnetischen Ordnung führt. In Zusammenhang mit strukturellen Untersuchungsmethoden wird die kationische Unordnung mit den magnetischen Eigenschaften korreliert und durch Analyse der dielektrischen Funktion bestätigt.

Bibliographic Record:

Zviagin, Vitaly

Ellipsometric Determination of Cation Disorder in Magnetically Ordered Spinel Ferrite Thin Films

Universität Leipzig, Dissertation

140 pp., 199 refs., 55 figs., 8 tabs.

Abstract:

In this investigation, the cation distribution in ferrites of spinel-type structure is spectroscopically investigated with respect to the observed magnetic behavior. The ferrite thin films were fabricated by pulsed laser deposition and consequently annealed at different temperatures as well as atmospheres. Structural properties were determined with various methods and the crystalline quality was examined. The dielectric function line-shape was parametrized based on empirical evidence and was found to be dominated by electronic transitions between d orbitals of Fe^{2+} cations as well as transitions from O 2p to 3d and 4s orbitals of iron and zinc cations. The strongest magneto-optical response was observed for transitions involving cations, which correspond to lattice disorder and inversion within the normal spinel structure.

With the decrease in the substrate temperature during fabrication, a decrease in the magnetic response was observed. The diminishing ferrimagnetic order was directly correlated to the decrease in strength of the transitions, involving Fe^{3+} on tetrahedral lattice sites. After thermal treatment in argon atmosphere and at a temperature below the deposition temperature, the increase in the magnetic response was explained through the facilitation of oxygen vacancies. With the increase in treatment temperature, a decrease in ferrimagnetic order was related to the recrystallization of the disordered spinel structure toward a more stable normal configuration, evident in the dielectric function spectra.

The cationic configuration distribution in the surface as well as the bulk region, as a function of Zn concentration, was determined from approximation of the XPS and the dielectric function spectra, respectively. The difference in the cation configuration distribution, in films of predominantly inverse configuration, was related to the weak magnetic response, as opposed to films of predominantly normal spinel configuration. Our results demonstrate that a defect-rich surface region could serve as a possible explanation for the ferrimagnetic order in a nominally non-magnetic normal spinel ZnFe_2O_4 . In combination with structural property determination, the net magnetic behavior is explained through the local cationic disorder, determined from the parametrization of the dielectric function spectra in a wide spectral range.

"If we knew what it was we were doing, it would not be called research."

Albert Einstein

Contents

1	Introduction	1
2	Theoretical background and fundamental considerations	5
2.1	Spinel ferrite crystal structure	5
2.2	Crystal field stabilization energy	8
2.3	Band structure description	11
2.4	Verwey transition	14
2.5	Magnetic exchange interactions	15
3	Sample preparation and modification	19
3.1	Macroscopic spinel film formation	19
3.2	Pulsed laser deposition	27
3.3	Thermal treatment	29
3.4	Sample overview	30
4	Methods and general properties	31
4.1	Structure characterization techniques	31
4.1.1	X-ray diffraction	31
4.1.2	X-ray reflectivity	33
4.1.3	Energy dispersive X-ray spectroscopy	35
4.1.4	Focused ion beam and scanning electron microscopy	36
4.1.5	Raman spectroscopy	37
4.2	Surface properties	39
4.2.1	Atomic force microscopy	39
4.2.2	X-ray photoelectron spectroscopy	41
4.3	Dielectric tensor properties	45
4.4	Spectroscopic ellipsometry	51
4.5	Magneto-optical Kerr effect	60
4.6	Magneto-static properties	66

CONTENTS

5	Results and discussion	71
5.1	Magnetic and optical properties of Fe_3O_4 thin film and single crystal	72
5.2	Magneto-optical properties of $\text{Zn}_x\text{Fe}_{3-x}\text{O}_4$ thin films	78
5.3	Fabrication temperature dependent ferrimagnetic order	83
5.4	Thermally induced structural stabilization	89
5.5	Cation configuration in dependence on the Zn concentration . . .	98
5.5.1	Structural property determination	98
5.5.2	Composition characterization	102
5.5.3	Magneto-static behavior	106
5.5.4	Section summary and discussion	110
6	Summary and outlook	113
	Bibliography	117
	List of article contributions	137
	Selbstständigkeitserklärung	139
	Acknowledgments	141

Chapter 1

Introduction

Iron oxides, ferrites, are well integrated in the geochemistry of our ecosystem [1]. Interestingly, the existence of haematite (α - Fe_2O_3) has been confirmed on Mars by the Curiosity rover [2]. On Earth, magnetite (Fe_3O_4) arguably aids the navigation of birds and is found in their beak as well as in the human brain and other body tissue [3–5]. The application of magnetite for navigation purposes dates back as early as 200 BC China. In the 20th century, one of the first metal-insulator transitions was discovered in magnetite by Verwey in 1939 [6]. Fe_3O_4 was further used by Néel as a prototype material to demonstrate the theory of ferrimagnetism [7].

Today, the versatility of tunable properties can be realized through the optimization of synthetic fabrication [8]. The diversity of ion configurations makes transition metal oxides, MFe_2O_4 (where M is the divalent cation), uniquely suitable for a vast scope of applications. For example, remarkable optoelectronic tunability, high thermal and chemical stability enables photoanode application for solar water oxidation [9–12]. Excellent electrochemical properties and reversible magnetization has advanced the design of novel Li-ion controlled electronic devices [13–16]. Recently, simultaneous detection and treatment of cancer cells by magnetic hyperthermia has been realized through drug delivery and heat generation with the aid of a franklinite (ZnFe_2O_4) nanoparticle [17–21]. Preparation of such theranostic systems was achieved by utilizing surface adsorption and superparamagnetic nature of biocompatible ferrite nanoparticles. Furthermore, the predicted 100% spin polarization of the conduction electrons at the Fermi level makes magnetite an outstanding candidate for design of next-generation complex spintronic devices [22–27]. Volatile structure-property relationship makes ternary spinel ferrite an exceptional archetype material system with a vast operational potential. However, efforts to precisely fabricate and determine the ionic distri-

1. Introduction

bution in relation to their physical properties remain technically challenging. In this work, a direct correlation between fabrication (thermal treatment) parameters and spectroscopically determined cationic distribution in ferrite thin films of inverse, disordered and normal spinel configuration is presented with respect to the overall magnetic behavior.

ZnFe_2O_4 is considered to be antiferromagnetic with a Néel temperature of 10 K and crystallizes in a normal spinel structure, where Zn^{2+} and Fe^{3+} cations occupy tetrahedral and octahedral lattice site, respectively [28]. The oxygen mediated super-exchange interaction between two octahedral Fe^{3+} cations allows antiferromagnetic coupling. However, the presence of intrinsic defects, such as oxygen vacancies and tetrahedrally coordinated Fe^{3+} cations alter magnetic interactions, giving rise to spontaneous magnetization at room temperature [29,30]. Previous studies have demonstrated the presence of tetrahedral Fe^{3+} to strongly contribute to the overall magnetic behavior due to the dominant strength of the oxygen mediated super-exchange interaction between Fe^{3+} cations on the two lattice sites [31–34]. Presence of oxygen vacancies was shown to change the interaction between octahedral Fe^{3+} cations from antiferromagnetic to ferromagnetic, thereby influencing the total magnetic response [35]. Furthermore, a lack of long-range order at low temperatures was demonstrated by neutron scattering in a single crystal sample [36]. This contradicts the observed temperature dependent magnetization, which displays the magnetic character either of a spin glass or a superparamagnetic system [19,21,25,37–39]. The distribution of tetrahedral Fe^{3+} cations in the surface region is argued to strongly influence this behavior, however their magnetic contribution is yet to be thoroughly investigated [37,40–42]. Magnetite, Fe_3O_4 , on the other hand, crystallizes in an inverse spinel configuration and exhibits ferrimagnetic order. The overall magnetic moment would arise only from the octahedral Fe^{2+} cations, as the moments of octahedral and tetrahedral Fe^{3+} cations are compensated. However, the double-exchange interaction between octahedrally coordinated Fe^{2+} and Fe^{3+} cations would also contribute to the overall magnetic response and give rise to electrical conductivity, where both would diminish below the Verwey transition temperature [43]. The presence of macroscopic defects, such as antiphase boundaries, has shown to be the main culprit of the low magnetic response in magnetite and the deviation of the surface cation distribution from that of the bulk [8,44–47]. The effect of local crystallographic disorder as well as cation configuration distribution within the thin film structure on the overall magnetic behavior is yet to be fully understood and experimentally demonstrated.

The research on ZnFe_2O_4 thin films at Universität Leipzig serves as foundation for this investigation. The dependence of dielectric function line-shape on deposition temperature was presented, however a deeper understanding of mechanisms behind this behavior remained unclear [48]. Electrical conductivity in ZnFe_2O_4 films was related to the presence of Fe^{2+} cations and showed an increase with the decrease in oxygen partial pressure during fabrication [49]. The surface composition of spinel ferrite films was shown to depend strongly on the cations of tetrahedral coordination, however, the approach to quantify the relative cation content is yet to be developed [50]. The growth of epitaxial, atomically smooth, heteroepitaxial TiN thin films on (100) MgO single crystals was optimized and used as substrates for the $\text{Zn}_x\text{Fe}_{3-x}\text{O}_4$ thin film fabrication [51]. The fabrication of ZnFe_2O_4 thin films on SrTiO_3 substrates by pulsed laser deposition was previously optimized to obtain epitaxial films of high quality [52]. Theoretical calculations were previously conducted at the Martin-Luther University of Halle-Wittenberg for similar ZnFe_2O_4 structures in cooperation with Universität Leipzig [35]. The influence of individual local defect on the induced magnetic response was investigated to show the dominance of oxygen vacancies over cation disorder, experimental determination of which is yet to be explicitly demonstrated.

In this work, spinel ferrite ($\text{Zn}_x\text{Fe}_{3-x}\text{O}_4$ with $0 \leq x \leq 1.26$) thin films were fabricated on MgAl_2O_4 , MgO, SrTiO_3 and TiN/MgO substrates by pulsed laser deposition. By varying the deposition and thermal treatment environment, ferrite films of configuration ranging from inverse to disordered and normal spinel were achieved. Energy dispersive X-ray (EDX) spectroscopy was applied to verify the material composition. The crystallinity was analyzed by X-ray diffraction (XRD) as well as Raman spectroscopy. Physical surface and bulk structure was examined by atomic force microscopy (AFM) and scanning electron microscopy (SEM), respectively. The chemical composition was approximated by individual cation contribution to the X-ray photoelectron spectroscopy (XPS) Fe 2p, 3p and Zn 2p core level surface spectra as well as to the bulk diagonal elements of the dielectric tensor, obtained by spectroscopic ellipsometry. A parametric model for the dielectric function (DF) was developed in the spectral range from 0.5 to 8.5 eV. The DF spectra was found to be dominated by optical transitions between d orbitals of Fe^{2+} (≤ 1 eV) and transitions from O 2p to Fe and Zn 3d and 4s orbitals (≥ 2 eV). Magnetically active transitions were correlated to transitions visible in the off-diagonal elements of the dielectric tensor, determined by magneto-optical Kerr effect (MOKE). Structural defects in normal spinel,

1. Introduction

such as tetrahedral Fe^{3+} and octahedral Fe^{2+} , were evident from the strength of electronic transitions in DF spectra and showed a strong dependence on the substrate temperature and oxygen pressure, respectively. While tetrahedral Fe^{3+} were due to either inversion mechanism or occupation of previously unoccupied sites, the presence of Fe^{2+} was partially due to oxygen vacancies. Valence- and site-specific cation composition in the film bulk and surface was examined as a function of Zn concentration. The defects were found to contribute to the competing ferromagnetic and antiferromagnetic interactions and were correlated to the overall magnetic response, determined by vibrating sample magnetometry (VSM) as well as superconducting quantum interference device (SQUID).

The investigated ZnFe_2O_4 and $\text{Zn}_x\text{Fe}_{3-x}\text{O}_4$ thin films were deposited by H. Hochmuth and M. Bonholzer, respectively, using targets, prepared by G. Ramm. Prior to deposition, the substrate was treated by M. Hahn. EDX and SEM measurements were conducted by J. Lenzner. Raman spectra were recorded by C. Sturm. The XPS spectra of the $\text{Zn}_x\text{Fe}_{3-x}\text{O}_4$ thin films were recorded and the spectra approximation was conducted by P. Huth of Prof. Dr. R. Denecke group in the Wilhelm Ostwald Institute for Physical and Theoretical Chemistry. The MOKE spectra were recorded and data analysis was conducted by P. Richter and A. Sharma of Prof. Dr. D.R.T. Zahn, Semiconductor Physics Group in the Technical University of Chemnitz. The Fe_3O_4 thin film was prepared by M. Ziese and the SQUID measurements were conducted by A. Setzer of Prof. Dr. P. Esquinazi, Superconductivity and Magnetism Group.

Chapter 2

Theoretical background and fundamental considerations

The vast range of intrinsic properties, which continue to make spinel ferrite an attractive material for applications, is attributed to the diversity of possible ion configurations. However, the phenomena behind the preferred crystallographic ground state formation remains controversial. In this chapter, the local crystallographic structures, that assemble the investigated thin films, are presented. The fundamental origin behind the physical properties is related to the preferential cation allocation within the spinel lattice.

2.1 Spinel ferrite crystal structure

The first determination of spinel crystal structure dates back to the first application of the X-ray diffraction technique to investigate the crystallinity of magnetite [56]. Spinel type oxides have a chemical formula of AB_2O_4 , where A and B designate divalent and trivalent cations, respectively. Most spinel compounds, as in our case $ZnFe_2O_4$, belong to the cubic space group $Fd\bar{3}m$ (No. 227) and crystallize in the same structure as the parent mineral compound $MgAl_2O_4$. The crystal structure can be interpreted in terms of cubic close packed arrays of anions with $ABCABC\dots$ stacking [57]. As the O^{2-} ionic radius (~ 0.14 nm) is much larger than that of Fe^{2+} (~ 0.082 nm), Fe^{3+} (~ 0.065 nm) and Zn^{2+} (~ 0.074 nm) cations, the crystallinity of the structure is strongly dependent on the anion arrangement [1]. The intersites between the anion arrays are either of octahedral or tetrahedral coordination and contain cations, which act as bonding elements between the anion sheets. Ideally, 8 out of 64 tetrahedral and 16 out of 32 octahedral lattice sites are occupied in the face-centered cubic (fcc) unit [58]. Depending

2.1. Spinel ferrite crystal structure

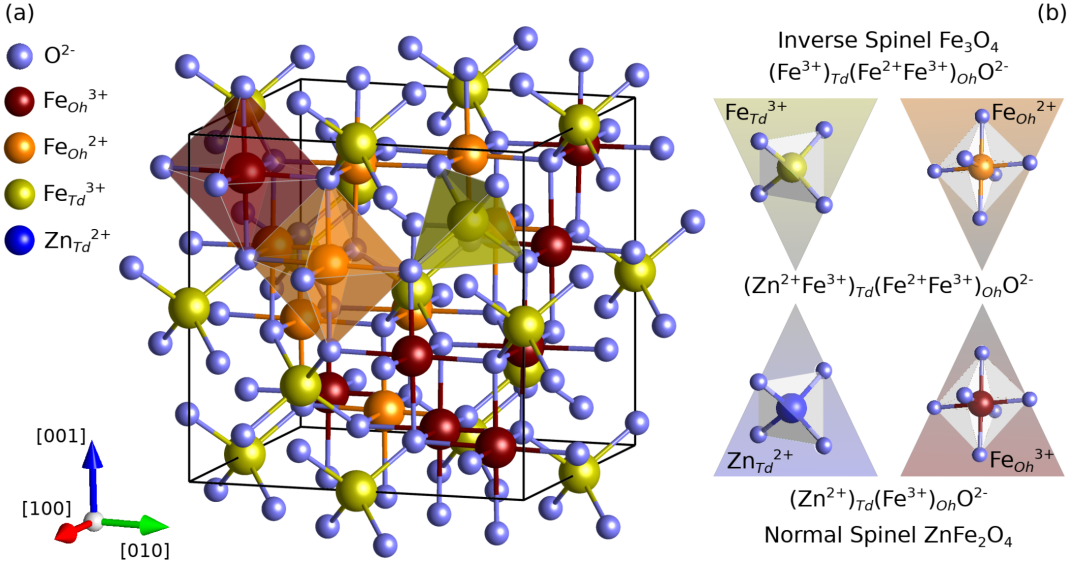


Figure 2.1: (a) The cubic crystal structure of the inverse spinel Fe_3O_4 , imported from [53]. (b) Depiction of tetrahedral (Td) Fe^{3+} (green), Zn^{2+} (blue) and octahedral (Oh) Fe^{2+} (orange), and Fe^{3+} (red) cations, coordinated by O^{2-} (purple) anions, as well as cation distribution formula for the inverse spinel Fe_3O_4 (top), containing only Fe_{Td}^{3+} and Fe_{Oh}^{2+} , disordered (middle) and normal spinel ZnFe_2O_4 (bottom), containing Zn_{Td}^{2+} and Fe_{Oh}^{3+} cations. Crystallographic images were modified using VESTA [54] and edited using Inkscape software [55].

on divalent or trivalent cation allocation among the two lattice sites, a spinel of either normal or inverse configuration is formed.

A lattice of normal spinel AB_2O_4 configuration contains divalent (A) and trivalent (B) cations on tetrahedral and octahedral interstitial sites, hereinafter also referred to as Td and Oh , respectively. In the spinel structure of inverse configuration, the divalent cations occupy the octahedral lattice sites, while the trivalent cations are distributed evenly over both sites. Therefore, a conventional notation for the cation distribution formula with respect to the inversion parameter (λ) is given by

$$(A_{1-\lambda}B_\lambda)_{Td}(A_\lambda B_{2-\lambda})_{Oh}O_4^{2-} \quad (2.1)$$

In our case, $\text{Zn}^{2+}\text{Fe}_2^{3+}\text{O}_4$ ideally crystallizes in a normal configuration. Magnetite ($\text{Fe}^{2+}\text{Fe}_2^{3+}\text{O}_4$), on the other hand, crystallizes in an inverse spinel configuration and is schematically depicted in Figure 2.1(a). Therefore, the equilibrium state of the spinel lattice, as a function of Zn concentration (x), is expected to assemble in the following cation configuration

$$(\text{Zn}_x^{2+}\text{Fe}_{1-x}^{3+})_{Td}(\text{Fe}_{1+x}^{3+}\text{Fe}_{1-x}^{2+})_{Oh}O_4^{2-} \quad (2.2)$$

2.1. Spinel ferrite crystal structure

where $x = 0$ and 1 would correspond to the inverse Fe_3O_4 and normal spinel ZnFe_2O_4 structure, respectively. The cation distribution formula for the structure, evolving from inverse to normal, with a decrease in Fe_{Td}^{3+} and Fe_{Oh}^{2+} and increase in Zn_{Td}^{2+} , is depicted in Figure 2.1(b). More information about the spinel ferrite structure can be found at [1] and [28]. Furthermore, the molecular structure with basic band structure calculations and their details can be found at [53]. The mechanism behind cation allocation within the lattice as well as the relation to the band structure is revealed below.

2.2 Crystal field stabilization energy

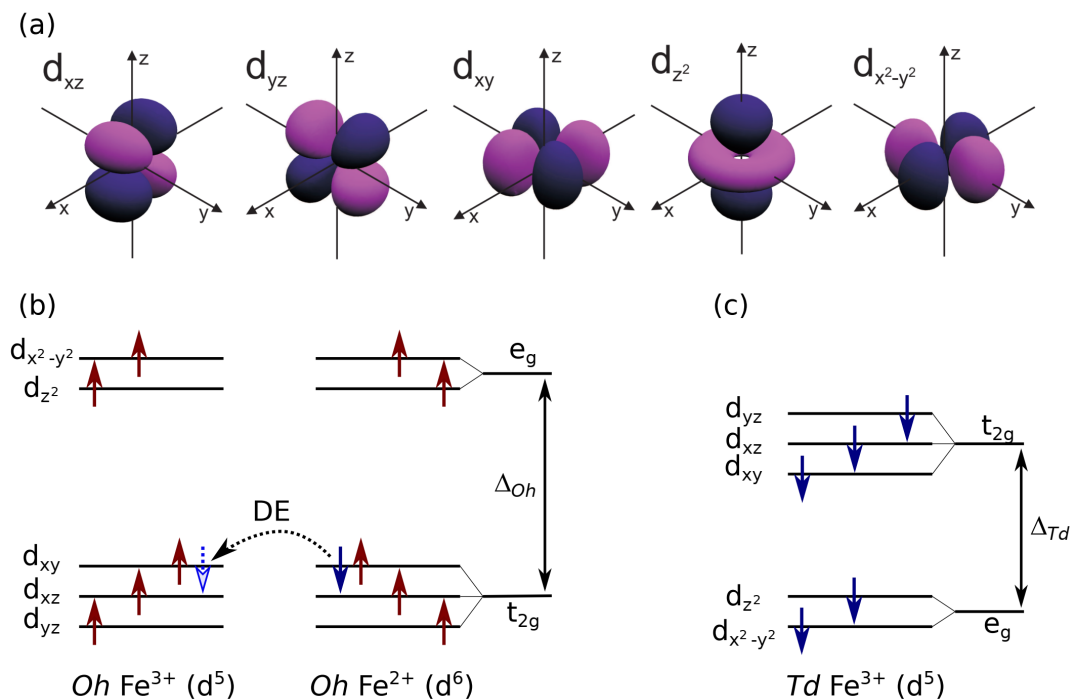


Figure 2.2: (a) Orbital configurations of electrons in the d orbital, for $n = 3$, $l = 2$ and $m = -1$ (d_{xz}), 1 (d_{yz}), 2 (d_{xy}), -2 ($d_{x^2-y^2}$), 0 (d_{z^2}). Sketch redrawn after [59]. Schematic representation of electron occupation of (b) octahedral (Oh) Fe^{2+} and Fe^{3+} as well as (c) tetrahedral (Td) Fe^{3+} 3d states in Fe_3O_4 with symmetry states separated by Δ_{Td} as well as Δ_{Oh} , respectively. Individual d levels in each t_{2g} and e_g symmetry state have been shifted for clarity. The spin down electron on the t_{2g} state is coupled antiparallel to the local moment formed by spin up electrons and can hop between orbitals of the Fe^{2+} and Fe^{3+} cations, giving rise to electrical conductivity.

The classical approach to distinguish between normal and inverse spinel configuration is by the crystal field stabilization energy (CFSE). This approach correlates the type of local structure sites with the excess orbital energy, as a result of the d atomic orbital energies by non-spherical crystal field [60]. As in our case, this approach is applicable to a structure, which contains open shell transition metal cations.

The ground state of the spinel lattice structure is defined by the cation distribution over tetrahedral and octahedral sites. Based on the ligand theory, the cation arrangement is dependent on the CFSE. It describes the energy which results from an ion being placed in a set of ligand atoms and depends on the number of electrons in the d orbital, listed in Table 2.1. In response to the charge

2.2. Crystal field stabilization energy

distribution, due to the surrounding anions, the five d orbital states, depicted in Figure 2.2(a), are split into two sets. In the octahedral symmetry, the three orbital states, d_{xz} , d_{yz} and d_{xy} , will be lower in energy than the two $d_{x^2-y^2}$ and d_{z^2} states, Figure 2.2(b). While the former set is denoted as the t_{2g} orbital, the latter is the e_g orbital. The orbital states in the tetrahedral symmetry, Figure 2.2(c), however, are reversed and the crystal field energy between the two orbital states is lower than for the octahedral symmetry ($\Delta_{Td} < \Delta_{Oh}$) [61]. The energy by which the two orbitals are split is known as the crystal field parameter (Δ_{Oh} , Δ_{Td}). It is commonly expressed in terms of Dq , which is related to the radial electron density of the d electrons, their charge and distance to the surrounding anions.

A simplified sketch for orbital states of 3d tetrahedral and octahedral Fe cation states in Fe_3O_4 are illustrated in Figure 2.2(b) and (c). The 3d band of the Fe_{Oh}^{2+} cation contains 6 d electrons, where 5 electrons occupy the spin up state and the 6th is in the spin down state. The spin down electron in the t_{2g} orbital can hop between Fe^{2+} and Fe^{3+} cation orbitals. The mechanism gives rise for the double exchange (DE) magnetic interaction and is responsible for electrical conductivity in magnetite. Due to 4 unpaired electrons in the 3d orbital, the Fe^{2+} cation has a net magnetic moment of $4\mu_B$. The term $\mu_B = \frac{e\hbar}{2m_e}$ is the Bohr magneton magnetic moment unit, where e , m_e and \hbar is the elementary charge, electron mass and reduced Planck constant, respectively. The Fe^{3+} cation, however, has 5 unpaired electrons that occupy the majority states only, and exhibits a net magnetic moment of $5\mu_B$, listed in Table 2.1.

At this point, we would like to note that while the large CFSE of Fe^{2+} cations would correspond to their octahedral sublattice occupation, some studies have also shown tetrahedral occupation [62]. Whether Fe^{2+} controversially occupies tetrahedral sites is not addressed within the scope of this investigation and octahedral Fe^{2+} occupation is assumed. Furthermore, Fe^{3+} and Zn^{2+} cations are known to have no preference over sublattice occupation, $\text{CFSE} = 0$, Table 2.1. Therefore, both cations can occupy both tetrahedral and octahedral lattice sites. The cation distribution formula, depicted in Figure 2.1(b), is possible in a normal spinel ZnFe_2O_4 where cation inversion is present.

The classical approach to distinguish between normal and inverse spinel configuration is the CFSE, described above. Based on the ion-ion contributions to the total energy of the structure, quantitative rationalization for the cation arrangements is commonly made. Nevertheless, due to the complexity of the structures, the cation redistribution in the ground state is not as straightforward and alter-

2.2. Crystal field stabilization energy

Table 2.1: Orbital set notation, magnetic moment in terms of μ_B and CFSE, given in Dq , for ions with d electron configuration of octahedral (Oh) and tetrahedral (Td) coordination. The table was adopted from [59].

Ion	Moment (μ_B)	Shell	Oh Orbital	$CFSE_{Oh}$	Td Orbital	$CFSE_{Td}$
Fe^{3+}	5	$3d^5$	$t_{2g}^3 e_g^2$	0	$e^2 t_{2g}^3$	0
Fe^{2+}	4	$3d^6$	$t_{2g}^4 e_g^2$	-4	$e^3 t_{2g}^3$	-2.7
Zn^{2+}	0	$3d^{10}$	$t_{2g}^6 e_g^4$	0	$e^4 t_{2g}^6$	0

native determination methods have been proposed. For example, the empirical valence force field approach, by Kutoli *et al.* [63], which minimizes empirically parametrized inter-atomic potential function energies. Alternatively, classification of the spinel structure has been conducted using the point-ion electrostatic model by Stevanovic *et al.* [64]. The model is parametrized by the oxygen displacement parameter u and by the relative cation valencies, Z_A and Z_B . They have proposed a simple rule for either the normal or inverse cation distribution preference. If $Z_A < Z_B$, the structure is normal for $u < 0.255$ and inverse for $u > 0.258$ [64]. This rule has shown a high success rate for the known spinel structures. On the other hand, by pseudopotential orbital radii approach, Zhang *et al.* [65] have shown that the anion type plays a minor role in determining cation distribution in spinels and that the d-orbital radii are of no explicit importance in this determination. However, O’Neil *et al.* [66] has demonstrated that the effect of disordering enthalpy depends linearly on the degree of disorder and cation size contributes to the thermodynamic properties. Similarly, based on the point-ion electrostatic model, Stevanović *et al.* [67] have described the disorder phenomena in the ground state of the normal and inverse spinel structures as well as a function of temperature. While the mentioned calculation methods describe and predict a number of structural possibilities, the controversy of cation distribution remains in need of experimental justification.

2.3 Band structure description

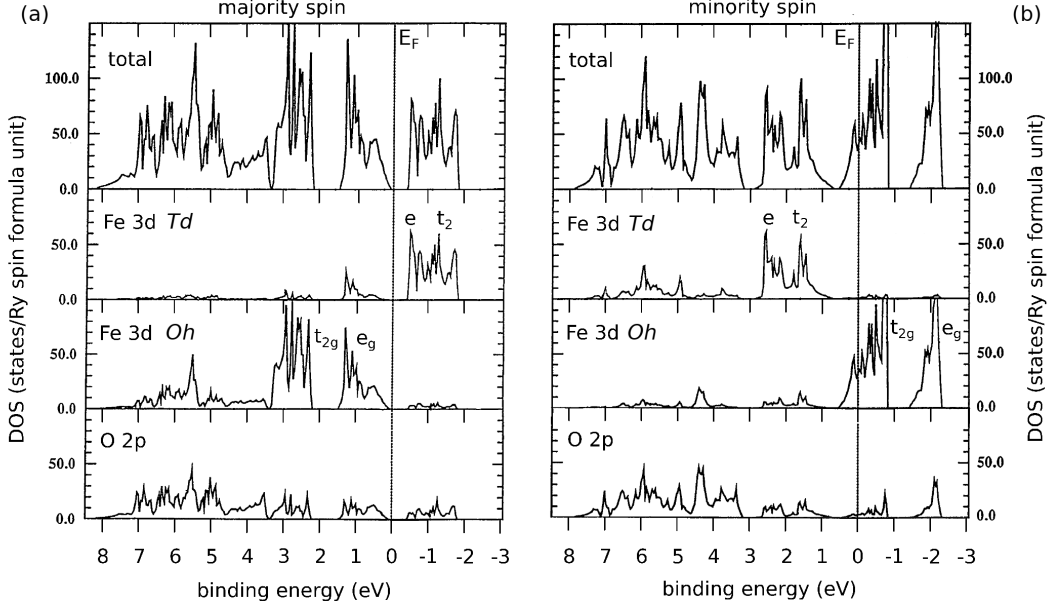


Figure 2.3: Density of states for (a) majority and (b) minority orbital resolved spin electrons in ferrimagnetic fcc Fe_3O_4 , calculated by local spin density approximation. Figure adopted from [68].

Theoretical description of the electronic structure from first principles is commonly conducted by an approximation of the density functional theory (DFT). The most frequent methods for calculation of the density of states (DOS) are the generalized gradient approximation (GGA), local density approximation (LDA), and self-interaction correlated local spin density approximation (SIC-LSDA). The appropriate choice of initial parameters results in an approximation which sheds light on the structural, magnetic, electronic and optical properties in dependence on the degree of inversion and cation distribution.

An example of the DOS for each majority and minority spin state and individual orbital for an fcc Fe_3O_4 is depicted in Figure 2.3 [68]. *Ab-initio* calculations on Fe_3O_4 were performed as early as 1984 [69] and give variable description of its conducting quality. The half-metallicity character is attributed to the minority t_{2g} electrons crossing the Fermi energy (E_F), while majority spin up band shows a band gap. This gives rise to the predicted 80% spin polarizability of the conduction electrons and makes Fe_3O_4 attractive for spintronic applications [70]. Most recent investigations were conducted using an additional U parameter in order to account for the strong electron correlation. In this case, however, a disproportionate ordering of orbital charge is exhibited and affects the electronic

2.3. Band structure description

properties in Fe_3O_4 . The influence of this parameter on the description of low temperature electronic structure of Fe_3O_4 is described by Jeng *et al.* [71]. A fair agreement between hybrid functional DFT and nuclear magnetic resonance has been recently demonstrated and confirmed minority spin electron presence at the E_F [72]. Most recent DFT-based calculations on Fe_3O_4 were conducted to predict structures which are likely to be encountered upon production of the thin film. In particular, the electronic description of the structures at the interface have been shown to deviate from the bulk and will be discussed in a later section in more detail.

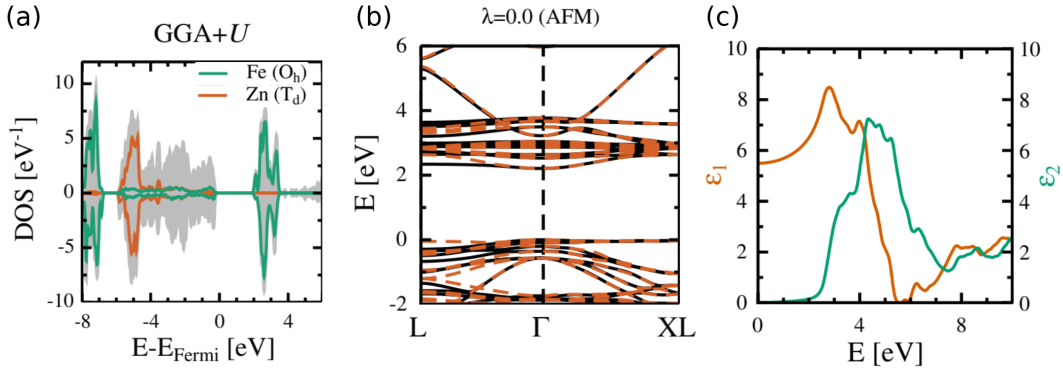


Figure 2.4: (a) Total and projected DOS per formula unit for ZnFe_2O_4 spinel in a normal ($\lambda = 0$) state, calculated with GGA+ U exchange-correlation functionals. (b) Electronic band structures, with majority (black lines) and minority spin (orange dashed lines) bands. The zero energy is set to the valence band maximum. (c) Real (orange) and imaginary (green) part of the dielectric function, calculated by GGA+ U method, adopted from [73].

For the ZnFe_2O_4 spinel ferrite, the description of the electronic structure strongly depends primarily on the inversion parameter, λ , Equation 2.1. Ideally, in the normal spinel configuration, the structure is expected to behave as an antiferromagnetic insulator. However, LSDA calculations by Singh *et al.* have shown a metallic band structure, while an insulating paramagnetic state was found by the GGA approach without the consideration of the Hubbard correlation [74]. Therefore, the appropriate choice of the Hubbard correlation parameter U is deterministic of the validity and accuracy of the DFT calculations. Furthermore, Soliman *et al.* demonstrated that the cation distribution is not enough for symmetry determination and an adjustment of the oxygen displacement parameter is necessary for an adequate description of electronic structure [75]. A decrease in the octahedral symmetry of Fe from O_h to C_{4v} showed a decrease in the stress of the octahedral site by forcing an increase in the degree of inver-

2.3. Band structure description

sion. Recently, a hybrid functional approach, based on Perdew-Burke-Ernezerhof (PBE) parametrization, was found to provide an appropriate description of the optical response [73, 76]. Ziaei *et al.* [76] provided an insight into the nature of the visible electronic transitions. Fritsch *et al.* [73] demonstrated energetically favorable ground state of a ferromagnetically coupled normal ZnFe_2O_4 spinel and the obtained results closely match the experimentally determined dielectric function (DF) for a similar structure [30]. Calculations of the DOS, electronic band structure and DF [73], using the GGA+ U exchange-correlation functionals for ZnFe_2O_4 spinel in a normal and antiferromagnetic state ($\lambda = 0$ from Equation 2.1), are shown in Figure 2.4(a), (b) and (c), respectively.

2.4 Verwey transition

By considering the simple ionic model, electrical conductivity in magnetite at room temperature is assumed to be due to itinerant electron hopping between Fe^{2+} and Fe^{3+} cations on the octahedral sublattice, Figure 2.2(b). However, as a function of temperature, a first order transition occurs at ~ 120 K and conductivity drops by two orders of magnitude.

While first detected by Parks *et al.* [77] in 1925, Verwey described this transition as an order-disorder transition [6]. Below the Verwey transition temperature (T_V), the periodic order prevents the motion of carriers by localizing the itinerant electron, thereby the structural phase would change from a metallic cubic to an insulating orthorhombic phase. While some studies provide experimental confirmation of this theory [78], numerous studies do not demonstrate Verwey type ionic ordering and contradict the simple description [79]. Most conduction models have been based on either band conduction and/or small-polaron hopping mechanism [80, 81]. However, the experimentally determined conduction maximum at 305 K does not match the predicted 600 K by the approach based on the non-interacting polaron model. By considering small-polaron band and small-polaron hopping mechanisms, Lorenz *et al.* [82] attributed the increase in conductivity above T_V to the destruction of short-range order due to thermally activated process. Despite substantial research since its discovery, the interpretations of the Verwey transition in magnetite remain controversial. The description of the recent developments were concisely summarized by Walz *et al.* [83] as well as Garcia *et al.* [84].

Furthermore, upon the distortion of crystal symmetry at T_V , the magnetic easy axis rotates from $\langle 111 \rangle$ in the cubic phase to the $\langle 001 \rangle$ monoclinic axis and an abrupt change in the magnetic moment is expected [85]. As T_V strongly depends on a variety of factors, such as the stoichiometry and strain, the presence of this transition is characteristic of inverse spinel magnetite and temperature dependence of magnetization provides a deeper insight into the magnetic interactions due to the crystallographic order.

2.5 Magnetic exchange interactions

Magnetic ground state of iron oxides in spinel configuration is governed mainly by indirect magnetic exchange interactions between Fe cations. Since oxygen anions have a full 2p shell, they act as mediating agents to their neighboring magnetic cations. The Fe^{2+} ($3d^6$, $S = 2$) cations occupy the octahedral lattice sites and have a net magnetic moment of $4\mu_B$. The Fe^{3+} ($3d^5$, $S = 5/2$), on the other hand, have a net magnetic moment of $5\mu_B$ and can occupy both sites. The Zn^{2+} ($3d^{10}$, $S = 0$) cation have no magnetic moment, a completely filled d-orbital and can also occupy both sites. Ferromagnetic (FM) double-exchange (DE) and antiferromagnetic (AF) super-exchange (SE) interactions between Fe cations of the Td (spin down) and Oh (spin up) site occupation give rise to the overall magnetic order.

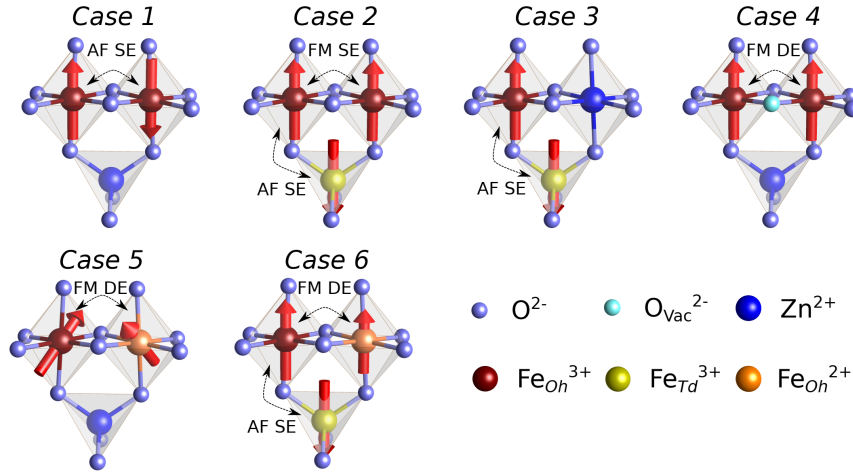


Figure 2.5: Schematic representation of possible magnetic configurations and interactions between the neighboring cations. The cations are color coded and the alignment of the magnetic moment is depicted by the red arrows for each case, see text for details.

Ideally, normal spinel ZnFe_2O_4 has an antiferromagnetic order below the Néel temperature of 10 K. However, neutron scattering experiments have shown that long-range magnetic order is not attained in a single crystal normal spinel ZnFe_2O_4 even at temperatures as low as 1.5 K due to three-dimensional geometrical spin frustration [36, 38]. The presence of structural disorder would suppress the intrinsic spin frustration, leading to the finite-range magnetic order [31]. Consequently, the possible cases are schematically depicted in Figure 2.5 and listed below [35, 47], ordered with respect to the decrease of Zn^{2+} content, increase in disorder, in the normal spinel ZnFe_2O_4 :

2.5. Magnetic exchange interactions

- *Case 1*: AF ordered normal ZnFe_2O_4 . The AF oxygen mediated SE interaction between two octahedrally coordinated Fe^{3+} cations.
- *Case 2*: Disordered ZnFe_2O_4 with Fe^{3+} on nominally unoccupied tetrahedral lattice site. This gives rise to the weak FM oxygen mediated SE interaction between the two Oh Fe^{3+} and a strong oxygen mediated AF SE interaction between Fe^{3+} , located on Td and Oh lattice sites.
- *Case 3*: Disordered ZnFe_2O_4 , where Fe^{3+} and Zn^{2+} now occupy Td and Oh lattice sites, due to the inversion mechanism. The strong oxygen mediated SE interaction between Fe^{3+} , located on Td and Oh lattice sites gives rise to the overall ferrimagnetic behavior.
- *Case 4*: Disordered ZnFe_2O_4 with the presence of an oxygen vacancy (O_{Vac}^{2-}). The AF SE interaction becomes FM interaction between Fe_{Oh}^{3+} cations.
- *Case 5*: Zn poor ZnFe_2O_4 , due to the presence of Td coordinated, non-magnetic, Zn cations. The magnetic interactions Td -O- Oh become uncompensated and result in a FM DE interaction. The spins are canted with respect to each other by an angle known as the Yafet-Kittel angle [86,87].
- *Case 6*: The case of Fe_3O_4 , where the FM DE and AF SE interaction between Oh -O- Oh and Td -O- Oh Fe cations is exhibited. In this case, the antiparallel alignment of the Fe_{Oh} and Fe_{Td} leaves only the Fe^{2+} cation with $4\mu_B$ to contribute to the net magnetic moment of the system.

The initial model for ferrimagnetism in Fe_3O_4 was proposed by Néel, where the antiparallel alignment of Td - Oh moments of Fe^{3+} cations would compensate each other and the net magnetic moment of $4\mu_B/\text{f.u.}$ would originate from the remaining Fe^{2+} cations [7]. However, this model does not take the FM DE interaction between Fe^{2+} and Fe^{3+} cations into account. Therefore, Yafet *et al.* [86] proposed a more detailed model where the Oh sublattice would be divided into Fe_{Oh}^{2+} and Fe_{Oh}^{3+} sublattices, Figure 2.5 *Case 6*. Due to the strengthening of the FM DE Oh -O- Oh interaction, the spins would no longer be strictly parallel to one another, but rather canted by a finite Yafet-Kittel angle. This mechanism is particularly important when the AF SE Td -O- Oh becomes weakened due to the increase of the Zn cation content, occupying the Td site, Figure 2.5 *Case 5*. As a result, magnetization saturation would originate from the competing AF SE between the two sites and the FM DE between Fe_{Oh}^{2+} and Fe_{Oh}^{3+} cations.

Theoretical approximation of the exchange integrals in magnetite has been described by Uhl *et al.* [88]. By considering non-collinear moment arrangements

2.5. Magnetic exchange interactions

of spin-spiral configurations and employing scalar relativistic augmented spherical wave method, the magnetic exchange constants $J_{Td-Td}(R_\alpha)$, $J_{Td-Oh}(R_\beta)$, and $J_{Oh-Oh}(R_\gamma)$ were approximated by [88]:

$$S_{Td}^2 n_{Td-Td}(R_\alpha) J_{Td-Td}(R_\alpha) = \frac{-1}{N \sin^2 \theta} \int d^3 q \cos(q \times R_\alpha) (E(q, \theta, 0) - E(0, \theta, 0)) \quad (2.3)$$

$$S_{Oh}^2 n_{Oh-Oh}(R_\beta) J_{Oh-Oh}(R_\beta) = \frac{-1}{N \sin^2 \theta} \int d^3 q \cos(q \times R_\beta) (E(q, 0, \theta) - E(0, 0, \theta)) \quad (2.4)$$

$$S_{Td} S_{Oh} n_{Td-Oh}(R_\gamma) J_{Td-Oh}(R_\gamma) = \frac{-1}{N \sin^2 \theta} \int d^3 q \cos(q \times R_\gamma) (E(q, \theta, \theta) - E(0, \theta, \theta)) \quad (2.5)$$

$$- S_{Td}^2 n_{Td-Td}(R_\alpha) J_{Td-Td}(R_\alpha) - S_{Oh}^2 n_{Oh-Oh}(R_\beta) J_{Oh-Oh}(R_\beta)$$

where the Td or Oh spin length is S , magnetic exchange energy per unit cell E in the spinel-spiral configuration is defined by the spin polar angle θ and vector q . The $J_{Td-Td}(R_\alpha)$, $J_{Td-Oh}(R_\beta)$, and $J_{Oh-Oh}(R_\gamma)$ are the exchange constants between the iron atoms and n_{Td-Td} , n_{Td-Oh} , and n_{Oh-Oh} are the appropriate weights per unit cell. As a result, the inter-sublattice AF SE was determined to be the strongest nearest-neighbor magnetic coupling with $J_{Td-Oh} = -2.88$ meV. The FM DE coupling, due to mixed valence state on the Oh , was the second strongest with $J_{Oh-Oh} = 0.83$ meV. Lastly, the AF SE coupling between two Td Fe^{3+} cations on adjacent sublattices was the weakest, with $J_{Td-Td} = -0.18$ meV. Although the values, calculated in this approximation, were slightly larger than those determined experimentally, a distinctive strength of the Td -O- Oh magnetic exchange interaction is evident. Furthermore, the importance of oxygen vacancies has been only recently considered and predicted to strongly influence the net magnetic moment of ZnFe_2O_4 [35]. The lack of an anion between the two AF ordered Oh Fe cations would result in a FM exchange interaction instead, Figure 2.5(Case 4). Theoretical calculations by Rodriguez Torres *et al.* [35] showed a contribution of $8\mu_B$ per oxygen vacancy per supercell due to the flipping of the spins, while a contribution of 6 and $10\mu_B$ per additional Td Fe cation per supercell was predicted for *Case 2* and *Case 3* (Figure 2.5), respectively. Not only would the length of the bonds be locally affected by the oxygen vacancy, but the lack of oxygen could be responsible for creating Fe^{2+} cations. This effect was considered to explain room temperature ferrimagnetic order in ZnFe_2O_4 in

2.5. Magnetic exchange interactions

dependence on oxygen pressure during fabrication [29]. However, as the detection of the Fe^{2+} cation remains technically challenging [40], its direct contribution to the net magnetic moment of ZnFe_2O_4 is yet to be carefully examined.

The presence of Fe^{2+} due to oxygen vacancy formation can be demonstrated indirectly. The FM DE interaction is mediated by the itinerant spin down t_{2g} electron hopping between Fe^{2+} and Fe^{3+} cations on the Oh sites. Owing to Hund's coupling rule, the spin of the itinerant electron is AF coupled to the local 3d spin up electrons [89]. As a result, the density of itinerant charge carriers is directly related to the electrical conductivity in spinel ferrite [32, 90]. This has been shown by Brachwitz *et al.* [91] in ZnFe_2O_4 film, grown in a wide range of oxygen partial pressures. While n-type conductivity was related to the presence of oxygen vacancies [92], p-type conductivity is widely considered to be caused by cation vacancies which act as acceptors [93]. Therefore, the choice of dopant agent in the AB_2O_4 system allows tailoring of electronic properties [94]. In fact, electrical conductivity was shown to be significantly lower in $\text{Zn}_x\text{Fe}_{3-x}\text{O}_4$ films grown in finite Ar/O_2 (99:1) mixed atmosphere, as compared to those grown in Ar [47]. This is explained by the presence of octahedral Fe^{3+} cation vacancies, which would weaken the density of thermally activated itinerant electron hopping between the mixed-valent octahedral $\text{Fe}^{2+}/\text{Fe}^{3+}$ cations. Furthermore, as also shown in this work, the deficiency of the octahedral Fe^{3+} cations would decrease the strength of the $Td\text{-O-}Oh$ AF SE interaction, which would weaken the overall magnetic response in magnetite [47]. The effects of cation vacancies on the geometric and electronic structures of normal ZnFe_2O_4 , from first principles, have been investigated by Yao *et al.* [95] and show a change from semiconducting to metallic band structure, depending on the vacancy defect.

Further deviations from the expected strength of magnetic response in magnetite as well as the rise of ferrimagnetic order in ZnFe_2O_4 have been explained by the formation of macroscopic structural defects, discussed in the next section.

Chapter 3

Sample preparation and modification

In light of rapidly growing technology frontier, accurately tailoring the desired properties of transition metal oxides is essential for device integration [9, 27]. This is achieved through precise fabrication solutions, which have advanced significantly in the past two decades. In this chapter, the deposition method and specifics are presented and discussed. The mechanisms, involved in film formation, give an insight into the resulting structures and their effect on the physical properties are outlined. Furthermore, the modification procedure as well as an overview of the investigated samples is provided.

3.1 Macroscopic spinel film formation

The mechanisms behind the formation of thin films as well as the resulting physical properties are presented and discussed below. Along with the importance of the substrate temperature and deposition chamber atmosphere, the appropriate choice of the substrate is essential for the engineering of film strain, which results in films with potentially controllable electrical and magnetic properties [97, 98]. Thin film crystallinity as well as the lattice plane orientation strongly depends on the lattice mismatch between the film and the substrate, defined by:

$$f = \frac{2(a_f - a_s)}{a_f + a_s} \sim \frac{a_f - a_s}{a_s} \quad (3.1)$$

where a_f and a_s denote the in-plane lattice constants (or multiples) of the film and substrate, respectively. Ideally, the substrates are chosen so that $|f| < 10\%$, thereby a single crystalline film exhibits epitaxial growth [96]. In the case of $f < 0$,

3.1. Macroscopic spinel film formation

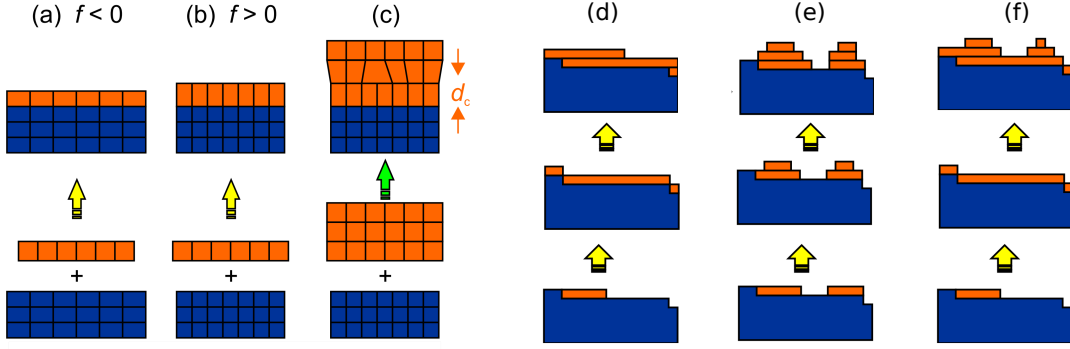


Figure 3.1: Heteroepitaxial thin film growth in dependence on strain, due to lattice mismatch f . (a) In-plane tensile and out-of-plane compressive strain, (b) in-plane compressive and out-of-plane tensile strain, (c) relaxed thin film formation for film thickness $> d_c$. (d) Frank-van Merwe (layer growth in two-dimensions), (e) Volmer-Weber (island growth in three-dimensions) and (f) Stranski-Krastanov (island on layer growth) modes. The film formation schematic was adopted from [96].

the film exhibits a tensile (compressive) strain in the in-plane (out-of-plane) direction, Figure 3.1 (a). For $f > 0$, compressive (tensile) strain is present in the in-plane (out-of-plane) direction, Figure 3.1 (b). Furthermore, once the film thickness exceeds a critical thickness of d_c (Figure 3.1 (c)), the film lattice relaxation to its bulk properties is accompanied by the formation of lattice defects. In some cases, the three growth modes of bulk epitaxial thin film can be distinguished by the film surface morphology.

To ensure a smooth film/substrate interface, the substrates are chemically cleaned and annealed prior to film fabrication, resulting in an atomically flat substrate surface, ideally with monolayer terraces, the blue base in Figure 3.1 (d-f). The film surface morphology shows either two- or three-dimensional structures. This can be explained through the thermodynamics of film growth modes, depicted in Figure 3.1 (d-f). Three main growth modes can be distinguished: Figure 3.1 (d) Frank-van Merwe (layer growth in two dimensions), (e) Volmer-Weber (island growth in three dimensions) and (f) Stranski-Krastanov (island on layer growth) [96]. Depending on the inter-atomic bonding strength as well as bonding strength between the film and the substrate, the realization of the three growth modes is possible. As long as the bonding strength between the film and the substrate remains dominant during the deposition, the Frank-van Merwe mode is achieved and the film forms in two dimensions. On the other hand, if the inter-atomic bonding strength remains dominant, the film grows in island-like

3.1. Macroscopic spinel film formation

structures, in accordance with the Volmer-Weber mode. With each deposited layer, the bonding strength between the film and the substrate weakens while the inter-atomic bonding strength increases, resulting in the Stranski-Krastanov growth mode [99–101]. The formation of the thin film in appropriate mode depends on the deposition specific parameters, such as the substrate temperature, chamber pressure, deposition rate, shape of the plasma plume and the deposited elements. However, island as well as nanostructure formation is frequently exhibited by magnetite as well as Zn ferrite thin films, respectively.

Anomalous magnetic and transport properties of magnetite thin films have been mainly attributed to the existence of anti-phase boundaries (APBs). Due to the presence of different nucleation areas during fabrication, the coalescence of island-like structures is indicative of the formation of structural domains, referred to as the anti-phase domains (APDs). Well reported is the growth of magnetite on MgO substrates [46, 102]. The atomically sharp APBs are due to the reduced cubic symmetry of Fe_3O_4 as compared to MgO, along with a lattice mismatch of $\sim 0.3\%$. In this case, the O lattice remains undisturbed and the APBs form as a stacking defect in the cation sublattice. The cation sublattice shifts by a vector, which is smaller than the lattice constant so that the cation sublattice becomes out of phase at the boundary. The shift of the APBs was shown to belong to either the $1/2 \langle 100 \rangle$ or the $1/4 \langle 110 \rangle$ set of directions [102]. In the case of $\text{Fe}_3\text{O}_4/(001)\text{MgO}$, Celotto *et al.* showed that 45% of the phase shifts are in the boundary plane being perpendicular to the shift, while the remaining 55% were out of the boundary plane, being oriented close to the $\{100\}$ or $\{310\}$ planes [102]. The size of the APDs depends strongly on the growth temperature and film thickness, as thicker films grown at high temperature favor larger domain size [103]. The size of the domains has been related to the square root of the film thickness, determined by transmission electron microscopy [104].

The formation of APBs is considered to be a characteristic of magnetite, which results from the growth process [106]. As a result, the altered Fe-O-Fe bond geometries cause a break in the continuity of the lattice formation, which modifies the local electronic structure. The intra-sublattice exchange interactions (J_{AA} and J_{BB}) dominate over the AF SE J_{AB} interaction and cause an antiferromagnetic coupling between the neighboring domains across the boundary. Depending on the shift vector as well as the boundary plane, only $\sim 50\%$ of the APBs attain an overall antiferromagnetic coupling [102]. As depicted in Figure 3.2 (a), the spin-polarized DOS show a transition from a positive to negative spin polarization across the three atomic layers near the APB defect. Also visible in Figure

3.1. Macroscopic spinel film formation

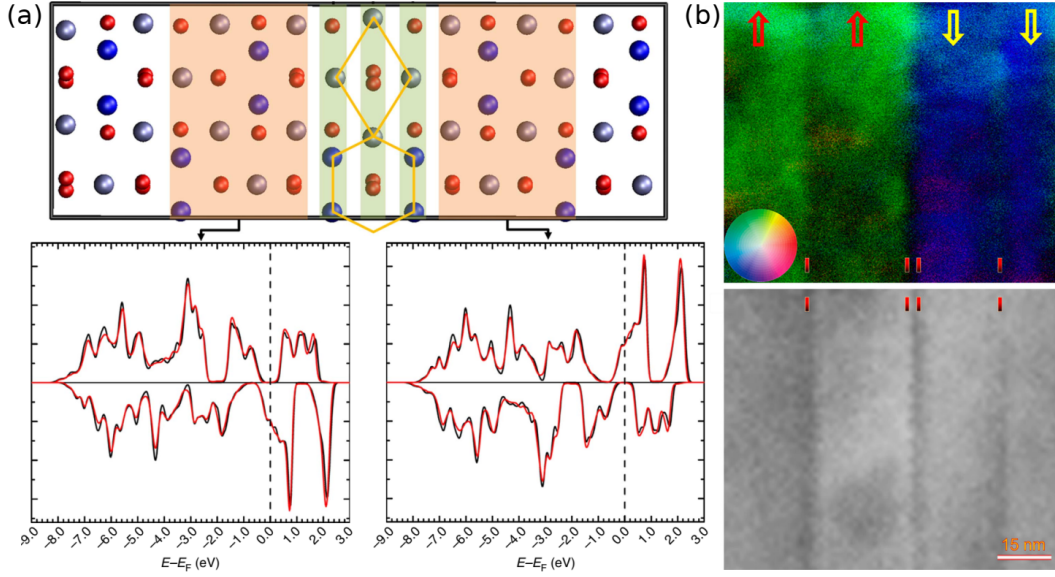


Figure 3.2: (a) Top: Fe₃O₄ schematic of the {110} APB defect (green shaded area). Bottom: spin-polarized DOS (red lines) of the bulk-like regions are almost indistinguishable from the DOS of the bulk crystal (black line). Image adopted from [45]. (b) Top: color-coded magnetic coupling across the phase boundaries, showing ferromagnetic (type I) and antiferromagnetic (type II) coupling. The reconstructed in-plane magnetization vector maps of the Fe₃O₄ twin lamellae, obtained by DPC STEM, the color wheel indicates magnetic field direction/strength. Bottom: bright-field TEM images of the same Fe₃O₄ twin lamellae. Adopted from [105].

3.2 (a) is a fair agreement between the DOS of the bulk-like region (red lines) and that of a single crystal (black lines) [45]. McKenna *et al.* have demonstrated that APB defects on the {110} planes induce the antiferromagnetic coupling between adjacent domains and explain the high stability of the {110} APB defects by the presence of metastable bulk *Pmma* phase of Fe₃O₄ at the APB (Figure 3.2(a) green regions), due to strain in films or nanostructures [45]. Numerous studies have been conducted on understanding the type of coupling present by using state-of-the-art atomic-resolution scanning transmission electron microscopy (STEM) and differential phase contrast (DPC) imaging [44, 45, 107, 108]. An exemplary image is depicted in Figure 3.2 (b) [105]. Most recently, Chen *et al.* [105] demonstrated existence of ferromagnetic coupling between the APBs along with the antiferromagnetic coupling, type I and II in Figure 3.2 (b), respectively. Thereby underlining the importance of the atomic core structures present at the interfacial/intergranular regions. Furthermore, the implications of these defects on the structural relaxation and the bulk properties of magnetite thin films still remain

3.1. Macroscopic spinel film formation

controversial.

As the domain size depends on the thickness of the magnetite film layer, the structures that form in the near-surface region also have a considerable impact on the thin film properties. Of particular interest is the transition of the surface electronic structure and charge order around the Verwey transition temperature [109,110]. Bernal-Villamil *et al.* have shown a $(\sqrt{2} \times \sqrt{2})R45^\circ$ reconstruction of the Fe_3O_4 (001) surface of the bulk phase below the Verwey transition temperature [111]. A rise of an insulating surface gap was due to the large demand of the surface O [111]. Figuera *et al.*, on the other hand, have shown that the reconstruction of the (100) surface is unperturbed by the bulk transition, and is continuous over the phase boundaries, revealing that the bulk first order transition is not an extension of the Verwey-like surface reconstruction [109]. Lodziana *et al.* described such reconstruction as the "surface Verwey transition" and have suggested that the surface remains insulating, regardless of temperature [112]. Furthermore, speculation about the existence of a magnetically dead layer at the magnetite surface has recently been disproven experimentally and attributed to the surface structures, which attain the magnetic moment. In order to understand the surface structures better, a subsurface cation vacancy (SCV) model has been proposed to also explain the adsorption phenomena of the magnetite surface [113]. In the SCV model, the surface Fe_{Oh} -O layer remains stoichiometric, but is distorted by the rearrangement of the cations in the subsurface layers [8], namely additional Fe_{Td} in the second layer replaces two Fe_{Oh} cations from the third [114]. Furthermore, while the surface is believed to exhibit Fe_{Oh} termination, the presence of metastable Fe_{Td} termination has been proposed [115]. In order to explain the deviation of the magnetic moment in the surface layer, the distribution of magnetic domains and even the presence of a phase between Fe_2O_3 and Fe_3O_4 has been demonstrated experimentally [101, 116].

As a consequence of the surface layer, its effect on the total magnetic behavior becomes considerably significant with the decrease in film thickness. In magnetite, it is believed that the exchange interactions at the APBs form a magnetically hard structure that overshadows the effect of both the crystalline and shape anisotropy under variations of the magnetic field directions [117]. However, with decreasing thickness to an ultrathin thickness (<5 nm) magnetite films were reported to exhibit superparamagnetic and insulating behavior [106]. In the case of ZnFe_2O_4 , however, the room temperature ferrimagnetism is due to the degree of inversion or disorder, namely Fe^{3+} on tetrahedral sites, arising from the defects as presented in Section 2.1. Although Torres *et al.* [29] demonstrated homoge-

3.1. Macroscopic spinel film formation

neous distribution of Fe and Zn cations within the ZnFe_2O_4 thin films, Stewart *et al.* [40] have shown a significant contribution from the surface effects as the structure becomes nanocrystalline [37]. While surface cation magnetic contributions of Fe^{3+} at two sites were in the same magnetic phase, determined by field dependent X-ray magnetic circular dichroism measurements, the in-plane surface anisotropy was shown to differ from the volume anisotropy, contributing to the overall magnetic response [41]. The superparamagnetic behavior along with a ferromagnetic contribution at room temperature has also been attributed to nanostructure formation and modification [118]. In fact, it is the nanoparticle formation that gives rise to the superparamagnetic contribution, while the ferromagnetic contribution is due to cation inversion, consistent with field and temperature dependent magnetization behavior [31, 119]. On the other hand, the temperature dependent magnetization was determined to be caused by inter-particle interactions among nanoparticles with cluster spin glass-like behavior [119, 120]. The cluster spin glass-type system exhibits a magnetic transition at a temperature proportional to the degree of inversion. Below this temperature, the spins are frozen and magnetic moment is attained cooling under a magnetic field [39]. Due to the ambiguity of this transition, it is commonly interchanged with the superparamagnetic particle or cluster blocking temperature [31]. Whether the magnetic strength at low temperatures is caused by magnetic clusters or by particles, which are magnetically blocked, remains speculative. Due to their similarity, both concepts attempt to explain the bimodal magnetic state, evident from temperature and field dependent magnetization. The strength of the magnetic response was shown to depend inversely on the particle size [118, 121], which suggests at least two competing interactions are present. The bimodal magnetic behavior of the system, specifically the negative remnant magnetization, can be attributed to two magnetic contributions within the nanoparticle concept described below.

If we consider a nanoparticle system, where the surface and core spins contribute to the overall response, then a bimodal magnetization state is expected. This is due to the evolving dominance between anisotropy energy, Zeeman energy and antiferromagnetic coupling energy under different field and temperature conditions [123]. In this case, a wasp-waist behavior would be exhibited and could show negative remanent magnetization, as depicted in Section 5.5 for films with Zn content of 1.26. Since the surface and core spins exhibit different magnetic behavior, namely hard or soft hysteresis loop, the net magnetization along the applied field can be given by:

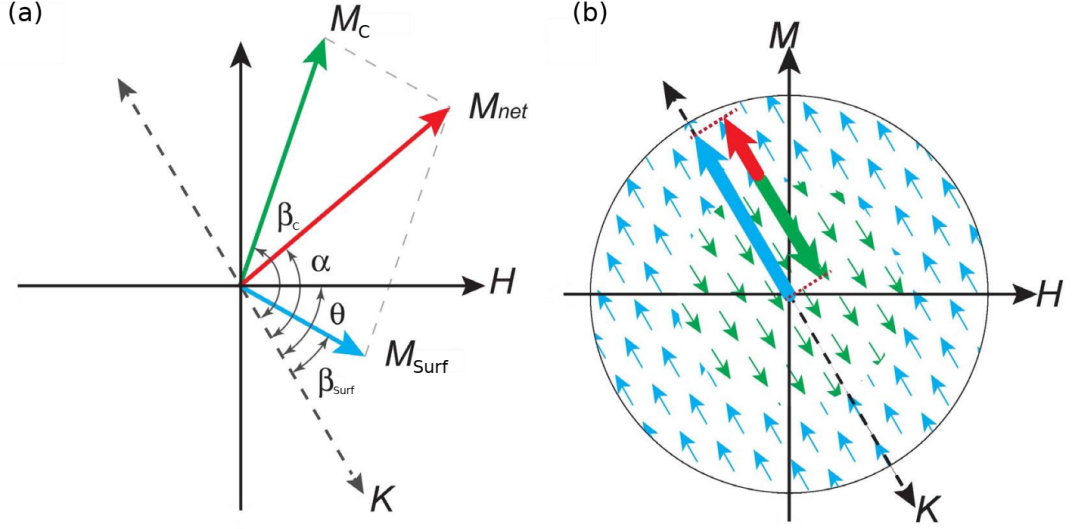


Figure 3.3: (a) Schematic illustration of the wasp-waist system. The M_C , M_{Surf} and M_{net} arrows correspond to core, surface and total magnetization, respectively. (b) Schematic depiction of antiparallel alignment of core and surface spins in order to induce a negative total magnetization, aligned along the easy axis K . Image adapted from [122].

$$M = M_{Surf} \cos(\beta_{Surf} - \theta) + M_C \cos(\beta_C - \theta) \quad (3.2)$$

where M_{Surf} and M_C correspond to surface and core magnetization, while β are their orientation directions with respect to the easy axis, as depicted in Figure 3.3 (a) [122]. The alignment of the core and surface spins depends on the applied magnetic field, prior to measurement, as well as temperature. After a low applied field, the surface spins can fluctuate along the easy axis and a positive remnant magnetization is achieved. At very low temperatures, the antiferromagnetic coupling between the core and surface spins is suppressed, because the rotation of the core spins is frozen upon removal of the applied field and mutual alignment of the core spins is sustained. If the external magnetic field is sufficiently strong to saturate the surface spins, then the core and surface spins are aligned antiparallel to each other and resulting negative total magnetization, M_{net} , is aligned along the direction of the easy axis K , but not the applied field direction [122]. This case is depicted schematically in Figure 3.3 (b) and has been proposed to explain the occurrence of negative remanent magnetization in a nanoparticle system [122]. However, the model would then depend on the nanoparticle size as well as the corresponding surface to volume ratio. Furthermore, the difference in the degree of disorder within the surface as well as the core would be deterministic of the

3.1. Macroscopic spinel film formation

strength of each contribution to the bimodal magnetic state. The manipulation of the aforementioned factors has placed ZnFe_2O_4 as an ideal candidate material in a wide scope of applications, while their determination and phenomenological contribution to the magnetic behavior remain technically challenging and controversial.

3.2 Pulsed laser deposition

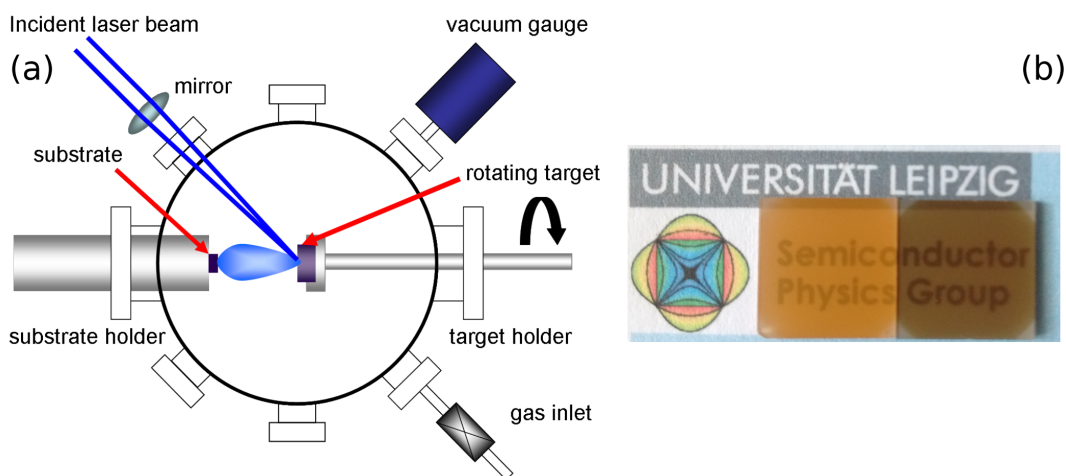


Figure 3.4: (a) Schematic depiction of the growth procedure inside the PLD chamber. The image was adapted from [124]. (b) ZnFe_2O_4 thin films ZFOT1 (left) and ZFOT2 (right), grown at low and high oxygen partial pressure, can be distinguished by their color.

Thin films in this investigation were grown by the pulsed laser deposition (PLD). A schematic representation of the growth procedure within the chamber is depicted in Figure 3.4(a). The resulting thin film samples are shown in Figure 3.4(b). The target was prepared within the Semiconductor Physics Group at the Felix Bloch Institute for Solid State Physics, Universität Leipzig through mixing of ZnO and Fe_2O_3 powders of high purity obtained from Alfa Aesar, Berlin Chemie. By mixing the powder proportionately and sintering the mixture at 1200°C , stoichiometric ZnFe_2O_4 target was achieved. A pulsed KrF excimer laser (Coherent Lambda Physik LPX305i), operating at a wavelength of 248 nm, was used to vaporize the surface of the target. To ensure homogeneous deposition of the thin film with uniform thickness, the target was put into constant rotation. The excimer laser, with a pulse duration of 25 ns, an energy of 600 mJ and constant energy density of 2 Jcm^{-2} was used. This resulted in elemental species of low and high mass clustered target constituents, namely the plasma plume which condensates onto the surface of the substrate forming the thin film. The adjustable temperature of the substrate is measured at the radiation heater element by the resistance heater, however the actual substrate temperature is expected to be lower. By adjusting the laser pulse repetition frequency and the number of pulses, preparation of films with predetermined thickness is possible. Further deposition parameters, such as target-substrate distance, background gas

3.2. Pulsed laser deposition

and pressure as well as laser energy density at the target can be properly adjusted to obtain thin films with various structural properties [52]. Furthermore, because it is possible to change the target without influencing the conditions inside the chamber, it is also possible to grow multilayered structures. The $\text{Zn}_x\text{Fe}_{3-x}\text{O}_4$ composite (ZnX0-ZnX4) thin films used for this investigation were deposited on $\text{TiN}/(100)\text{MgO}$ this way.

The substrate is usually chosen to have the least lattice mismatch with the deposited thin film in order to achieve epitaxial film growth, while retaining the best properties for applications. Most common substrates, also used in this work, are single crystal materials such as MgO and SrTiO_3 with dimensions of $10\times 10\times 1\text{ mm}^3$, obtained from CrysTec.

The $\text{Zn}_x\text{Fe}_{3-x}\text{O}_4$ composite films were deposited on TiN film on (100) MgO substrate in order to build a magnetic tunnel junction device as a candidate for spintronic application, c.f. Bonholzer [51]. The (100) -oriented MgO single side polished substrates, with a miscut angle of $\gamma \leq 0.15^\circ$, were annealed at 950°C for two hours using the CO_2 -laser in order to obtain a reproducible preparation of atomically flat, monolayer terraced substrate surfaces, providing optimal conditions for two-dimensional growth of the thin films. More detailed investigation on the influence of the annealing temperature and environment on the surface properties was conducted by Bonholzer *et al.* [51]. With the intention of sample applications in spintronic device, TiN was chosen due to its high conductivity and high crystalline structure, with the lattice parameter being close to that of MgO . The TiN deposition parameters were chosen to produce an atomically flat surface with monolayer terraces, optimal for the growth of $\text{Zn}_x\text{Fe}_{3-x}\text{O}_4$ thin films.

The composite thin films were deposited at a substrate temperature (T_S) of 400°C and Ar background pressure of 3×10^{-2} mbar. The excimer pulse energy was 500 mJ with a repetition rate of 15 Hz, with a laser aperture of $15\times 4\text{ mm}^2$. The pulse number chosen was 15000, resulting in a film thickness of 35 to 63 nm, depending on the Zn concentration x , which was varied by adjusting the lens position L during deposition. As reported by Lorenz [125], variable transfer factors of dopant concentration from target into the film during deposition were observed. The transfer factor of Fe in ZnO , was determined to be 1.47 ± 0.16 , meaning due to different evaporation temperature, 907°C for Zn and 2861°C for Fe, the evaporation rate of Zn determines the film composition. Therefore, by increasing the energy density at the target and changing the lens position, it is possible to adjust the Zn concentration in the deposited $\text{Zn}_x\text{Fe}_{3-x}\text{O}_4$ composite thin films.

3.3 Thermal treatment

In order to investigate the effect of high temperature treatment, ZnFe_2O_4 films were annealed in a chamber equipped with O_2 , Ar and N_2 gas purge capability. Initially, the chamber was pumped to vacuum for the duration of 30 min. Next, the chamber was flooded with either O_2 or Ar gas until the pressure of 100 mbar was reached. The samples were then annealed at temperatures 250, 300, 330 and 375° C for a period of 4 hours. The chamber was then cooled for the duration of 30 min and the pressure was increased to 800 mbar. Prior to retrieving the samples, the chamber temperature was stabilized between 30 and 60°C. Treatment duration of 4 hours was chosen, based on previous annealing investigation of ZnFe_2O_4 thin films. [34] The thin film magnetic response was found to reach saturation within this period.

3.4. Sample overview

3.4 Sample overview

Fabrication and treatment parameters of the samples investigated in this study are listed in Table 3.1. The specific thin films will hereinafter be referred to by their sample name. Apart from FFO and ZnX0-ZnX4 samples, the film composition from EDX showed a fair agreement with the Zn:Fe (1:2) ratio, as expected for the bulk ZnFe_2O_4 material. Note, the (*) corresponds to LP ZFO and HP ZFO films annealed in oxygen (O_2) and argon (Ar) atmosphere, respectively. The temperature and pressure during thermal treatment is as listed. The investigated ZnFe_2O_4 and $\text{Zn}_x\text{Fe}_{3-x}\text{O}_4$ thin films were deposited by H. Hochmuth and M. Bonholzer, respectively, using targets, prepared by G. Ramm. The Fe_3O_4 thin film (FFO) was prepared by M. Ziese at the Felix Bloch Institute for Solid State Physics, Universität Leipzig.

Table 3.1: Fabrication specific parameters for the investigated thin films. The sample name will be used throughout this work. Composition for the ZnX0-ZnX4 sample series and ZnFe_2O_4 was determined from EDX and is relative to the Zn:Fe ratio (1:2), as expected for bulk ZnFe_2O_4 material. The substrate, its temperature (T_S) as well as pressure during deposition is listed. The atmosphere was oxygen for all thin films, unless specified otherwise. The thickness was determined from B-Spline numerical approximation of the DF and correlated with XRR or SEM. Note: (*) samples O250-O375 and Ar250-Ar375 were annealed in oxygen and argon, respectively at temperature and pressure specified.

Sample name	Composition (EDX)	Substrate	Film thickness (nm)	Substrate T_S ($^\circ\text{C}$)	Pressure (mbar)
FFO	Fe_3O_4	MgAl_2O_4	107.1	550	9×10^{-6}
ZFOT1	ZnFe_2O_4	MgO	150.5	350	6×10^{-5}
ZFOT2	ZnFe_2O_4	MgO	224.3	640	0.016
ZFOT1.1	ZnFe_2O_4	SrTiO_3	53.1	350	6×10^{-5}
ZFOT2.1	ZnFe_2O_4	SrTiO_3	57.9	640	0.016
ZFOT4	ZnFe_2O_4	SrTiO_3	40.3	400	0.016
ZFOT5	ZnFe_2O_4	SrTiO_3	41.7	500	0.016
ZFOT6	ZnFe_2O_4	SrTiO_3	41.0	600	0.016
ZnX0	$\text{Zn}_0\text{Fe}_3\text{O}_4$	TiN/(100)MgO	59.0	400	3×10^{-2} (Ar)
ZnX1	$\text{Zn}_{0.26}\text{Fe}_{2.74}\text{O}_4$	TiN/(100)MgO	45.7	400	3×10^{-2} (Ar)
ZnX2	$\text{Zn}_{0.56}\text{Fe}_{2.44}\text{O}_4$	TiN/(100)MgO	41.9	400	3×10^{-2} (Ar)
ZnX3	$\text{Zn}_{0.87}\text{Fe}_{2.13}\text{O}_4$	TiN/(100)MgO	40.1	400	3×10^{-2} (Ar)
ZnX4	$\text{Zn}_{1.26}\text{Fe}_{1.74}\text{O}_4$	TiN/(100)MgO	34.1	400	3×10^{-2} (Ar)
LP ZFO	ZnFe_2O_4	SrTiO_3	73.3	300	1×10^{-5}
O250*	ZnFe_2O_4	SrTiO_3	73.3	250*	100 (O_2)*
O300*	ZnFe_2O_4	SrTiO_3	73.3	300*	100 (O_2)*
O330*	ZnFe_2O_4	SrTiO_3	73.3	330*	100 (O_2)*
O375*	ZnFe_2O_4	SrTiO_3	73.3	375*	100 (O_2)*
HP ZFO	ZnFe_2O_4	SrTiO_3	69.5	300	0.016
Ar250*	ZnFe_2O_4	SrTiO_3	69.5	250*	100 (Ar)*
Ar300*	ZnFe_2O_4	SrTiO_3	69.5	300*	100 (Ar)*
Ar330*	ZnFe_2O_4	SrTiO_3	69.5	330*	100 (Ar)*
Ar375*	ZnFe_2O_4	SrTiO_3	69.5	375*	100 (Ar)*

Chapter 4

Methods and general properties

4.1 Structure characterization techniques

Structural characterization was conducted by the following methods. Crystallinity of the investigated thin films was estimated by X-ray diffraction and Raman spectroscopy. Initial determination of the film thickness was conducted with the X-ray reflectivity technique. Energy dispersive X-ray spectroscopy gave an insight into the proportional weight of each element (Fe and Zn) found in the investigated material. Images for cross sectional analysis were obtained by scanning electron microscopy. The specifications as well as operational details of these methods are discussed in this chapter.

4.1.1 X-ray diffraction

The crystalline quality of the lattice structure was revealed by X-ray diffraction (XRD) $2\theta - \omega$ scans using a wide angle Phillips X'Pert Bragg-Brentano diffractometer with Cu ($\lambda_{XR} (K_\alpha) = 1.5406 \text{ \AA}$) radiation. The X-rays are scattered from the three-dimensional lattice of the crystalline films as well as the substrate. An interference pattern is formed with significant X-ray intensity at angle of their reflection from the lattice planes. A schematic depiction of the operational principle is shown in Figure 4.1(a). Beside the intensity coming from the thin film structures, the W L_α , $K_{\alpha 1}$, $K_{\alpha 2}$ as well as K_β reflexes are visible, originating from the Cu anode. The 2θ scan is conducted along the n vector, depicted in Figure 4.1(b), and provides information about the structural phases, present in the film. The path difference between X-rays, diffracted from two lattice planes is related to the wavelength by the Bragg equation:

4.1. Structure characterization techniques

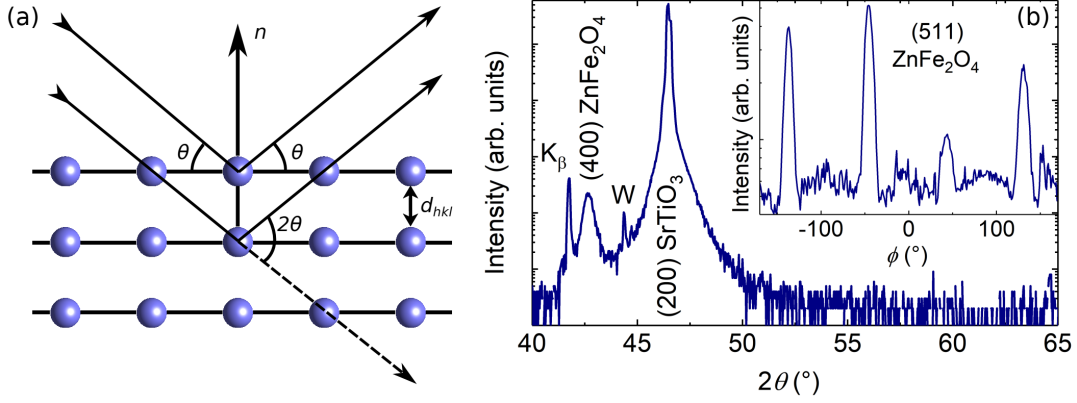


Figure 4.1: (a) Schematic depiction of the XRD operational principle satisfying the Bragg Equation 4.1. The vector, normal to the lattice plane, n , as well as lattice plane spacing, d_{hkl} , are shown. Created using VESTA [54]. (b) Wide angle 2θ scan shows the reflexes of Cu K_β from the substrate, (400) $ZnFe_2O_4$, W L_α peak as a result of the X-ray tube, and the (200) $SrTiO_3$ substrate. The inset shows a four-fold symmetry of the (511) $ZnFe_2O_4$ reflex.

$$2d_{hkl}\sin\theta = n\lambda_{XR} \quad (4.1)$$

where n is the diffraction order, h , k and l are the Miller indices, describing the lattice planes, and θ is the angle between the crystallographic plane and incident X-ray, as depicted in Figure 4.1(a). The lattice plane spacing, $d_{h,k,l}$, can then be related to the lattice constant, a , for a cubic lattice by:

$$a = d_{hkl} \times \sqrt{h^2 + k^2 + l^2} \quad (4.2)$$

Effects such as strain due to film and substrate lattice mismatch as well as a possible composition gradient within the sample lead to small variations in the lattice plane spacing, evident by a broadening of the film reflex. Therefore, the Scherrer equation:

$$d_{hkl} = \frac{\lambda_{XR}}{2\Delta\theta \times \cos\theta} \quad (4.3)$$

based on the method proposed by Nelson and Riley:

$$\frac{\Delta d}{d} \propto \left(\frac{\cos^2\theta}{\sin\theta} + \frac{\cos^2\theta}{\theta} \right) \quad (4.4)$$

is necessary to account for the intrinsic defects. The extrapolation of $\cos^2\theta$ as a function of the lattice plane spacing yields a more exact value of the out-of-plane

4.1. Structure characterization techniques

lattice constant [126].

The in-plane epitaxial relationship between the substrate and the thin film is determined by the ω scan, where the angle of the diffractometer is set to a symmetric reflex and the sample is rotated by an angle, ϕ , normal to n in Figure 4.1(a). For a cubic structure of (100) orientation, a fourfold symmetry, at $\phi = 0^\circ$, 90° , 180° and 270° , of the ω (511) reflex, depicted in the inset of Figure 4.1(b), is indicative of epitaxial growth.

To summarize, while the reflex position in the 2θ scan reveals the out-of-plane structure and lattice parameter information, the peak width is related to the crystalline size and intrinsic defects, such as strain. The ω scan provides further information about the film structure, such as its mosaicity and texture.

4.1.2 X-ray reflectivity

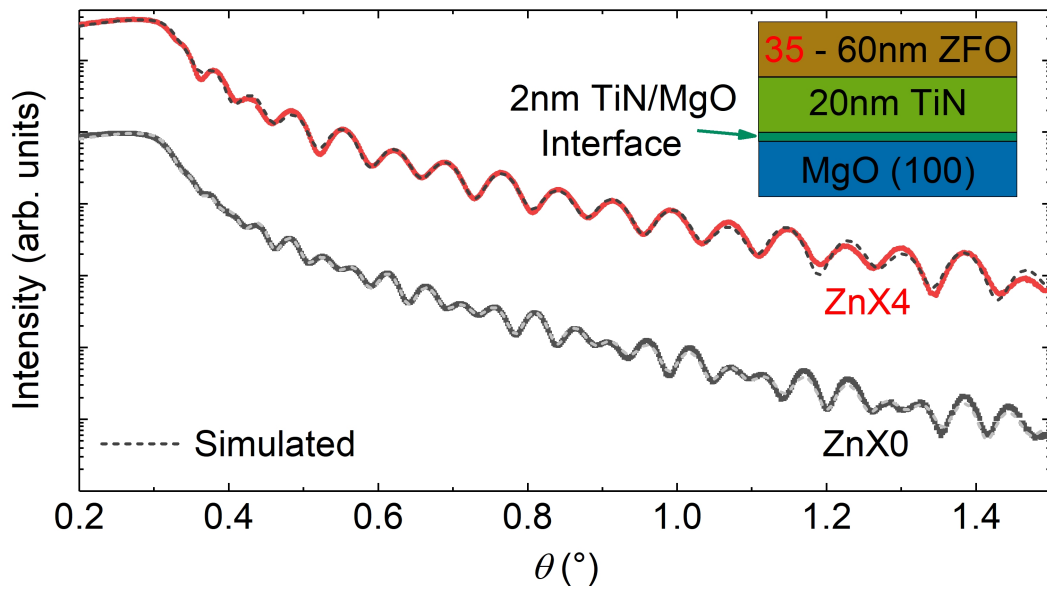


Figure 4.2: XRR simulated and experimental spectra for the ZnX4 (35 nm) and ZnX0 (60 nm) samples, shifted vertically for clarity. The layer model, used to simulate the experimental data, is shown as inset.

X-ray reflectivity (XRR) technique allows determination of the thickness and interface roughness of individual layers within the sample. The small incident angle $\theta \leq 5^\circ$ of the incident X-rays results in a specular reflection in dependence on the incident angle θ . The reflectivity of the X-rays at individual layers and thus the effectiveness of this method, strongly depends on the difference between their mass density. Exemplary simulated and experimental XRR spectra are depicted for the ZnX0 and ZnX4 samples in Figure 4.2 along with the layer model used

4.1. Structure characterization techniques

for simulation. While the film density ρ and layer thickness has an influence on the oscillation amplitude and spacing of the layer thickness interference patterns, the interface roughness influences the oscillation amplitude and total intensity. In the absorption-free spectral range, the refractive index, n , of a medium for X-rays can be given as:

$$n = 1 - \frac{e^2 \lambda_{XR}^2}{2\pi m_e c^2} N_A \rho_e \quad \text{where} \quad \rho_e = \frac{Z}{m_A} \rho_m \quad (4.5)$$

In this case, N_A is the Avogadro constant, e is the electron charge, m_e is the electron mass, c is the speed of light and λ_{XR} is the incident wavelength. The electron density ρ_e is related to the mass density ρ_m by a ratio of the atomic number Z and atomic mass m_A [126].

Total reflection occurs for the incident angle of the X-rays being smaller than the critical angle θ_C . The critical angle is proportional to $\sqrt{\rho}$, and the degree of total reflectivity can then be expressed as: [127]

$$R \simeq \left(\frac{\theta_C}{2\theta} \right)^4 \quad (4.6)$$

Since the refractive index difference between the layers of the sample is correlated to the difference in the layer density, the amplitude and intensity of the oscillations, caused by reflection from the interfaces, are proportional to the density difference. This allows a precise determination of the mass density of each layer, given that the density difference is of significant magnitude. The period of the interference pattern depends only on the film thickness, thus allowing precise determination of the layer thickness. The values are fitted to the XRR spectra using the X'Pert Reflectivity software of Malvern Panalytical Ltd., which takes into account the predefined measurement parameters and uses the Parratt-formalism to describe the multilayer system. Three methods to simulate the experimental spectra are possible, namely the genetic algorithm, segmented fit and a combination of both methods. The measurements were partially conducted and evaluated by M. Bonholzer at the Felix Bloch Institute for Solid State Physics, Universität Leipzig. From the XRR spectra, the layer thickness, density and roughness are determined, similar to the approach reported for $\text{Fe}_3\text{O}_4/\text{TiN}/\text{Si}(100)$ multilayers [128].

4.1.3 Energy dispersive X-ray spectroscopy

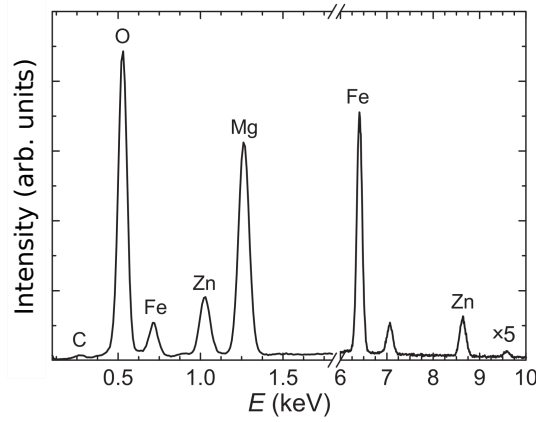


Figure 4.3: EDX spectrum of a ZnFe_2O_4 thin film of similar growth conditions as ZFOT2 on MgO substrate. The spectra (≥ 6 keV) was multiplied by a factor of 5 for clarity. This image was adapted from [49].

The elemental composition and stoichiometry of the investigated samples was determined using energy dispersive X-ray spectroscopy (EDX). A dual beam microscope FEI NanoLab Nova 200 is equipped with an Ametek EDAX energy dispersive spectroscopy (EDS) detector, a silicon drift detector. It is also capable of conducting scanning electron microscopy (SEM) analysis, discussed in following section.

The principle of EDX is to excite the inner shell electrons using X-ray radiation. The generated electron vacancies are then filled by outer shell electrons. The transition from high energy state to low energy state emits X-ray photons of a certain energy, which is characteristic of the transition as well as of the element, depicted in Figure 4.3 [49]. Energy of 15 keV was used for excitation of the atoms within the sample. The resulting spectra from the emitted X-ray photons was then analyzed to obtain atomistic ratios which define the stoichiometry of the sample. Four to five measurements were conducted on different areas of the thin film. The measurements were carried out and evaluated by J. Lenzner at the Felix Bloch Institute for Solid State Physics, Universität Leipzig. The standard deviation of the values from the average was found to be 4%, signifying the homogeneity in the elemental composition of the whole sample.

4.1. Structure characterization techniques

4.1.4 Focused ion beam and scanning electron microscopy

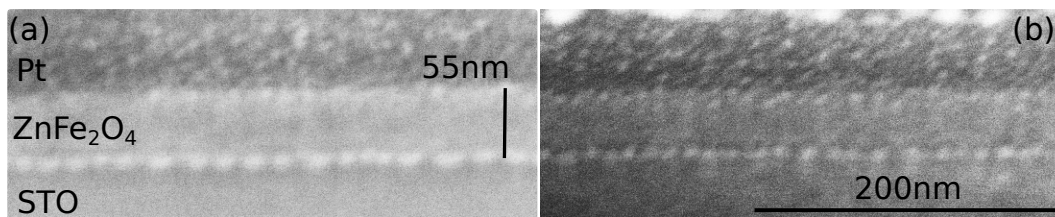


Figure 4.4: SEM images of ZnFe_2O_4 thin films, grown at high (a) and low (b) temperatures, namely ZFOT2.1 and ZFOT1.1 thin films, respectively. Sample thickness, STO substrate and Pt cap layer is indicated. The contrast between the layers is limited by the resolution of the device.

Focused ion beam (FIB) option of the dual beam microscope system allows thin film lateral SEM images to be recorded. A beam of gallium ions from the liquid-metal ion source is used for site specific milling to cut the sample for cross sectional analysis. Platinum capping layer is deposited from an organometallic precursor on the thin film surface in order to eliminate induced charges. The small spot size of the focused ion beam with high kinetic energy (~ 30 keV) allows milling of well defined structures into the sample surface. Focused electron beam with acceleration voltage between 5 and 15 kV then scans the thin film. This causes two types of interactions and thus two types of electrons are emitted, namely the secondary electrons with a low kinetic energy and back-scattered electrons with a high kinetic energy. The former interaction is the inelastic scattering of the incident beam and the K-shell electrons of the element specific atoms. Amount of emitted secondary electrons define the pixel contrast of the recorded image. The latter interaction, however, is elastic electron scattering which contributes to the background signal and reduces the SEM resolution. An exemplary lateral structure image for ZFOT2.1 and ZFOT1.1 films is depicted in Figure 4.4. Measurements were conducted by J. Lenzner at the Felix Bloch Institute for Solid State Physics, Universität Leipzig. The thickness of the samples, analyzed by SEM, showed a fair agreement to the values, obtained by XRR. The SEM micrographs reveal a presence of an interface layer between the substrate and investigated layers for all measured thin films.

4.1.5 Raman spectroscopy

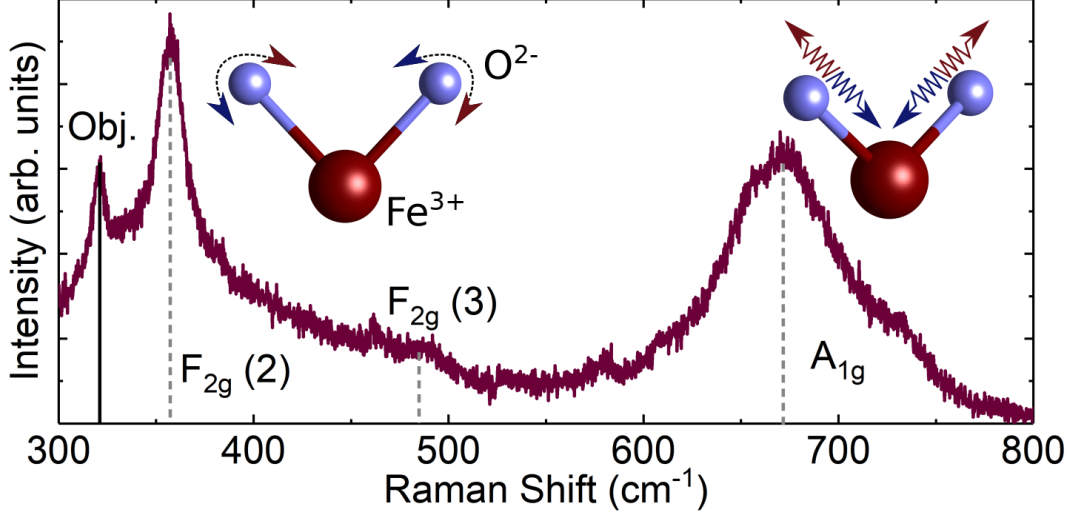


Figure 4.5: Raman spectra for the O375 sample with main F_{2g} and A_{1g} modes along with the peak resulting from the objective, used in the experimental set-up, are indicated. The inset shows a schematic depiction of asymmetric bending and symmetric stretching vibrational phonon modes of oxygen O^{2-} anions with respect to iron Fe^{3+} cations. Created using VESTA [54].

The crystalline formation was further examined by Raman spectroscopy. The elementary vibrational excitations, phonons, propagate as waves through the crystal [129]. Depending on the direction of propagation, relative to the direction of atomic displacement, the phonon modes are classified as transverse or longitudinal. In crystals of a diatomic base, the phonons can be distinguished as acoustical phonons, where the sublattices oscillate as a single chain, or optical phonons, for which the sublattices oscillate against each other. In the vicinity of the Γ -point in the Brillouin zone, for long wavelengths and small wave vectors, the energy of acoustical phonons vanishes, while the optical phonons exhibit a finite energy [130].

In our case, a diode-pumped solid state laser emitting at $\lambda_R = 532\text{ nm}$ was used. The incident light was focused and collected by a microscope objective onto and from the sample. Magnification of 50x and the numerical aperture of $NA = 0.42$ was used. The spectra were recorded using a double spectrometer with a focal length of $2 \times 1\text{ m}$ and 2400 lines per mm grating. It was equipped with a liquid nitrogen-cooled charge-coupled device camera. Experimentally determined spectral resolution of this system was $\Delta\lambda_R = 0.006\text{ nm}$, corresponding to $\Delta\tau = 0.2\text{ cm}^{-1}$ at $\lambda_R = 532\text{ nm}$ [130].

4.1. Structure characterization techniques

A spinel structure is of the O_h^7 ($Fd\bar{3}m$) space group. Factor group analysis predicts the following modes in ZnFe_2O_4 spinel [131]:

$$A_{1g}(R) + E_g(R) + F_{1g} + 3F_{2g}(R) + 2A_{2u} + 2E_u + 4F_{1u}(IR) + 2F_{2u} \quad (4.7)$$

At room temperature, it is expected to exhibit five first order Raman active modes ($A_{1g} + E_g + 3F_{2g}$). In cubic spinels, the modes above 600 cm^{-1} (A_{1g}) would correspond to symmetric stretch of oxygen atoms of the tetrahedral (AO_4) symmetry, while the low frequency modes correspond to the symmetric and asymmetric bending of oxygen with respect to the cations of octahedral (BO_6) symmetry [128, 131, 132]. An exemplary spectra for the O375 sample as well as a schematic depiction of asymmetric bending and symmetric stretching vibrational phonon modes are shown in Figure 4.5. From the positions of the corresponding peaks as well as their width, as compared to literature values, an estimation of the crystalline symmetry can be established. The Raman spectra measurements were conducted by C. Kranert and C. Sturm at the Felix Bloch Institute for Solid State Physics, Universität Leipzig.

4.2 Surface properties

Information related to the surface of our thin films was obtained by atomic force microscopy (AFM) and X-ray photoelectron spectroscopy (XPS). While the surface morphology, obtained by AFM, hints to the possible film growth mode discussed in Section 3.1, XPS provides information about its elemental composition and chemical state.

4.2.1 Atomic force microscopy

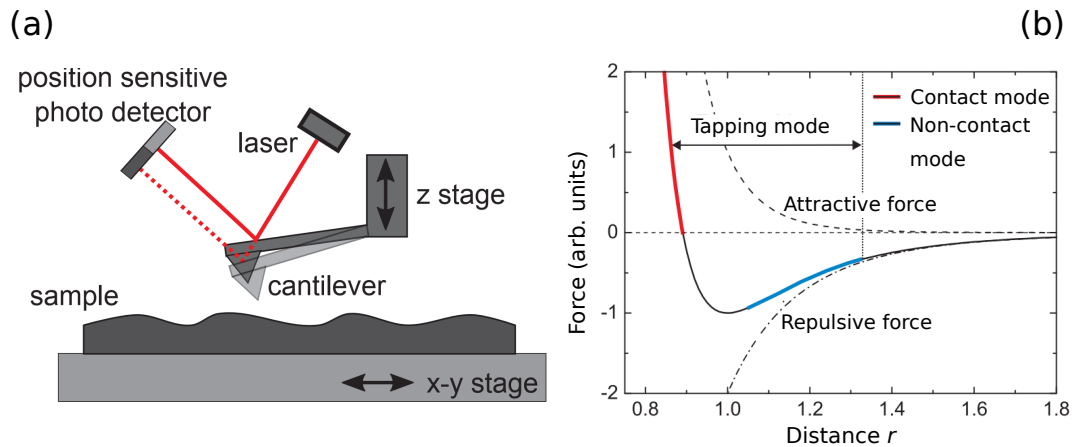


Figure 4.6: (a) Schematic representation of the basic principle of the AFM technique. (b) Force as a function of distance r between the cantilever and the surface atoms in contact and non-contact operational modes. The image was adopted from [51].

The film surface morphology scans were recorded using a Park System Xe-150 atomic force microscope (AFM) [133]. The schematic of its operational principle is depicted in Figure 4.6(a). The tip of a silicon cantilever scans over the sample surface at a close proximity. The attractive force between the tip and the surface causes the cantilever to deflect towards the surface. When the cantilever is brought in contact with the surface, the repulsive force dominates and the cantilever is deflected away, see Figure 4.6(b). In this case, the operational mode is the contact mode. However, taking advantage of both the attractive and repulsive forces, exerted by the surface, the tip can remain close to the surface during a scan of the non-contact operational mode. The change in the laser beam position of the tip is detected by a position-sensitive photo diode (PSPD) and the corresponding changes are related to the height of the surface features. The

4.2. Surface properties

x-y stage allows the sample to be moved back and forth with high precision and two images are obtained as one line of a two-dimensional topographic map.

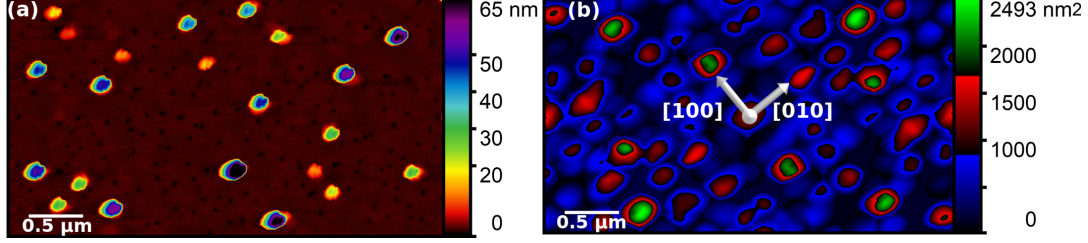


Figure 4.7: (a) Exemplary surface morphology scan of the ZnX0 film. (b) The 2-D autocorrelation analysis of the grains in (a). The predominant grain formation directions are indicated.

The scans, with a resolution of 512×512 , were analyzed by an open-source Gwyddion software [134]. In order to quantify the roughness of the surface, the root-mean-square (RMS) roughness (σ) was calculated and is given as:

$$\sigma = \sqrt{\frac{1}{MN} \sum_{m=1}^M \sum_{n=1}^N (z(x_m, y_n) - \langle z \rangle)^2} \quad (4.8)$$

where $z(x_m, y_n)$ is the height at a position (m, n) and $\langle z \rangle$ is the average height value. The initial image, obtained by the device, is prone to contain errors and noise, which arise from the instrument. Specifically, if the surface morphology is very smooth ($\text{RMS} \leq 2 \text{ nm}$). Therefore, the software allows options to thoroughly correct the image in order to improve the quality of the obtained scan. Furthermore, an analysis of the surface grains is possible and their distribution across the scan is examined by the 2-D autocorrelation function. In the case of an AFM image, the autocorrelation function, similar to the height-height correlation function, is given by:

$$\begin{aligned} G(\tau_x, \tau_y) &= \iint_{-\infty}^{\infty} z_1 z_2 w(z_1, z_2, \tau_x, \tau_y) dz_1 dz_2 \\ &= \lim_{S \rightarrow \infty} \frac{1}{S} \iint_S \xi(x_1, y_1) \xi(x_1 + \tau_x, y_1 + \tau_y) dx_1 dy_1 \end{aligned} \quad (4.9)$$

where z_1 and z_2 are values of heights at points (x_1, y_1) , (x_2, y_2) ; furthermore, $\tau_x = x_1 - x_2$ and $\tau_y = y_1 - y_2$. The function $w(z_1, z_2, \tau_x, \tau_y)$ denotes the two-dimensional probability density of the random function $\xi(x, y)$, corresponding to points (x_1, y_1) , (x_2, y_2) and the distance between these points τ [134]. An exemplary surface morphology scan for the ZnX0 film as well as the 2-D autocorrelation

image are shown in Figure 4.7. Therefore, apart from the surface roughness, the analysis of the AFM scans gives an indication of the possible type of film growth and allows determination of the predominant directions of grain formation.

4.2.2 X-ray photoelectron spectroscopy

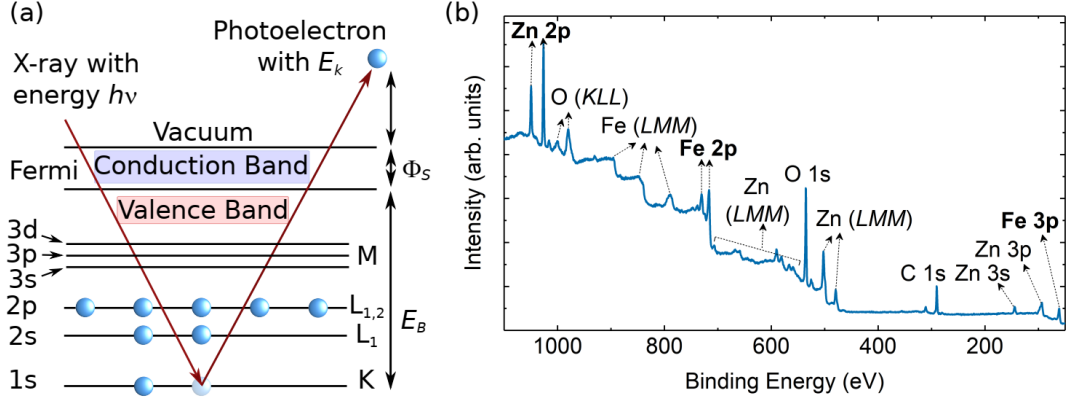


Figure 4.8: (a) Simplified illustration of the operational principle of XPS. (b) Survey spectra for the ZnX4 sample with each visible core level indicated. The core levels, which are examined in detail within the scope of this investigation are indicated in bold.

The elemental composition of the near-surface region was examined using X-ray photoelectron spectroscopy (XPS). The operational principle of the technique is depicted in Figure 4.8(a). The sample surface is irradiated with an X-ray of known energy ($h\nu$), in our case K_α radiation source (1486.6 eV) on an ESCALAB 220Xi X-ray photoelectron spectrometer. The measurements are performed at UHV conditions with the base pressure of 5×10^{-9} mbar. The kinetic energy (E_K) of the emitted electron, from a surface of a solid sample, is given by:

$$E_K = h\nu - E_B - \Phi_S \quad (4.10)$$

where Φ_S is the work function, specific to the detector of the instrument, and h as well as ν are the Planck's constant and frequency of the X-rays, respectively. The intensity distribution is due to overlapping electronic excitations contribution, specific to the chemical environment of the near-surface region. The excitation peaks at characteristic binding energies (E_B) are used to identify the electron configuration of the corresponding element involved. An exemplary survey spectra (0-1100 eV) for the ZnX4 film is shown in Figure 4.8(b) with each core level

4.2. Surface properties

indicated. The survey and detailed spectra were recorded with a pass energy of 50 and 10 eV and a dwell time of 100 and 300 ms, respectively.

The electrons, ejected from the s sub-shells, appear as chemically shifted primary peaks. On the other hand, the electrons, ejected from core levels with symmetries, such as p and d, often appear as doublet states. In order to obtain the precise position of the investigated core levels, the C 1s peak, located at 285 eV, is appropriately used as binding energy axis reference for the energy scale calibration. In addition to inelastic energy loss processes, secondary peaks, due to Auger transitions, shake-up and shake-off energy loss processes, contribute to the spectrum background. Therefore, a correct choice and description of the spectrum background is vital to the quality of the analysis. Although a simple line model is widely used for this purpose, the Shirley function background provides a more accurate description [135]. The modeling of the Zn 2p as well as the Fe 2p and 3p core levels, exemplary depicted in Figure 4.9 for the ZnX0 thin film, was performed using the UNIFIT software [136] by P. Huth at Wilhelm Ostwald Institute for Physical and Theoretical Chemistry, Universität Leipzig.

The intensity distribution of the Fe 2p and 3p core level spectra can be interpreted on the basis of multiplet splitting. Calculations of a p core level multiplet were conducted by Gupta and Sen by considering the electrostatic and spin-orbit interactions and using the Hartee-Fock approximation of the free Fe ion [137]. This approach was adopted by McIntyre to develop a general estimate of individual cation contribution to both core levels [138]. Alternatively, by examining the evolution of the XPS Fe 2p and 3p core level spectra, with respect to the structure of Fe₂O₃ to Fe₃O₄ films, Fujii *et al.* [139] were able to distinguish between the three site-specific Fe_{Td}³⁺, Fe_{Oh}³⁺ and Fe_{Oh}²⁺ cation contributions. Particularly, the final state shake feature, located between the Fe 2p_{3/2} and 2p_{3/2} peaks, is due to the overlapping satellite contribution of each cation state. In the case of magnetite, namely the ZnX0 sample, where contributions from the Fe cation species overlap, the satellite feature is broad and is not apparent in the spectra. However, in a structure containing predominantly Fe²⁺ (e.g. FeO) this feature would be present at a lower binding energy than the structure with predominantly Fe³⁺ (e.g. Fe₂O₃ or ZnFe₂O₄). Therefore, the presence and position of the satellite contribution hints to the dominating valence state of Fe and is commonly used to distinguish between FeO, Fe₂O₃ and Fe₃O₄ ferrites [8].

Nevertheless, a precise determination and quantification of the site- and valence-specific Fe cation contribution remains technically challenging. Commonly X-ray absorption spectroscopy as well as X-ray magnetic circular dichroism (XMCD) is

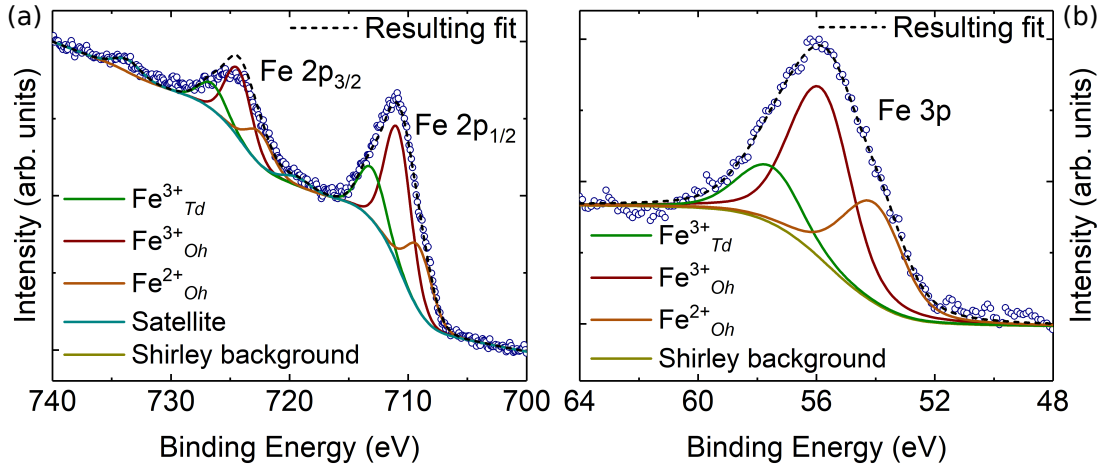


Figure 4.9: The experimental detailed XPS spectra as well as the modeled fit for (a) Fe $2p$ and (b) Fe $3p$ for the ZnX0 sample. The Shirley background as well as individual site- and valence-specific contributions to the core level approximations are color-coded.

used for this purpose. Recently, Aghavnian *et al.* [140] have demonstrated a fair agreement of the inversion parameter of inverse spinel CoFe_2O_4 by examining the XPS Co $2p$ and XMCD Fe $L_{2,3}$ edge spectra. However, the XMCD spectra did not provide sufficient information for quantitative analysis. Yuan *et al.* [141] reported site and valence specific ratios of the Fe cations and distinguished between the spin and orbital interaction. Torres *et al.* [35] and Zelis *et al.* [41], on the other hand, attribute both positive and negative XMCD peaks of the Fe L_3 edge spectra to only Fe^{3+} cations, located at tetrahedral and octahedral site, respectively. Groering *et al.* [43] has suggested that the situation might be more band-like due to the significant orbital moment of Fe^{3+} cations and that the integer Fe^{2+} and Fe^{3+} cation interpretation is not at all trivial.

In this investigation, both Fe $2p$ and $3p$ core levels were examined in order to obtain an approximate estimate of the individual cation presence in the near-surface region of our films. Based on the approach of Fujii *et al.* [139,142] and Yamashita *et al.* [143], a convolution of three Gaussian-Lorentzian functions was found to yield an appropriate match to the experimental Fe $2p$ and $3p$ core level spectra, Figure 4.9. Placed at binding energies, consistent with literature values and listed in Table 4.1, the three functions were sufficient to account for the features, associated with three Fe species. The Zn $2p$ core level was fit with a pair of Gaussian-Lorentzian functions [144]. The individual peak height ratio as well as peak separation was kept fixed according to database values. Through iterative fitting of the Shirley background as well as peak areas, and considering

4.2. Surface properties

the element specific photo-ionization sensitivity factor, the quantitative analysis of each Fe core level was conducted. The modeling of the XPS Fe 2p and 3p core levels allows an approximate estimation of the relative elemental composition of the Fe as well as Zn cations in near-surface region of our films.

Table 4.1: Binding energies (E_B) of Fe 3p, 2p_{1/2}, 2p_{3/2} core level maximum for the ZnX0 thin film. *The Zn 2p core level maximum binding energy is listed for the ZnX1 film. Binding energies of individual Fe cation contributions are listed for the approximation of the ZnX0 film Fe core level spectra.

Core level	E_B for ZnX0 (± 0.1 eV)	Fe _{Oh} ²⁺ (± 0.1 eV)	Fe _{Oh} ³⁺ (± 0.1 eV)	Fe _{Td} ³⁺ (± 0.1 eV)
Fe 3p	55.6	53.9	55.6	57.4
Fe 2p _{1/2}	711.0	709.1	710.9	713.1
Fe 2p _{3/2}	724.5	722.5	724.3	726.5
Zn 2p	1021.4*			

4.3 Dielectric tensor properties

Our understanding of the phenomenological origin of the light matter interaction has led to uncovering of the fundamental properties of countless materials. The primary aim of this investigation is to unveil the crystallographic nature as well as the electronic structure of spinel ferrites by examining this interaction. The theoretical principles, which govern this interaction, are discussed in this section.

Dielectric tensor and light propagation

The propagation of light in a material is characterized by macroscopic optical properties, which can be described by the dielectric function tensor, $\bar{\epsilon}(\vec{k}, \omega)$, given by [145]:

$$\vec{D}(\vec{k}, \omega) = \epsilon_0 \bar{\epsilon}(\vec{k}, \omega) \vec{E}(\vec{k}, \omega) \quad (4.11)$$

where the electric displacement vector $\vec{D}(\vec{k}, \omega)$ and the electric field vector $\vec{E}(\vec{k}, \omega)$ are expressed in momentum space and ϵ_0 is the vacuum permittivity. For a non-magnetic material, the tensor elements of $\bar{\epsilon}$ obey $\epsilon_{ij} = \epsilon_{ji}$, and therefore, the symmetric dielectric tensor can be transformed to the diagonal form with $\epsilon_{ij} = \epsilon_i \delta_{ij}$ where $i = (x, y, z)$ and δ_{ij} is the Kronecker symbol. For materials that are not optically active, the spatial dispersion can be neglected and $\bar{\epsilon}(\vec{k}, \omega)$ can be represented as $\bar{\epsilon}(\omega)$:

$$\bar{\epsilon}(\omega) = \begin{pmatrix} \epsilon_{xx}(\omega) & 0 & 0 \\ 0 & \epsilon_{yy}(\omega) & 0 \\ 0 & 0 & \epsilon_{zz}(\omega) \end{pmatrix} \quad (4.12)$$

Optical material character, namely biaxial, uniaxial and isotropic, is distinguished by the propagation of plane waves in three Cartesian planes. In the case of a biaxial material, polarization state is dependent on the propagation direction, and $\epsilon_{xx} \neq \epsilon_{yy} \neq \epsilon_{zz}$. For an optically uniaxial material, the plane wave propagates with the same velocity in two out of three directions, therefore $\epsilon_{xx} = \epsilon_{yy} \neq \epsilon_{zz}$. In this case, light polarization of the two eigenmodes is perpendicular ($\epsilon_{xx,yy}$) and parallel (ϵ_{zz}) to the optical axis. Since light propagates with the same velocity in any given direction of an optically isotropic crystal, as in our case, the dielectric tensor reduces to a scalar and the $\epsilon_{xx} = \epsilon_{yy} = \epsilon_{zz}$ relation holds.

The dielectric tensor element is represented by a complex function, given as:

4.3. Dielectric tensor properties

$$\epsilon(\omega) = \epsilon_1(\omega) + i\epsilon_2(\omega) \quad (4.13)$$

where the real term (ϵ_1) is related to the propagation of light, and the imaginary term (ϵ_2) is related to the energy dissipation into the material due to absorption. Both terms are related to the index of refraction (n) and extinction coefficient (κ):

$$\epsilon_1 = n^2 - \kappa^2 \text{ and } \epsilon_2 = 2n\kappa \quad (4.14)$$

Inverting these equations yields:

$$n = \sqrt{\frac{\sqrt{\epsilon_1^2 + \epsilon_2^2} + \epsilon_1}{2}} \text{ and } \kappa = \sqrt{\frac{\sqrt{\epsilon_1^2 + \epsilon_2^2} - \epsilon_1}{2}} \quad (4.15)$$

Interpretation of the optical properties

The real and imaginary terms of the DF are not independent and are related by dispersion relationship, namely the Kramers-Kronig relation [146]:

$$\epsilon_1(\omega) = 1 + \frac{2}{\pi} P \int_0^\infty \frac{\omega' \epsilon_2(\omega')}{\omega'^2 - \omega^2} d\omega' \quad (4.16)$$

$$\epsilon_2(\omega) = -\frac{2\omega}{\pi} P \int_0^\infty \frac{\epsilon_1(\omega') - 1}{\omega'^2 - \omega^2} d\omega' \quad (4.17)$$

where ω and ω' are real angular frequencies and P denotes the principal value of the integral.

The origin behind the classical interpretation is the work of Lorentz and Drude. The quantum mechanical description yields the same mathematical expressions for the dielectric function, but with a reinterpretation of the parameters. While the Lorentz oscillator model is applicable to insulators and semiconductors, the Drude model provides a good description of the free electron response in metals [146].

The optical and phononic characteristics of metals, or semiconductors are due to a combination of bound and free electron behaviors. The two types of optical characteristics can be expressed for metallic, semiconducting or insulating materials in a general form as:

$$\epsilon_1(\omega) = \epsilon_{0s} - \frac{N_{ef}e^2}{\epsilon_0 m(\omega^2 + \gamma_f^2)} + \frac{e^2}{\epsilon_0 m} \sum_n \frac{N_{eb,n}(\omega_n^2 - \omega^2)}{(\omega_n^2 - \omega^2)^2 + \gamma_n^2 \omega^2} \quad (4.18)$$

$$\epsilon_2(\omega) = \frac{N_{ef}e^2\gamma_f}{\epsilon_0m\omega(\omega^2 + \gamma_f^2)} + \frac{e^2}{\epsilon_0m} \sum_n \frac{N_{eb,n}\gamma_n\omega}{(\omega_n^2 - \omega^2)^2 + \gamma_n^2\omega^2} \quad (4.19)$$

The sum rules can be employed to relate the optical properties of an optically isotropic material to the concentration of all the electrons that interact with the electric field:

$$\int_0^{\omega_c} \omega \epsilon_2(\omega) d\omega = \frac{\pi N_a e^2}{2\epsilon_0 m} Z_{eff}(\omega_c) \quad (4.20)$$

where N_a is the concentration of atoms and $Z_{eff}(\omega_c)$ is the number of electrons per atom contributing to the optical properties up to frequency ω_c .

Model dielectric function

In the transparent region, where no transitions take place, the Cauchy function provides an effective description of the optical response of a non-absorbing material. The approximation for the refractive index dispersion is given by:

$$n(\lambda_i) = A + \frac{B}{\lambda_i^2} + \frac{C}{\lambda_i^4} \quad (4.21)$$

where λ_i is the wavelength of incident light and A , B , and C are the Cauchy parameters [147].

In the visible to the vacuum-ultraviolet spectral range, where phononic excitations are not present, as in our case, the dielectric function is dominated by electronic transitions between ionic orbitals. Band-to-band transition contributions to the dielectric function line-shape can be expressed by analytical expressions for the joint density of states function close to the critical points. For a direct semiconductor, the lowest band-to-band transitions occur at the Γ -point of the Brillouin zone. The critical point model (CPM) of the 3D M_0 type appropriately describes the line-shape of the DF. It is based on the one-electron interband transition approach and parabolic band approximation, assuming energy independent momentum matrix elements [145, 148, 149]. The contributions to the dielectric function, of 3D M_0 -type, are given by:

$$\epsilon^{3DM_0}(E) = A_n E_n^{-1.5} \left(\frac{2 - (1 + \chi_n)^{0.5} - (1 - \chi_n)^{0.5}}{\chi_n^2} \right) \quad (4.22)$$

with $\chi_n = \frac{(E + i\Gamma_n)}{E_n}$

where A_n , E_n and Γ_n is the amplitude, transition energy and broadening param-

4.3. Dielectric tensor properties

eter of the CPM approximation, respectively. The term n is the running index of the actual transition and E is the photon energy. The significant absorption in the high energy range is attributed to transitions that are distributed across widely spread regions of the Brillouin zone.

As discussed in the previous section, discrete electronic transitions are well described by the Lorentzian model, applicable to semiconductors and insulators. In the framework of this discussion, the Lorentzian harmonic oscillator function provides an appropriate approximation for multiple adjoined transitions between discrete states and is given by:

$$\epsilon_{n,Lor}(E) = \frac{A_n \Gamma_n E_n}{E_n^2 - E^2 - i\Gamma_n E} \quad (4.23)$$

where A_n , E_n and Γ_n is the averaged amplitude, transition energy and broadening parameter, respectively with n being the running index [150]. Another function used to describe inhomogeneous parts of the system as well as electronic transitions due to the loss of charge carriers from scattering or absorption processes is the Gaussian model. In this case, the electronic transition contributions to the complex ϵ line-shape can be approximated by:

$$\begin{aligned} \epsilon_{n2}(E) &= A' e^{-\left(\frac{E-E_n}{\sigma}\right)^2} - A' e^{-\left(\frac{E+E_n}{\sigma}\right)^2} \\ \epsilon_{n1}(E) &= \frac{2}{\pi} P \int_0^\infty \frac{\xi \epsilon_{n2}(\xi)}{\xi^2 - E^2} d\xi \end{aligned} \quad (4.24)$$

where $\sigma = Br_n/2\sqrt{\ln(2)}$ defines the broadening parameter, and ξ is proportional to Br_n . In this case, A' is the dimensionless amplitude and E_n is the transition energy [151].

As will be discussed in Section 4.4, it was determined that the Lorentzian approximation function appropriately describes the energetically low electronic transitions, namely d-d interband transitions. For the rest of the measured spectral range, the Gaussian function approximation of the DF was employed to describe notably broad features, related to the sum of discrete electronic transitions, involving 3d and 4s orbitals. The CPM function gave an appropriate description of the high energy absorption and was most effective when located close to the assumed band-gap energy. A series of aforementioned approximations yields an adequate description of the material optical properties in the measured spectral range.

Magneto-optical tensor elements

So far, we have described the case for an optically isotropic material in the absence of magnetic field. However, in the presence of external magnetic field, the change in polarization of electromagnetic wave upon interaction with a magnetic medium no longer follows the diagonal representation 4.12 with $\epsilon_{xx} = \epsilon_{yy} = \epsilon_{zz}$. The effect which describes the change in the polarization of light through transmission is called the Faraday effect, and the change in ellipticity is known as magnetic circular dichroism [152]. The change in the polarization state upon reflection from a magnetic sample is known as the magneto-optical Kerr effect (MOKE) [153].

The magneto-optical activity is commonly expressed as the complex Kerr rotation, given by:

$$\Phi_K = \theta_K + i\eta_K = \frac{\omega}{2c} \tilde{n} Q d \quad (4.25)$$

where ω is the angular frequency of the electromagnetic field, c is the velocity of light, and \tilde{n} the complex index of refraction for the film with thickness d . The parameter, characteristic of the material, is known as the Voigt constant, Q . The real part (θ_K) of the complex Kerr rotation is related to the tilt angle of the main axis of polarization upon reflection from the sample, while the imaginary part (η_K) is ellipticity.

Considering the Onsager relation of symmetry conservation of the off-diagonal dielectric tensor components under time reversal, symmetry is kept only by reversing the magnetic field (B). Therefore, $\epsilon_{ij}(B) = \epsilon_{ji}(-B)$ relation must hold. Under assumption that for $B = 0$, the off-diagonal components are zero, for $i \neq j$, each pair of symmetrical components will be proportional for \pm components of B [154, 155]. For B parallel to the sample normal, otherwise known as the polar MOKE, the dielectric tensor for a cubic system is expressed as:

$$\bar{\epsilon}(\omega) = \begin{pmatrix} \epsilon_{xx}(\omega) & \epsilon_{xy}(\omega) & 0 \\ -\epsilon_{xy}(\omega) & \epsilon_{xx}(\omega) & 0 \\ 0 & 0 & \epsilon_{xx}(\omega) \end{pmatrix} \quad (4.26)$$

where $\epsilon_{xx,xy}(\omega)$ terms are complex quantities. The off-diagonal component of the dielectric tensor can then be expressed as $\epsilon_{xy}(\omega) = Q \epsilon_{xx}(\omega)$, where Q is the Voigt constant.

The microscopic picture can be interpreted by considering the susceptibility tensor approximation in the Cartesian representation. The electric dipole ap-

4.3. Dielectric tensor properties

proximation can be modified to the case where the medium is characterized by a magnetic susceptibility tensor, using the duality principle [156]. In the case of isotropic coupling, and with the magnetic field B applied parallel to the radiation propagation vector, the dielectric tensor can be described by a sum of Lorentz oscillator functions with different resonant frequencies, ω_{0k} , given by:

$$\epsilon_{xx}(\omega) = \sum_k f_k \frac{\omega_{0k}^2 - \omega^2 - i\omega\Gamma_k}{(\omega_{0k}^2 - \omega^2 - i\omega\Gamma_k)^2 - 4\omega^2\omega_{Lk}^2} \quad (4.27)$$

$$\epsilon_{zz}(\omega) = \sum_k \frac{f_k}{\omega_{0k}^2 - \omega^2 - i\omega\Gamma_k} \quad (4.28)$$

$$\epsilon_{xy}(\omega) = \sum_k \frac{-2i\omega\omega_{Lk}}{(\omega_{0k}^2 - \omega^2 - i\omega\Gamma_k)^2 - 4\omega^2\omega_{Lk}^2} = -\epsilon_{yx}(\omega) \quad (4.29)$$

where f_k is the weight factor, Γ the damping constant, and ω_{Lk} the Larmor frequency. In the case of metals, where the free electrons are modeled by Lorentz function with zero resonant frequency, the above components are expressed as:

$$\epsilon_{xx}^{(D)} = -f_D \frac{\omega + i\Gamma_D}{\omega[(\omega + i\Gamma_D)^2 - 4\omega_{LD}^2]} = \epsilon_{yy}^{(D)} \quad (4.30)$$

$$\epsilon_{zz}^{(D)} = \frac{-f_D}{\omega(\omega + i\Gamma_D)} \quad (4.31)$$

$$\epsilon_{xy}^{(D)} = -f_D \frac{2i\omega_{LD}}{\omega[(\omega + i\Gamma_D)^2 - 4\omega_{LD}^2]} = -\epsilon_{yx}^{(D)} \quad (4.32)$$

The case of ferromagnetic 3d metals and transition metals consists of both free and bound electrons and can be described by the aforementioned equations [156]. The classical interpretation of the spectral dependence of the susceptibility tensor gives a simplified insight into the microscopic picture. It employs both the Lorentzian and Drude model in order to describe the interband and intraband electronic transitions, which contribute to the magneto-optical activity of free and bound electrons in dependence on the applied frequency and magnetic field. However, in the configuration, where the light propagation vector is parallel to the magnetization or the wave is obliquely incident on the planar structure, the magneto-optical response can be handled analytically and the classical interpretation is valid. The detailed approach for modeling the response is presented in Section 4.5.

4.4 Spectroscopic ellipsometry

The principal material characterization technique in this investigation is spectroscopic ellipsometry. The non-invasive and precise optical method is continuously employed in various fields to extract material properties and their changes, such as detecting changes in nominal thickness with sub-monolayer accuracy. By examining the relative change in the polarization state of the incident electromagnetic plane wave upon reflection or transmission, and by model analysis interpretation, the optical properties of individual layers are obtained. The basic principles and the approach for determination of the diagonal elements of the dielectric tensor are presented in this section.

Standard spectroscopic ellipsometry

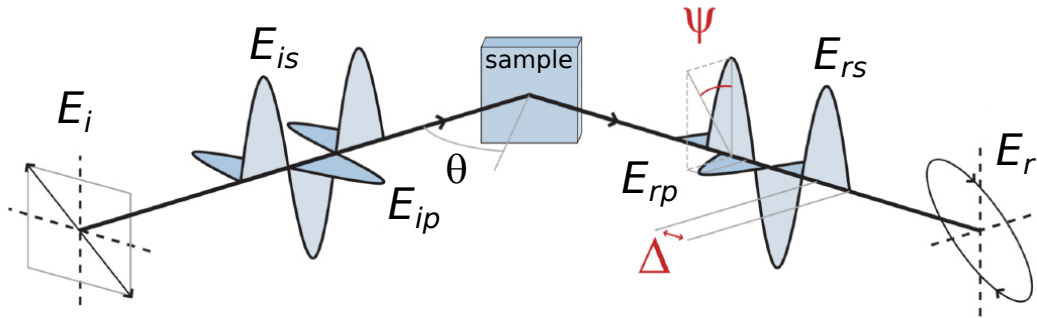


Figure 4.10: Schematic illustration of the operational principle of spectroscopic ellipsometry, adopted from [157]. The subscripts i and r correspond to incident and reflected electric field E of incidence angle of θ , while p and s correspond to its polarization state.

Spectroscopic ellipsometry (SE) detects the relative changes in the polarization state of electromagnetic plane wave upon reflection or transmission from the sample. Schematic representation of the operational principle is depicted in Figure 4.10. The incident light wave consists of orthogonal p - and s -polarization components, which correspond to the directions of the electric field vector that are parallel and perpendicular to the plane of incidence, respectively. Upon reflection, the changes in the wave polarization are manifested by the ratio of the amplitudes (Ψ) and difference in phase (Δ). The case of standard ellipsometry is applicable to an optically isotropic sample system, whereby the ellipsometric pa-

4.4. Spectroscopic ellipsometry

rameters, Ψ and Δ , are independent of the polarization state of the incident plane wave. In this case, the p - and s -polarization state of reflected light is sustained and no conversion of polarization state takes place [158]. The two ellipsometric parameters are related to the ratio of the p - and s -polarized complex Fresnel reflection coefficients, r_p and r_s , by:

$$\rho = \frac{r_p}{r_s} = \frac{E_{rp}/E_{ip}}{E_{rs}/E_{is}} = \tan \Psi e^{i\Delta} \quad (4.33)$$

The subscripts i and r correspond to incident and reflected electric field vector, while subscripts p and s represent p - and s -polarization state.

Alternative representation is the complex pseudo-dielectric function, $\langle \epsilon \rangle = \langle \epsilon_1 \rangle + i\langle \epsilon_2 \rangle$, which is related to the measured quantities Ψ and Δ by:

$$\langle \epsilon \rangle = \tan^2 \theta \left(\cos^2 \theta + \sin^2 \theta \left[\frac{1 - \rho}{1 + \rho} \right]^2 \right) \quad (4.34)$$

where θ is the angle of incidence [150]. The complex pseudo-dielectric function is equal to the material dielectric function for a semi-infinite material system bounded by air, considering no mode conversion upon reflection from the surface occurs.

A possible loss of polarization upon reflection can occur for an isotropic, but partially depolarizing sample. The depolarization quantity is then given by:

$$\%Depolarization = 100\%(1 - N^2 - C^2 - S^2) \quad (4.35)$$

where $N = \cos(2\Psi)$, $C = \sin(2\Psi) \cos(\Delta)$ and $S = \sin(2\Psi) \sin(\Delta)$. Further measured quantities are given by:

$$\begin{aligned} \Psi_{depol} &= \frac{1}{2} \arctan \frac{\sqrt{(S^2 + C^2)}}{N} \\ \Delta_{depol} &= \arctan \frac{S}{C} \end{aligned} \quad (4.36)$$

However, the approach, presented in the next section, allows a more thorough collection and interpretation of information for a sample, such as an anisotropic material or one with high degree of depolarization.

Generalized spectroscopic ellipsometry

The measurement of the complex ratio ρ can be addressed by different interpretations of the electromagnetic plane wave response from the sample. In contrast to the description of an isotropic system, both standard and generalized ellipsometry approaches describe the change in polarization state based on the Jones vector formalism. Consistent with the notation above, where the electric field vector E is incident (i) or reflected (r) and either p - or s -polarized, the polarization states of the incident and reflected wave are related by the Jones matrix \mathbf{j} :

$$\begin{pmatrix} E_{rp} \\ E_{rs} \end{pmatrix} = \mathbf{j} \begin{pmatrix} E_{ip} \\ E_{is} \end{pmatrix} = \begin{bmatrix} j_{pp} & j_{sp} \\ j_{ps} & j_{ss} \end{bmatrix} \times \begin{pmatrix} E_{ip} \\ E_{is} \end{pmatrix} \quad (4.37)$$

where j_{ps} and j_{sp} vanish in the case of an isotropic material. The reflection coefficients (" j_{ps} " = " r_{ps} ") are related to the generalized ellipsometry parameters:

$$\frac{j_{pp}}{j_{ss}} = \tan \Psi_{pp} \exp(i\Delta_{pp}), \frac{j_{ps}}{j_{pp}} = \tan \Psi_{ps} \exp(i\Delta_{ps}), \frac{j_{sp}}{j_{ss}} = \tan \Psi_{sp} \exp(i\Delta_{sp}) \quad (4.38)$$

The real-valued quantities $\Psi_{pp,ps,sp}$ and $\Delta_{pp,ps,sp}$ comprise the generalized ellipsometry data presentation within the Jones matrix formalism. [159] This is sufficient if neither the sample, nor the optical components of the apparatus depolarize the light beam. In particular, for systems which convert the s -waves into p -waves and vice versa, the off-diagonal elements of the Jones matrix are non-zero and the interpretation becomes less trivial. A more general description is the Stokes vector formalism, where the real-valued matrix elements connect the Stokes parameters of the electromagnetic plane waves before and after sample interaction [160]. The Stokes parameters can be directly measured, and for the p - s system are defined as:

$$S_0 = I_p + I_s, S_1 = I_p - I_s, S_2 = I_{45} - I_{-45}, S_3 = I_{\sigma+} - I_{\sigma-} \quad (4.39)$$

where I_p , I_s , I_{45} , I_{-45} , $I_{\sigma+}$, and $I_{\sigma-}$ denote the intensities for the p -, s -, $+45^\circ$, -45° , right-, and left-circularly polarized light components, respectively. [161] The S_0 component is proportional to the total intensity of the light beam, and the inequality $S_0 \geq \sqrt{S_1^2 + S_2^2 + S_3^2}$ gives a measure of the degree of polarization, while equality holds for totally polarized light. The change of the Stokes-vector upon interaction with the non-depolarizing system and an optically isotropic sample is

4.4. Spectroscopic ellipsometry

described by:

$$\begin{pmatrix} S_0 \\ S_1 \\ S_2 \\ S_3 \end{pmatrix}_{Out} = \begin{pmatrix} 1 & -N & 0 & 0 \\ -N & 1 & 0 & 0 \\ 0 & 0 & C & S \\ 0 & 0 & -S & C \end{pmatrix} \times \begin{pmatrix} S_0 \\ S_1 \\ S_2 \\ S_3 \end{pmatrix}_{In} \quad (4.40)$$

where $N = \cos(2\Psi)$, $C = \sin(2\Psi) \cos(\Delta)$ and $S = \sin(2\Psi) \sin(\Delta)$. Whereby, the constraint $1^2 + C^2 + S^2 = 1$ must hold [162]. The complex reflectivity coefficient ratio is given by:

$$\rho = \frac{C + iS}{1 + N} \quad (4.41)$$

Important to note, depending on the measurement system either some or all Jones matrix elements of the sample system can be determined [163]. In our case, with a system in a polarizer-compensator-sample-analyzer (PCSA) configuration, all matrix elements, apart from the fourth row, are measured. Following the Jones formalism, the contribution of each of the components of the experimental set-up, namely, the analyzer (*an*), compensator (*comp*) and polarizer (*pol*), are multiplied:

$$S_{out} = \mathbf{j}_{an} \mathbf{j}_{an}^{rot} \times \mathbf{j}_{sample} \times \mathbf{j}_{comp} \mathbf{j}_{comp}^{rot} \times \mathbf{j}_{pol} \mathbf{j}_{pol}^{rot} \times S_{in} \quad (4.42)$$

Additional contribution also arises from the windows of the cryostat installment in the case of temperature dependent measurements.

Vacuum Ultraviolet VASE

The primary measurement system for optical characterization of the investigated thin films, was the commercially available J. A. Woollam Vacuum Ultraviolet Variable Angle Spectroscopic Ellipsometer. Measurements were conducted in a NIR-VUV spectral range (0.5-8.5 eV) and in ambient conditions. The measurement system employs a Xenon lamp (0.5-6.5 eV) and a Deuterium lamp for the VUV spectral range (6.5-8.5 eV). A grating is used for setting the appropriate wavelength prior to reflection from the sample. The reflected beam is detected by a photomultiplier tube in the UV-VUV range (4.1-8.5 eV), while the Si-InGaAs tandem detector is used in the NIR-UV range (0.5-6.5 eV). The samples as well as the device components are dry-nitrogen-purged prior to measurement in order to prevent light absorption in the VUV spectral range by atmospheric oxygen and

water content. A cryostat installment allows measurements to be done in the temperature range from 5 to 700 K with the help of Helium cooling of the sample holder. The measurements were conducted at 60 and 70° angles of incidence, and with a spectral resolution of either 100 meV or 50 meV as well as a minimum of 100 averages per data point. Upto 5 samples can be mounted on the sample holder, held by a vacuum pump. In that case, the measurements are then done with an automated script, with sample alignment prior to data acquisition.

Maintenance procedures ensure minimal acquisition errors and higher detected intensity and thus a broader spectral range. Prior to the measurement set, the Xe and D₂ lamp intensity is maximized in order to decrease acquisition time and increase the accuracy of the measured data. Furthermore, regular detector calibration scripts were compiled in order to monitor the status of the system. The beam alignment procedure was then conducted, if necessary. Prior to every measurement set, a bulk Si sample with 25 Å SiO₂ surface layer was used to calibrate the system at three wavelengths, distributed across the available spectral range. The calibration parameters of individual system components were tuned to minimize the error of the calibration and thus improve the accuracy of the acquired data.

Acquisition data analysis

The general approach to determine the physical information, such as the optical properties and thickness of the investigated thin film layer, requires an analytical description of the system. An appropriate transfer matrix analysis for a layer stack model was employed to represent the whole sample and to generate an accurate description of the measured quantities. In the case of a single thin film layer, the model is composed of a semi-infinite substrate, the thin film and a surface layer.

The optical properties of the substrate were determined in the same spectral range and ambient conditions prior to deposition of the thin film. The surface layer was described by an effective medium approximation (EMA) function. Its thickness was correlated to the RMS of the surface roughness, determined from AFM measurements. The EMA also takes into account the relative amount of film structures that were present in the surface layer, which was correlated to the grain analysis of the surface morphology scans.

In order to quantify the quality of the match, between the calculated model data and the experiment, the following maximum likelihood estimator, the mean-

4.4. Spectroscopic ellipsometry

squared error (MSE), is used:

$$\begin{aligned}
 MSE &= \sqrt{\frac{1}{2N - M} \sum_{i=1}^N \left[\left(\frac{\Psi_i^{mod} - \Psi_i^{exp}}{\sigma_{\Psi,i}^{exp}} \right)^2 + \left(\frac{\Delta_i^{mod} - \Delta_i^{exp}}{\sigma_{\Delta,i}^{exp}} \right)^2 \right]} \\
 &= \sqrt{\frac{1}{2N - M} X^2}
 \end{aligned} \tag{4.43}$$

where N is the number of (Ψ, Δ) pairs, M is the number of variable parameters in the model, and σ are the standard deviations on the experimental data points. The chi-square (X^2) is defined for comparison [150]. The MSE did not exceed the value of 2 during the fitting procedure for all spectra of the investigated thin films.

Initial description of the DF line-shape was conducted by a numerical approximation, namely the B-spline function. This function is defined by a series of polynomial segments, which are constructed to maintain continuity up to a certain derivative degree [164]. The basic definition of the B-spline function $B_i^k(x)$ is expressed as:

$$\begin{aligned}
 B_i^0(x) &= \begin{cases} 1 & t_i \leq x \leq t_{i+1} \\ 0 & \text{otherwise} \end{cases} \\
 B_i^k(x) &= \left(\frac{x - t_i}{t_{i+k} - t_i} \right) B_i^{k-1}(x) \left(\frac{t_{i+k+1} - x}{t_{i+k+1} - t_i} \right) B_{i+1}^{k-1}(x)
 \end{aligned} \tag{4.44}$$

where the superscript k denotes the degree of the B-spline, and the superscript i indexes the knot locations t_i . In this sense, knots are interpreted as nodes on the x -axis where the curve transitions from one polynomial segment to another. The B-spline curve $S(x)$ is then defined as a linear sum of n basis functions, in which c_i are the spline coefficients for the i -th basis function:

$$S(x) = \sum_{i=1}^n c_i B_i^k(x) \tag{4.45}$$

The numerical approximation of the dielectric function is primarily used for the determination of the thickness of the film layer. While the XRR determines the film thickness, based on the mass density of the layer, and SEM allows estimation based on the contrast of conducting electrons, the B-spline function yields an optical thickness, which deviates by a few nm from the former methods. Depending on the placement of the nodes, a practical description of the dielectric function

line-shape can be achieved [164–167]. The fit of the numerical approximation to the experimentally obtained ellipsometric quantities, Ψ and Δ , is shown exemplary for the ZnX3 thin film in Figure 4.11 (a) and (b).

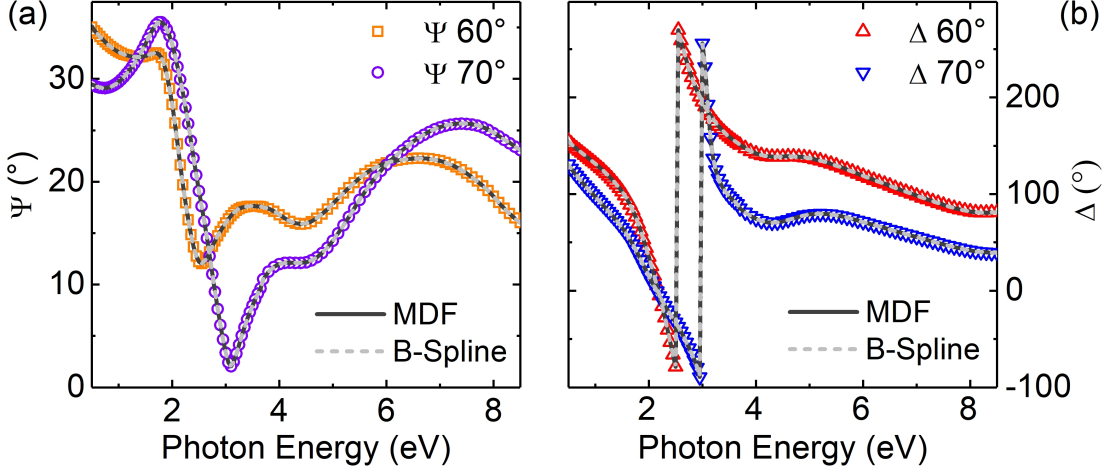


Figure 4.11: Experimentally obtained ellipsometric parameters (a) Ψ and (b) Δ of the ZnX3 thin film for 60° and 70° angles of incidence as well as the numerical (B-Spline) and numerical (MDF) approximation of the measured data are shown.

The line-shape of the imaginary part of the complex dielectric function, determined by the numerical B-spline approximation, and depicted for the spinel ferrite ZnX3 film in Figure 4.12, is used as a starting point for its parametrization. The parametric approximation of the complex dielectric function is referred to as the model dielectric function (MDF). It consists of a series of Kramers-Kronig consistent function approximations, presented in Section 4.3, which are distributed over the measured spectral range.

The critical point model (CPM_0) is placed at the energy of a band-to-band transition at the Γ -point of the Brillouin zone and provides an appropriate description of the onset of absorption in the high energy range. The Lorentzian function approximation is used to describe the narrow feature in the energy range below 1 eV. The remaining eight Gaussian oscillators are necessary to describe the spectral features of this material. Only G_1 , G_2 and G_4 functions are placed at energies, consistent with literature values, namely 2.0, 2.6 and 3.9 eV, respectively. The rest of the functions are located in the vicinity of the literature values, however their assignment to individual electronic transitions remains controversial. Based on the iterative fitting of the DF line-shape of ZnFe_2O_4 films, within the scope of this investigation, a significant amount of information has been gathered empirically and patterns became apparent. The function approximations, depicted in Figure 4.12, were required for a precise description of the DF in the measured

4.4. Spectroscopic ellipsometry

spectral range. Spectral position as well as the assigned electronic transitions are listed in Table 4.1 for ZnX0, ZnX2 and ZnX4 samples with Zn content of 0, 0.56 and 1.26, respectively. The approximation energy and strength in dependence on the fabrication and modification parameters as well as the Zn content will be discussed in more detail in the following chapters.

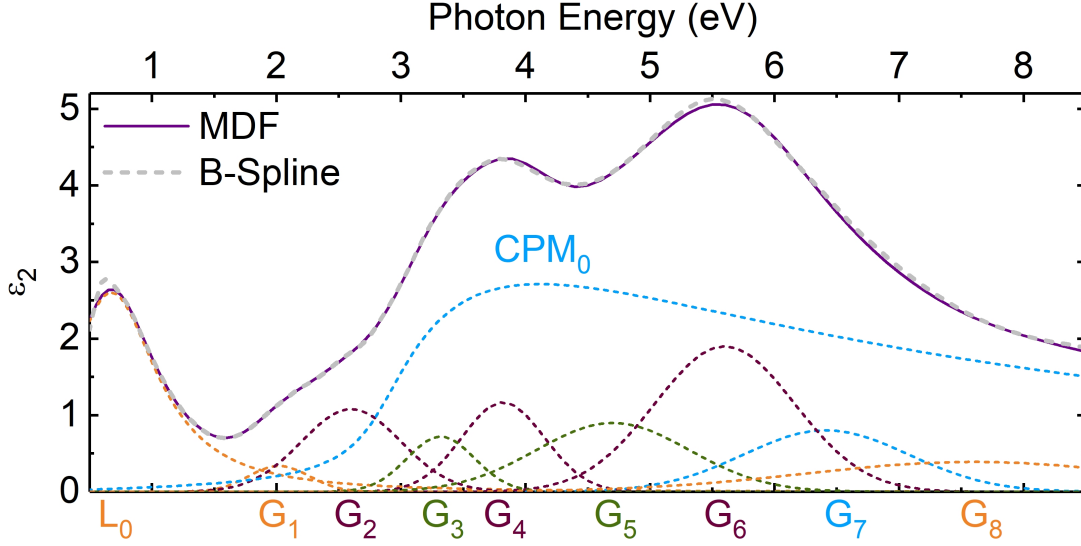


Figure 4.12: Parametric (straight line) and numerical DF (short dash line) with individual contributions as indicated for the ZnX3 thin film.

Furthermore, the high number of free function parameters, defining the MDF line-shape, makes the uniqueness of the set of values not at all trivial. If we consider the MSE as a surface, defined in an M -dimensional space where M is the number of variable model parameters, then we are attempting to evaluate the gradient of the MSE surface with the starting point, defined by the current set of values [150]. The data evaluation software employs the Levenberg-Marquardt algorithm for the minimization of the analysis model, which adjusts the values of variables in order to decrease the MSE. However, the initial guess for the set of parameters is not broad enough and the algorithm is likely to settle on a local minima of the MSE surface. Within the scope of this investigation, and through iterative approximation of the MDF line-shape for the spinel ferrite material, the number of free variables was decreased. Thereby, the range of possible values was limited for some of the parameters, based on the empirical evidence. For example, the energies for ZnX0 and ZnX4, listed in Table 4.2, were chosen as the constraining values, limiting the position parameters of the oscillator functions. In this sense, the remaining set of non-constraint variable parameters was chosen as the initial set for the Levenberg-Marquardt algorithm in order to find the most unique

4.4. Spectroscopic ellipsometry

solution that describes the material MDF line-shape approximation. Increasing the sample set for analysis as well as correlating the quantitative composition approximation from the DF to alternative methods, such as XMCD, Mössbauer spectroscopy, or theoretical approximations could strengthen the proposed approach by improving the choice of the initial set of parameters. However, the spectroscopic composition estimation, as well as a correlation of the theoretical description to experimental findings both remain challenging and non-trivial.

Table 4.2: Photon energies are listed for the assigned electronic transitions. Corresponding cations and anions involved are indicated for each (L) Lorentzian, (G) Gaussian and (CPM) Critical Point Model function. The estimated error for the specified energy values is in the range of the last digit.

Osc.	Transition	ZnX0 (eV)	ZnX2 (eV)	ZnX4 (eV)
L ₀	(Fe _{Oh} ²⁺)d t _{2g} - (Fe _{Oh} ²⁺)d t _{2g}	0.63	0.79	0.94
G ₁	(Fe _{Oh} ²⁺)d t _{2g} - (Fe _{Oh} ³⁺)d e _g	2.04	2.07	2.09
G ₂	O 2p - (Fe _{Oh} ³⁺)3d t _{2g}	2.59	2.57	2.60
CPM ₀	(Zn _{Td} ²⁺)	2.87	2.87	2.89
G ₃	O 2p - (Fe _{Td} ³⁺)3d e	3.15	3.25	3.37
G ₄	O 2p - (Fe _{Oh} ³⁺)3d e _{2g}	3.82	3.96	3.88
G ₅	O 2p - (Fe _{Td} ³⁺)4s	4.65	4.91	4.87
G ₆	O 2p - (Fe _{Oh} ³⁺)4s	5.65	5.70	5.68
G ₇	O 2p - (Zn _{Td} ²⁺)4s	6.48	6.48	6.48
G ₈	O 2p - (Fe _{Oh} ²⁺)4s	7.00	7.00	7.41

4.5 Magneto-optical Kerr effect

The description of the off-diagonal elements of the dielectric tensor provides valuable understanding of the phenomenological nature of the electronic transitions. The non-destructive technique examines the change of the polarization of light upon reflection from a material in the presence of an external magnetic field. The experimental set-up as well as the model approximation, used to describe the spectral dependence of the tensor elements, are presented in this section.

Experimental set-up

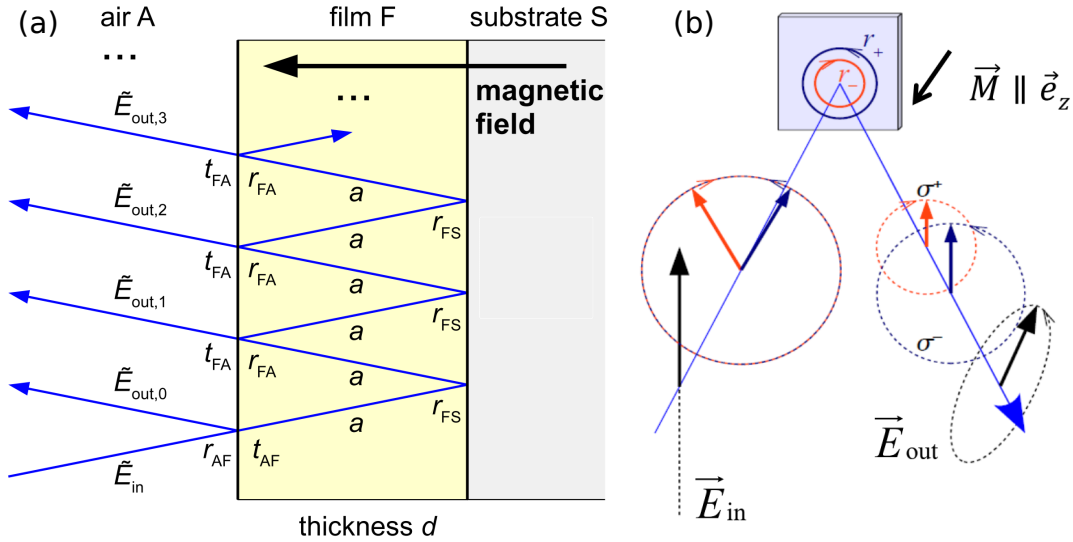


Figure 4.13: (a) Depiction of the three-layer model, taken from [153]. The Fresnel coefficients of the interfaces (r , t) and the propagation terms (a) are indicated. The electric field vectors of the outgoing radiation, \vec{E}_{out} , are summed up for right and left circularly polarized state separately, depicted in (b). (b) Depiction of the MOKE operational principle, where the right (red σ^+) and left (dark blue σ^-) circularly polarization states are indicated. For better visualization of the processes, the angle of incidence is shown to be larger than 0° in both images.

The magneto-optical response was measured in the spectral range from 1.7 to 5.5 eV with an applied field of 1.7 T in ambient conditions. The setup was a home-built magneto-optical Kerr effect (MOKE) setup, which allows measurements in polar geometry, with the angle of incidence of $\sim 1.3^\circ$. The measurements were conducted at Technical University of Chemnitz by P. Richter under the supervision of G. Salvan and D.R.T. Zahn.

4.5. Magneto-optical Kerr effect

The MOKE setup is similar to that described by Herrmann *et al.* [168]. The incoming light becomes *s*-polarized after passing through a polarizer. The reflected light beam then propagates through a photoelastic modulator and an analyzer before being detected by a photomultiplier. The change in the polarization state can be expressed by the complex Kerr rotation angle, Φ_K , given as:

$$\tilde{\Phi}_K = \theta_K + i \cdot \eta_K. \quad (4.46)$$

where θ_K represents the tilt angle of the main axis of polarization and η_K refers to the ellipticity of the reflected light.

The three-layer model is schematically depicted in Figure 4.13 (a). The Fresnel coefficients of light transmitted through, t , or reflected from, r , the interface at normal angle of incidence, are given by:

$$t = \frac{2\tilde{n}_1}{\tilde{n}_1 + \tilde{n}_2} \text{ and } r = \frac{\tilde{n}_1 - \tilde{n}_2}{\tilde{n}_1 + \tilde{n}_2} \quad (4.47)$$

where $\tilde{n} = n + ik$ is the complex index of refraction, denoted with index 1 for the medium where the light comes from or 2 for the medium which the light is going to or reflected from. The exponential attenuation of light due to propagation through the layer is given by:

$$a = \exp \left[i \left(\tilde{n} \frac{\omega}{c} d \right) \right] \quad (4.48)$$

By superimposing all reflected light beams, $\tilde{E}_{out,i}$, the sample effective reflection coefficient u is expressed by:

$$u = r_{AF} + \frac{t_{AF} \cdot t_{FA} \cdot a^2 \cdot r_{FS}}{1 - a^2 \cdot r_{FS} \cdot r_{FA}} \quad (4.49)$$

where the subscripts A , F and S denote air, film and substrate layer, respectively, as depicted in Figure 4.13 (a). The incident light can be considered as a composition of two polarized states, right (+) and left (-) circularly polarized, with certain phase relation, schematically depicted in Figure 4.13 (b). Since the magnetic field is normal to the sample surface plane and nearly parallel to the light propagation direction, the eigenmodes of the reflected light are circularly polarized as well [153], Figure 4.13 (b). The material optical constants can then be expressed as [153]:

$$\tilde{n}_{\pm} = \tilde{n} \left(1 \mp \frac{Q}{2} \right) \quad (4.50)$$

where Q is the Voigt constant, related to the magneto-optical activity of the

4.5. Magneto-optical Kerr effect

material, expressed as a ratio of the diagonal and off-diagonal dielectric tensor elements in Equation 4.26, described in Section 4.3. Furthermore, the effective reflection coefficient, u , would also consist of right (+) and left (-) circularly polarized components. And by using the Jones matrix formalism, the complex Kerr rotation angle Φ_K can be expressed as a function of u_{\pm} :

$$\Phi_K = \arctan \frac{i(u_+ - u_-)}{(u_+ + u_-)} \quad (4.51)$$

The experimental values θ_K and η_K are calculated from the above equations implemented in a Python script, developed by M. Fronk in the group of D.R.T. Zahn, in cooperation with D. Schmidt (Nebraska/Woollam Inc.) [153, 169].

Simulation model

The experimental MOKE spectra were imported into the WVASE program for analysis, based on the approach proposed by Schmidt *et al.* [170]. For a vanishing angle of incidence, the complex Kerr rotation is given by:

$$\tilde{\Phi}_K = \theta_K + i \cdot \eta_K = -\arctan \frac{r_{sp}}{r_{ss}} \quad (4.52)$$

The sign difference also holds between r_{sp} and r_{ss} . The ellipsometric values, of the type "Asp: Anisotropic Ellipsometry, r_{sp}/r_{ss} ratio", are then expressed by:

$$\begin{aligned} \Psi_{sp} &= \arctan |\rho| = \arctan |-\tan \Phi_K| \\ \Delta_{sp} &= -\arg(\rho) = -\arg(-\tan(\Phi_K)) \end{aligned} \quad (4.53)$$

The error, due to the data transformation, was estimated to be 10^{-4} and 10^1 for Ψ_{sp} and Δ_{sp} , respectively.

The model for approximation of the MOKE spectra was developed based on the transfer matrix formalism, expressed by a matrix for our case:

$$\bar{\epsilon} = \begin{pmatrix} D_{xx} & -A_{xy} & 0 \\ A_{xy} & D_{xx} & 0 \\ 0 & 0 & D_{xx} \end{pmatrix} \quad (4.54)$$

where D_{xx} are the diagonal terms, obtained from parametric DF approximation, and A_{xy} are the anti-symmetric (off-diagonal) terms, which are parametrized based on the measured MOKE spectra. In this model, the film thickness, surface roughness as well as film and substrate optical constants were the input parameters. The off-diagonal tensor elements were described by a parametric model,

4.5. Magneto-optical Kerr effect

similar to the diagonal DF tensor approximation. The implemented approach was based on the one proposed by Mack *et al.* [152].

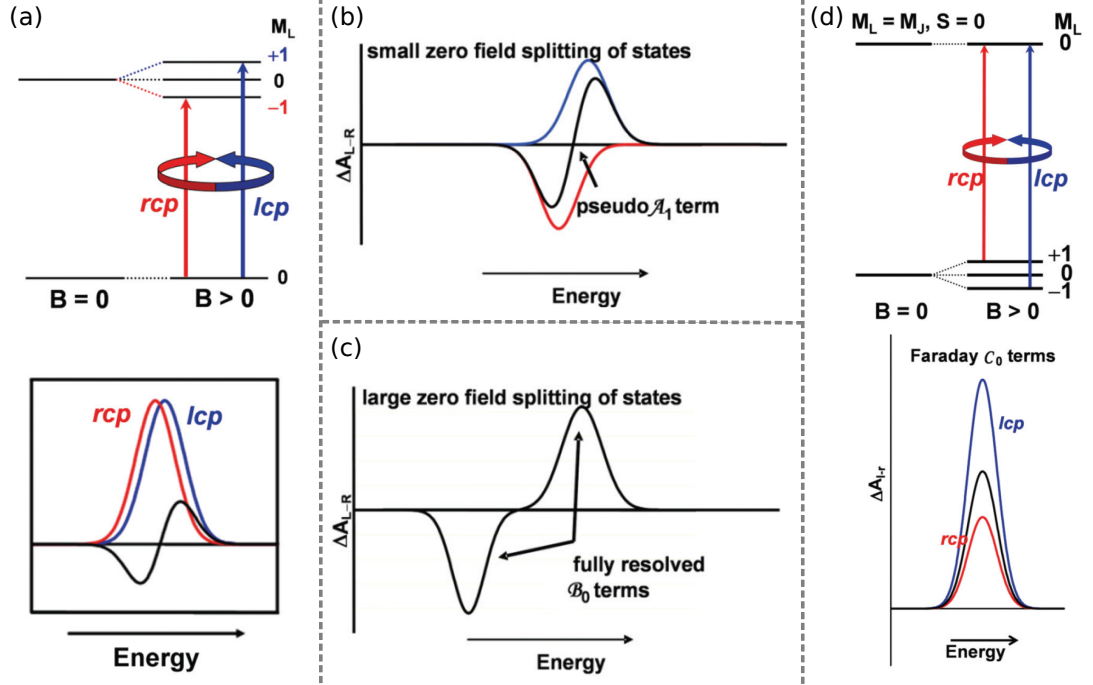


Figure 4.14: (a) Selection rules and derivative-shaped Faraday A_1 term (black line) due to Zeeman splitting of the band centers of the lcp (blue) and rcp (red) absorption bands. Depending on the strength of the zero field splitting, the coupled pair of lcp and rcp bands of opposite signs can (b) resemble a (pseudo-) A_1 term or (c) be fully resolved B_0 terms. (d) Absorption of the lcp (blue) and rcp (red) light between an orbitally degenerate ground state and a non-degenerate excited state. Image adopted from [171].

In the presence of external magnetic field, applied in the direction of light propagation, formation of M_{J+1} microstates occurs, where M_J denotes the total momentum quantum number. For $\Delta M_J = -1$, transitions are due to absorption of light in right circularly polarized (rcp) state, while $\Delta M_J = +1$ transitions are due to absorption of left circularly polarized (lcp) light. Therefore, the magnetically active optical behavior can be interpreted as a series of three Faraday terms, A_1 , B_0 and C_0 , which are related to the total approximation by [172]:

$$\Delta A_{1-r} = GB [A_1(-d\epsilon_{xy}(\omega)/d(\omega)) + (B_0 + C_0/kT)\epsilon_{xy}(\omega)] \quad (4.55)$$

where G is a constant, specific to the sample, which depends on the concentration and length of light propagation, and B is the strength of the magnetic field. The A_1 term is due to the $2g_J\mu_B B$ Zeeman splitting between the band centers of

4.5. Magneto-optical Kerr effect

the rcp and lcp absorption bands, in the orbitally degenerate excited state. The selection rule schematic for this term as well as a Gauss peak derivative shape is depicted in Figure 4.14 (a) [172]. The strength of the contribution of A_1 can be expressed as:

$$A_1 = d_A^{-1} \sum \langle J | \mu_Z | J \rangle - \langle A | \mu_Z | A \rangle ([m_{-1}^{AJ}]^2 [m_{+1}^{AJ}]^2) \quad (4.56)$$

where $\mu_Z = -\mu_B(L_Z + 2S_Z)$

where A and J correspond to the ground and excited state, while L_Z , S_Z and m represent orbital, spin angular momentum and electric dipole moment operators, respectively. The sign of the A_1 term depends on the total angular momentum difference between the ground and excited states.

The Faraday B_0 term pair is due to the field induced mixing of the zero field states by magnetic dipole transition moments and consists of Gauss peaks with opposite signs. Its contribution is given by:

$$B_0 = 2d_A^{-1} \Re \sum \frac{\langle J | \mu_Z | K \rangle}{\Delta E_{KJ}} - ([m_{-1}^{AJ}] [m_{+1}^{KA}] - [m_{+1}^{AJ}] [m_{-1}^{KA}]) \quad (4.57)$$

The energy separation between the K and J excited states (ΔE_{KJ}) determines the strength of the B_0 term contribution. When the zero field state splitting is weak in comparison to the spectral band width, a shape similar to the A_1 term is formed (pseudo- A_1), Figure 4.14 (b). Due to a large zero field splitting, the coupled B_0 pair is fully resolved and the net contribution of this term is zero, Figure 4.14 (c). While the A_1 and C_0 terms are observed in structures of high symmetry, the B_0 term is weaker and is found in low symmetry compounds.

The C_0 term is due to the Zeeman splitting of the orbitally degenerate ground state, Figure 4.14 (c), and can be expressed as:

$$C_0 = -d_A^{-1} \sum \langle A | \mu_Z | A \rangle ([m_{-1}^{AJ}]^2 [m_{+1}^{AJ}]^2) \quad (4.58)$$

This term is strongly dependent on temperature ($\sim 1/kT$), due to the population of the ground state, which can be described according to a Boltzmann distribution. While at low temperatures the shape of C_0 resembles a Gaussian function, at room temperature it exhibits a Gauss derivative shape [171].

Experimentally obtained MOKE spectra are exemplary shown for ZFOT1 sample in Figure 4.15 (a). The fit of the parametric approximation to the spectra in terms of ellipsometric parameters is depicted in Figure 4.15 (b). The approxi-

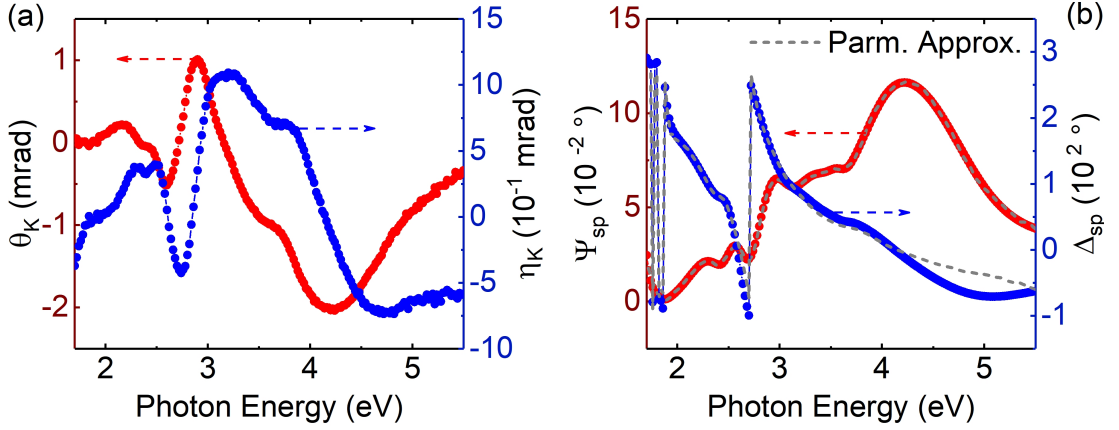


Figure 4.15: (a) Experimentally determined θ_K and η_K , shown exemplary for sample ZFOT1. (b) MOKE spectra values, represented in terms of ellipsometric parameters, Ψ_{sp} and Δ_{sp} , with the parametric approximation fit to the experimental data.

mation of the imaginary component of the off-diagonal dielectric tensor element, $\epsilon_{2,xy}$, consists of a series of Gaussian functions with positive and negative amplitudes, shown in Figure 5.9. The off-diagonal tensor exhibits an overlap of a number of transitions, characteristic of the models described above. To distinguish between transition is not at all trivial, as magnetically active transitions are distributed over the measured spectral range. This would require a much more elaborate model, consisting of at least two Gauss functions per transition to account for rcp and lcp contributions, which would result in an immense number of free parameters. However, some information can still be obtained when comparing the $\epsilon_{1,xy}$ line-shapes of the same material, e.g. in dependence on growth conditions. The strength of magneto-optical features are likely to vary while the change in transition energy should remain nearly constant, signifying a change in the magnetic cation interactions. This yields a deeper understanding behind the nature of electronic transitions, visible in the diagonal tensor elements for the same material, described in Section 5.2.

4.6. Magneto-static properties

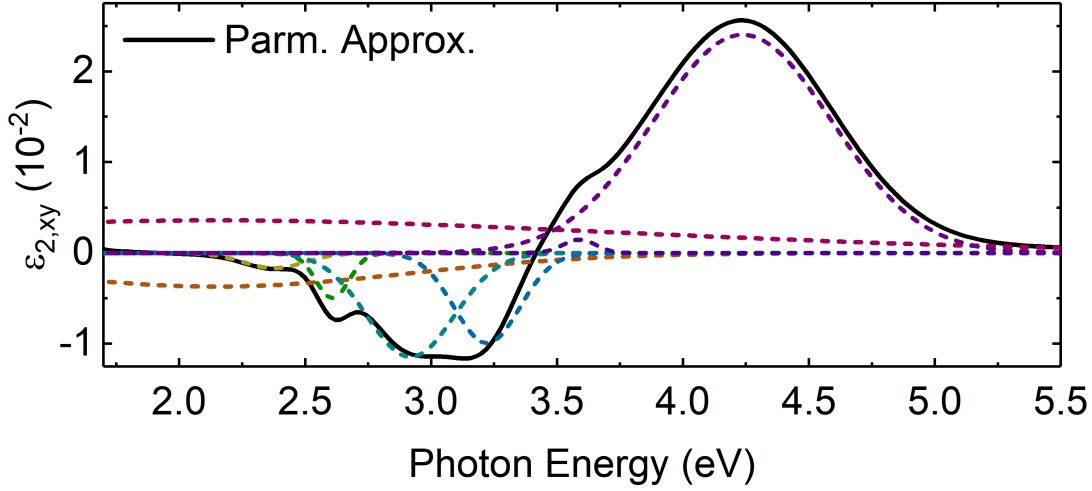


Figure 4.16: Parametric approximation of the imaginary component of the off-diagonal dielectric tensor element, $\epsilon_{2,xy}$. Individual contributions to the DF line-shape are shown as short-dashed lines.

4.6 Magneto-static properties

The principal objective of this investigation is to examine the main interactions, responsible for the observed magnetic behavior. For this purpose, magnetization measurements were conducted as a function of applied field and temperature, described below.

Vibrating sample magnetometry

Magnetic properties of LP ZFO, HP ZFO and annealed films were obtained by a physical property measurement system (PPMS-Quantum Design, USA) operating in vibrating sample magnetometer (VSM) mode. The schematic representation of the operational principle of the VSM, similar to the one used in this investigation, is depicted in Figure 4.17(a). Its operation is based on the Faraday's law, namely due to the electromagnetic force in a coil, generated by a change in flux through the coil [173]. The sample, mounted on a fused quartz sample rod, is located in a highly homogeneous, external magnetic field and exhibits vertical oscillation movement of 40 Hz in 2 mm range. The stationary gradiometer pick-up coils are located on the poles of the electromagnet with their symmetry center coinciding with the magnet center of the static sample. The change in magnetic flux, in response to the applied magnetic field (B), is detected by the change in oscillation frequency, which induces a voltage U_{ind} in the coils. For n_c

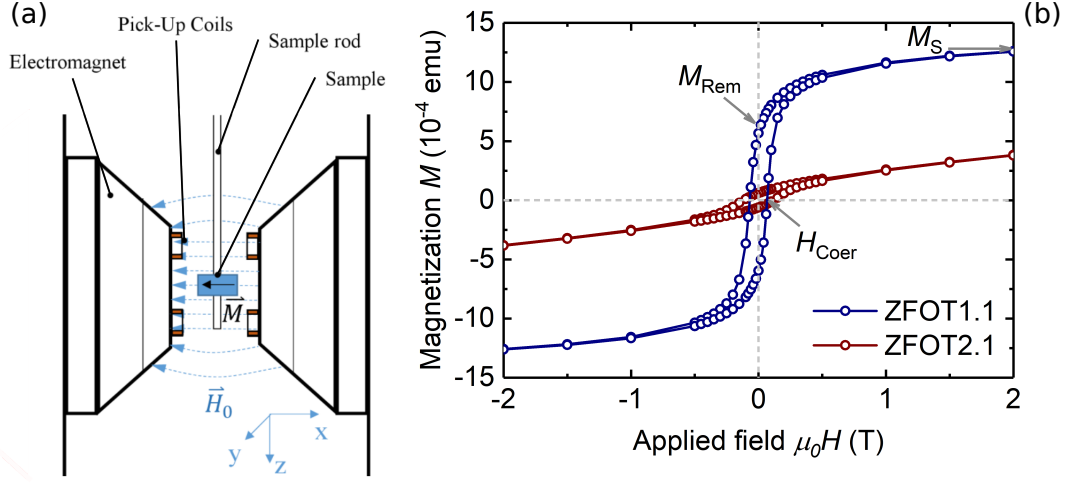


Figure 4.17: (a) Schematic representation of the operational principle of the VSM technique. Adopted from [173]. (b) Magnetization as a function of applied field $\mu_0 H$ for ZnFe₂O₄ films grown at low (ZFOT1.1) and high (ZFOT2.1) oxygen pressure and temperature, measured at 5 K. Magnetization saturation (M_S), remanence (M_{Rem}) and coercivity field (H_{Coer}) for ZFOT1.1 indicated.

pick-up coils with a flat surface A and n_w windings, the induced voltage is given as [174]:

$$U_{ind} = \sum_{n_c} \sum_{n_w} \int_A \frac{\delta B}{\delta t} dA \quad (4.59)$$

When the homogeneous magnetic field is applied along the x-axis, Figure 4.17 (a), the sample exhibits a sinusoidal movement $\delta(t)$ along the z-axis with an amplitude \hat{z} and frequency ω :

$$\delta(t) = \frac{dz}{dt} = \hat{z} \cdot \omega \cos(\omega t) \quad (4.60)$$

A change in the flux density \vec{B} , for a point at a distance \vec{r} from the sample, is given by:

$$\delta \vec{B} = \mu_0 \cdot \delta(t) \cdot \nabla \vec{H}(\vec{r}) \quad (4.61)$$

where $\nabla \vec{H}(\vec{r}) = -\frac{3m}{4\pi r^7} \cdot G$, with G being the parameter, which is related to the position and orientation of the pick-up coils. Therefore, the induced voltage can be expressed as:

$$U_{ind} = -\frac{3\hat{z}m}{4\pi} \cdot \mu_0 \cdot \cos(\omega t) \cdot \sum_{n_c} \sum_{n_w} \int_A d\vec{A} \cdot \frac{1}{d^7} \cdot G \quad (4.62)$$

4.6. Magneto-static properties

The change in magnetic flux as a function of time is due to the vertical movement of the sample, relative to the coils, leading to the detection of the sample magnetic moment m [175, 176].

The system is able to resolve magnetization changes of less than 10^{-6} emu at a data rate of 1 Hz. The VSM detection module uses the position encoder signal, obtained from the motor module, as a reference for the synchronous detection. It detects the in-phase and quadrature-phase signals from the encoder and from the amplified voltage of the pick-up coil. The signals are then averaged resulting in the detected signal. The maximum applied magnetic field of 9 T is possible in this system with a superconducting coils. The system is cooled regularly with He and N₂ cryogenic liquids [177].

SQUID-magnetometry

The bulk magnetic properties of our thin films with variable Zn content were recorded using a superconducting quantum interference device (SQUID) (MPMS-7 Quantum Design, USA). The operation principle of this device is similar to the one described above. It uses a second order gradiometer superconducting detection coils, also cooled with He cryogenic liquid. The maximum applied magnetic field is 7 T with a sensitivity of 10^{-8} emu. The measurements were conducted by A. Setzer, I. Lorite and Y. Kumar under the supervision of P. Ezquinazi within the division of Superconductivity and Magnetism at the Felix Bloch Institute for Solid State Physics, Universität Leipzig.

Measurement and data treatment procedure

Figure 4.17 (b) shows magnetization as a function of applied field, exemplary for two films of low (ZFOT1.1) and high (ZFOT2.1) growth temperature and oxygen pressure. The displayed measurements were conducted at 5 K. The film grown at low temperature and pressure displays ferromagnetic-type hysteresis with a magnetization saturation (M_S) as well as coercivity field (H_{Coer}). The film grown at high temperature and pressure, on the other hand, displays a lack of magnetic saturation, due to a strong paramagnetic contribution, as well as a low magnetization remanence. The external field was applied in the sample surface plane for all measurements in this study. The magnetization of the substrates was measured at the same conditions as the samples. The diamagnetic contributions from the substrate and the sample holder were redacted by linear

4.6. Magneto-static properties

fitting at high fields and subtracting the contribution from sample magnetization measurements. Important to note, all substrates had a diamagnetic contribution at room temperature, with a negative $M - H$ slope. Substrates prior to pre-deposition treatment (chemical etching and annealing) exhibited a magnetic response, which was attributed to presence of impurities, likely found at the surface [178,179]. Furthermore, the MgO substrate exhibited a ferromagnetic behavior at 5 K, this has recently been investigated and also related to contribution of point defects and impurities [180,181].

In order to investigate the temperature dependence of the magnetic interactions, magnetization as a function of temperature was recorded with the following procedure. Initially, the sample was cooled down to 5 K with no applied field. Then a magnetic field of either $\mu_0 H = 0.01, 0.1$ or 1 T was applied, and the magnetization was measured during heating to room temperature or 350 K (ZFC) and thereafter cooling back down to 5 K (FC). Consequently, the field was set to $\mu_0 H = 0$ T and the sample remnant magnetization as a function of temperature was recorded upon heating to room temperature or 350 K. Furthermore, the measured magnetization data (in emu) was normalized either to the thin film mass, volume, or per formula unit in terms of Bohr magneton μ_B [49]:

$$M[\mu_B/f.u.] = \frac{1}{8} \left(\frac{V_{Film}}{a^3} \right)^{-1} \frac{M[emu]}{9.274 \cdot 10^{-21} emu/\mu_B} \quad (4.63)$$

where a is the lattice constant, V_{Film} is thin film volume and $\mu_B = \frac{e\hbar}{2m_e}$ with e , \hbar and m_e is the electron charge, reduced Plank's constant and mass of the electron, respectively.

Chapter 5

Results and discussion

In this chapter, all significant results are presented and discussed. First, the magnetic and optical properties of Fe_3O_4 PLD-grown thin films are compared to that of a single crystal. Clear difference in the magnetic response as a function of both applied field and temperature was found for the thin films as compared to the single crystal. The Fe_3O_4 dielectric function is compared to the $\gamma\text{-Fe}_2\text{O}_3$ film spectra, with respect to expected cation configuration.

Magnetically active electronic transitions of the $\text{Zn}_x\text{Fe}_{3-x}\text{O}_4$ system are examined in detail. The difference in the spectral features is attributed to the presence of cationic disorder in dependence on substrate temperature and oxygen partial pressure during fabrication. The magneto-optical response as a function of applied field shows active transitions, involving cations of two distinct types.

In order to deeper understand the influence of the substrate temperature during fabrication with respect to the crystal structure, ZnFe_2O_4 thin films were deposited at different temperatures, but the same oxygen partial pressure. The behavior of dielectric function features was characteristic of an increase in the crystal quality with the increase in deposition temperature. The strength of the electronic transition, involving Fe_{Td}^{3+} cations, showed a direct correlation to the ferrimagnetic response.

Next, the effect of thermal treatment was exploited in order to manipulate the magnetic behavior. ZnFe_2O_4 thin films, deposited at low and high oxygen partial pressure were annealed at various temperatures in oxygen and argon environments, respectively. The thin films exhibited a cation renormalization from a disordered spinel toward a more stable normal spinel structure when annealed at temperatures above the deposition temperature, regardless of the environment. The corresponding change in the dielectric function features was directly correlated to the diminishing magnetic response.

5.1. Magnetic and optical properties of Fe₃O₄ thin film and SC

Lastly, the cation configuration distribution within the bulk and surface regions was examined in dependence on the Zn concentration of Zn_xFe_{3-x}O₄ thin films. The predominant cation configuration was determined to be of inverse and normal spinel with $x \leq 0.56$ and $x \geq 0.87$, respectively. A nearly homogeneous cation configuration distribution was determined for the $x = 0.87$ film, consistent with a smooth surface morphology and Bloch law temperature dependence of saturation magnetization. A deficiency (abundance) of Fe³⁺ on the octahedral (tetrahedral) sublattice is found in the bulk, as opposed to the near-surface region, of the film with predominantly inverse cation configuration. As a result, the non-uniform distribution leads to a diminished magnetic response in films of inverse spinel configuration, whereas the presence of Fe_{Td}³⁺ cations in the surface region of the normal spinel film $x = 1.26$ is likely responsible for the observed magnetic behavior.

5.1 Magnetic and optical properties of Fe₃O₄ thin film and single crystal

In this section, magnetization of the PLD-grown Fe₃O₄ thin films as a function of applied field and temperature is compared to that of a single crystal sample (Fe₃O₄ SC), obtained from Matrin-Luther University of Halle-Wittenberg. The Fe₃O₄ thin film dielectric function line-shape is compared to that of the single crystal as well as that of γ -Fe₂O₃, which is a Fe_{Oh}²⁺ cation poor structure. The temperature dependence of the thin film dielectric function is examined with respect to the visible electronic transitions.

In order to investigate the physical properties of PLD-grown Fe₃O₄ thin films, their dielectric function and magnetic response were compared to that of a single crystal Fe₃O₄ sample (Fe₃O₄ SC). The sample was obtained from Stefan Ebbinghaus at the Matrin-Luther University of Halle-Wittenberg and prepared by a crystal growth unit using Czochralski process, Malvern MSR2, similar procedure as described in [182]. The wide angle 2θ XRD scans reveal a single phase structure with (004) and (008) reflexes evident, Figure 5.1 (a). The four-fold symmetry of the (113) ω peak, Figure 5.1 (b), along with a full width half maxima of 0.103° of the (004) ω peak indicates exceptional crystalline quality. The PLD-grown films, ZnX0 (60 nm) and FFO (110 nm), were deposited on TiN/MgO and MgAl₂O₄ substrate, respectively. The parameters, specific to the film fabrication, are listed in Table 3.1 of Chapter 3. The γ -Fe₂O₃ maghemite film (100 nm) was grown in similar conditions as the FFO film on an MgO substrate.

5.1. Magnetic and optical properties of Fe_3O_4 thin film and SC

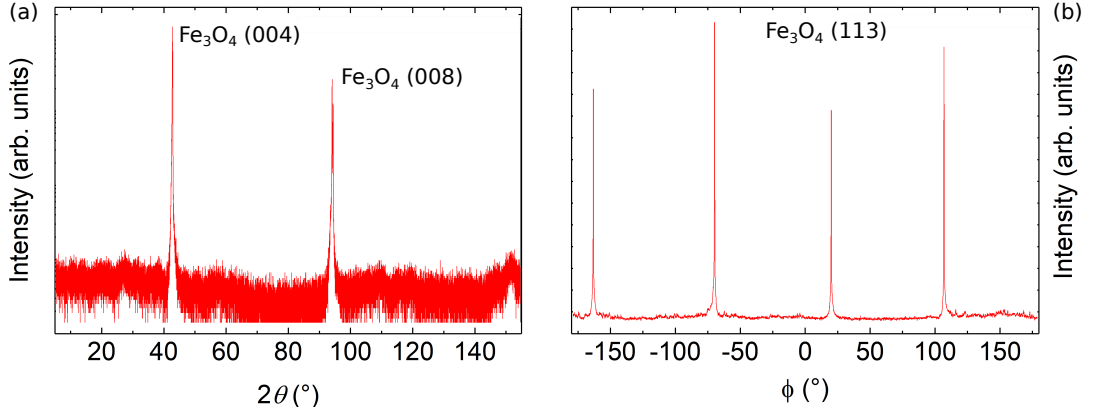


Figure 5.1: (a) Wide angle 2θ scan with Fe_3O_4 (004) and (008) reflexes indicated. (b) ϕ scans reveal a four-fold symmetry of the Fe_3O_4 (113) ω peak.

Figure 5.2 (a) shows magnetization as a function of applied field, measured at 5 and 300 K. The sample exhibits a more abrupt change in magnetization in low applied field at low temperature, as compared to room temperature measurement. At both temperatures, a lack of coercivity field indicates a single magnetic domain structure, since a negligible amount of energy is dissipated in the reversal of magnetization. The room temperature hysteresis loop becomes wider for the ZnX0 sample ($H_{Coer} = 17.5 \text{ mT}$) and shows a hard magnetic characteristic, with a large coercivity field of ($H_{Coer} = 29.7 \text{ mT}$) for the FFO sample, Figure 5.2 (b).

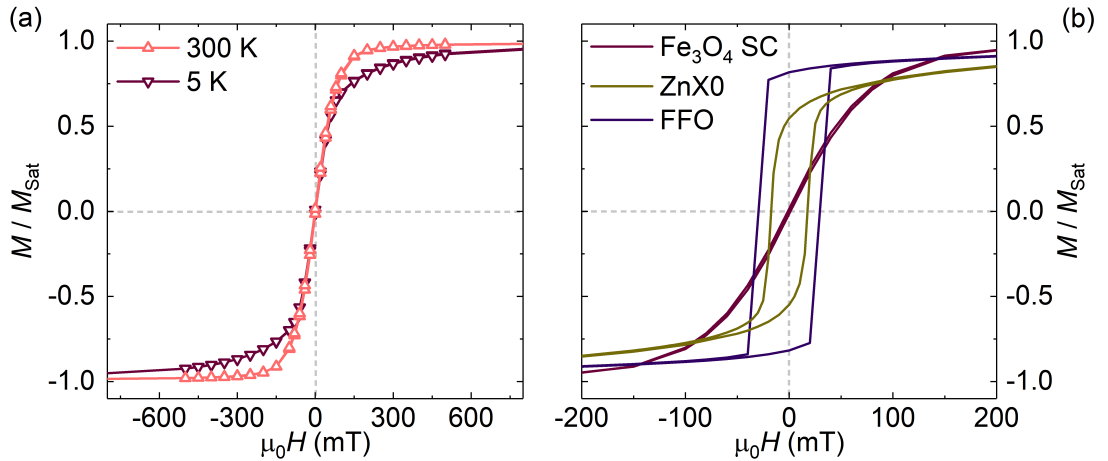


Figure 5.2: (a) Magnetization as a function of temperature for the Fe_3O_4 SC sample, measured at 5 and 300 K. (b) Hysteresis curves for magnetite samples measured at 300 K and normalized to the magnetization saturation.

Magnetization as a function of temperature, measured in the ZFC-FC mode, is shown in Figure 5.3 (a-c). The magnetization of the SC sample, exhibits a

5.1. Magnetic and optical properties of Fe_3O_4 thin film and SC

slight increase in magnetization with decrease in temperature and then an abrupt decrease below the Verwey transition temperature ($T_V = 116.7 \text{ K}$) in both ZFC and FC. Below T_V , magnetization is nearly constant. The abrupt change in magnetization clearly indicates a transition in the intrinsic magnetic interactions, while a constant magnetic response could suggest that no change in the magnetic interaction takes place below T_V . For the PLD-grown Fe_3O_4 thin films, the change in magnetization is also apparent below T_V , however it is diminished. This is likely due to the presence of additional magnetic interactions, which are dependent on temperature and lead to a decrease in magnetization below T_V of the ZFC curve. While the T_V temperature of ZnX0 sample coincides with the SC, it is slightly larger than for the FFO sample ($T_V = 120.1 \text{ K}$). Furthermore, with increase in temperature above T_V , the magnetization of the FFO sample exhibits a monotonous decrease, while that of ZnX0 sample remains nearly constant.

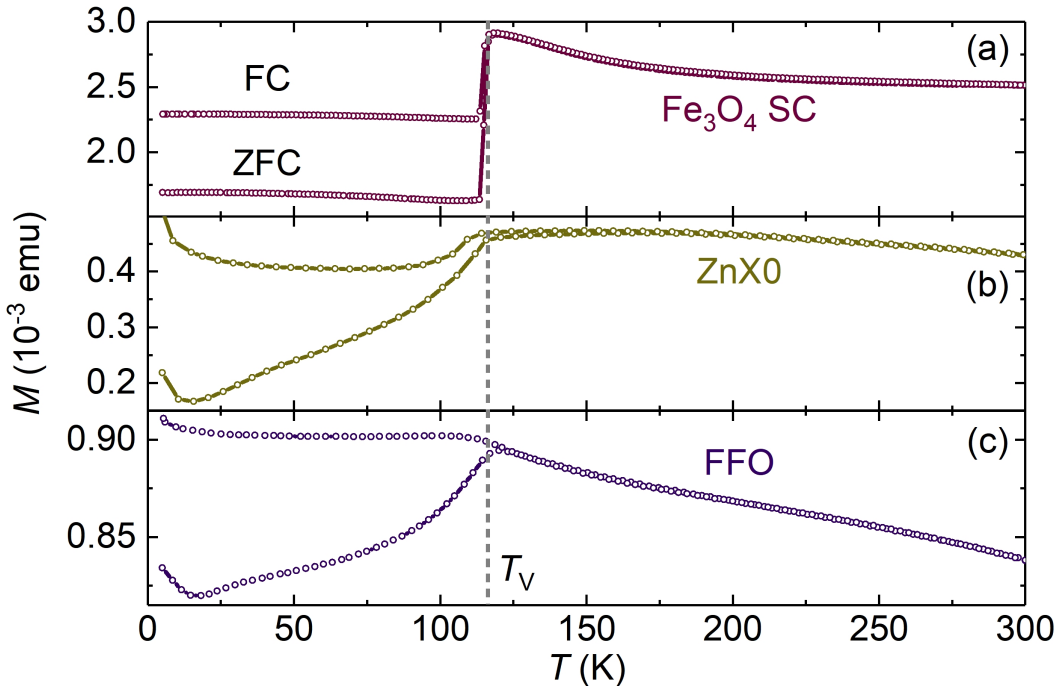


Figure 5.3: Magnetization as a function of temperature, measured in the ZFC and FC mode, for the (a) Fe_3O_4 SC, (b) ZnX0 and (c) FFO samples while applying a field of 0.1 T. ZFC and FC curves exhibit high and low magnetization, respectively, below the indicated Verwey transition temperature (T_V).

The parametric approximation of the dielectric function for the ZnX0 sample is presented in Figure 5.4 (a) with individual approximation functions indicated. The same model was used to describe the dielectric function line-shape of Fe_3O_4 SC and FFO thin film. The line-shape of ZnX0 matches the one of Fe_3O_4 SC very closely, and also agrees well to the one presented in literature upto the visible

5.1. Magnetic and optical properties of Fe_3O_4 thin film and SC

spectral range [183,184]. It consists of a series of Gaussian functions, positioned at energies of corresponding electronic transitions, listed in Section 4.4. For comparison, the dielectric function line-shape approximation for a PLD-grown $\gamma\text{-Fe}_2\text{O}_3$ thin film is presented in Figure 5.4 (b). The main difference between the two materials is the presence of Fe_{Oh}^{2+} in magnetite, as indicated in the ion distribution formula in Figure 5.4. A clear difference in the line-shape shows that the dielectric function of $\gamma\text{-Fe}_2\text{O}_3$ can be approximated without the functions that involve the Fe_{Oh}^{2+} cation transitions. The difference in the strength of the features arises from the different cation content on each site, namely $(\text{Fe}^{3+})_{Td}(\text{Fe}_{5/3}^{3+} V_{1/3})_{Oh}$ for maghemite, where V corresponds to Fe^{3+} cation vacancy, and $(\text{Fe}^{3+})_{Td}(\text{Fe}^{2+}\text{Fe}^{3+})_{Oh}$ for magnetite. However, the energies of the approximation functions deviate only by a maximum of 50 meV from those listed in Table 4.2 of Section 4.4.

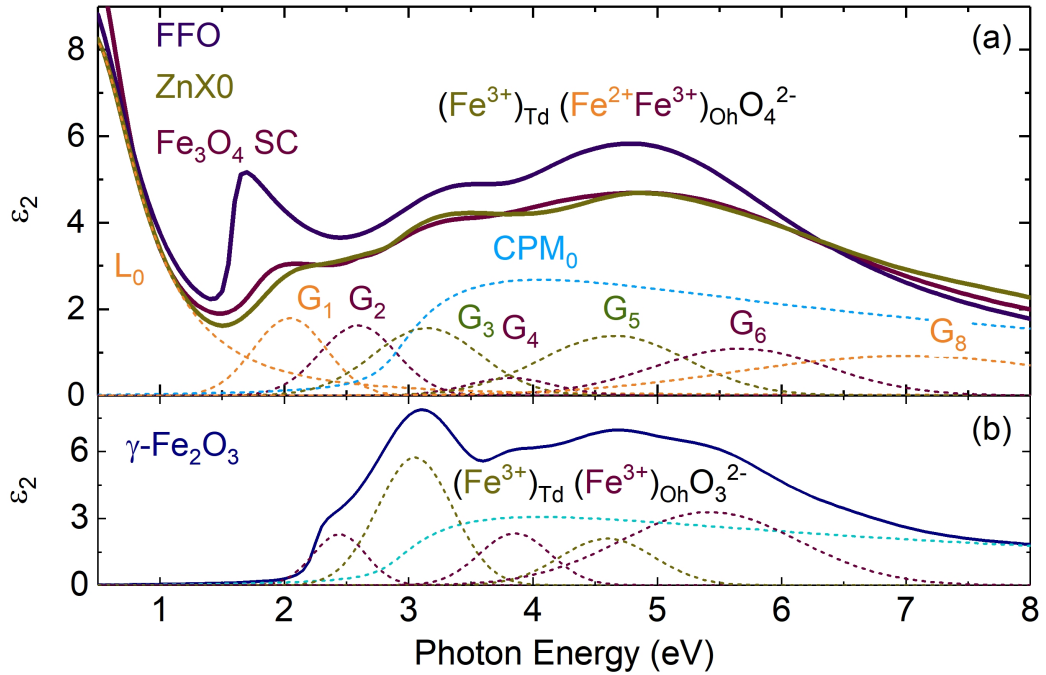


Figure 5.4: (a) Parametric approximation of the dielectric function line-shape for the three magnetite samples. The approximation functions to the ZnX0 DF line-shape are indicated, and color-coded for transitions involving Fe_{Oh}^{2+} (orange), Fe_{Td}^{3+} (green) and Fe_{Oh}^{3+} (green). (b) A DF line-shape of the $\gamma\text{-Fe}_2\text{O}_3$ thin film is approximated with a series of similar functions and is shown for comparison. Apparently, no Fe_{Oh}^{2+} is present. The ion distribution formula is indicated for each material.

5.1. Magnetic and optical properties of Fe₃O₄ thin film and SC

In contrast to the Fe₃O₄ SC and ZnXO, the parametric dielectric function approximation of FFO has a pronounced feature at 1.68 eV. It is described by a Lorentzian function and is assigned to an electronic transition between t_{2g} and e_g bands of Fe²⁺ and Fe³⁺ cations on octahedral lattice sites, respectively. The dielectric function line-shape as a function of temperature for this film shows two clear changes, namely in the features located at ~ 0.8 eV and those >3.1 eV. The former feature corresponds to an electronic transition between the d orbitals of the Fe_{Oh}²⁺ cation. The strength of this transition increases with the decrease in temperature and remains nearly constant at temperatures below 150 K. The latter feature corresponds to a combination of transitions involving cation 4s bands, which decrease in strength with a decrease in temperature. Similarly to the low energy transition, the rate of change of this feature decreases below assumed Verwey transition temperature. This behavior is coincident with the energy-weighted sum rule, where the spectral weight decreases in energy with the decrease in temperature. Below T_V , the change in the dielectric function line-shape is less pronounced, specifically the change in the transition directly involving Fe_{Oh}²⁺ d orbitals.

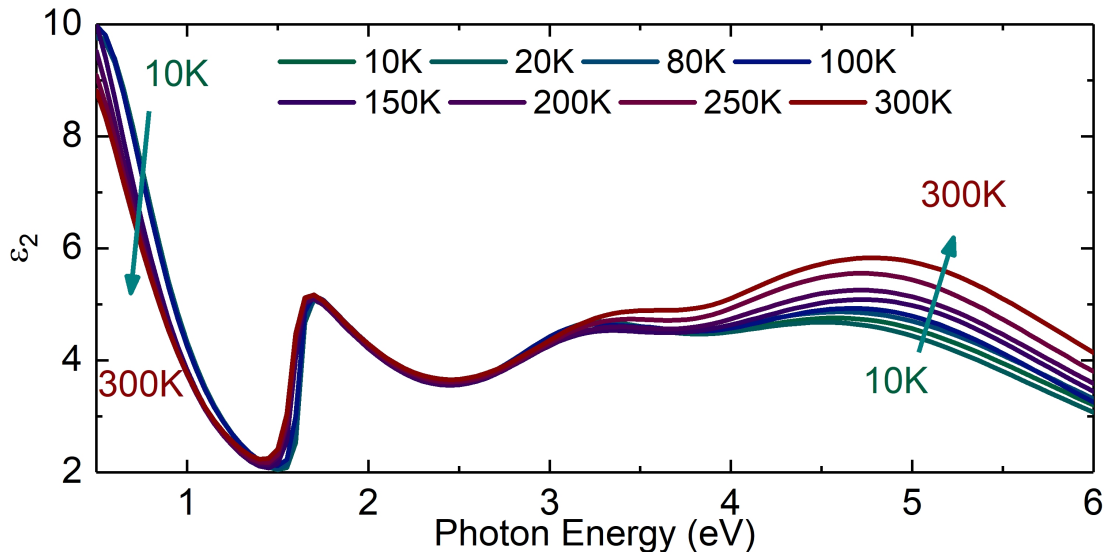


Figure 5.5: Parametric approximation of the DF for the FFO film, measured in the temperature range from 10 - 300 K.

5.1. Magnetic and optical properties of Fe₃O₄ thin film and SC

Summary:

In this section, we examined the magnetic and optical properties of Fe₃O₄ thin films. The Fe₃O₄ PLD-grown films exhibited a magnetic hysteresis with notable coercive field and a nearly monotonous magnetization increase with the increase in temperature below the Verwey transition temperature, as compared to the single crystal. The line-shape of the dielectric function of γ -Fe₂O₃ can be approximated by the model for Fe₃O₄, but without the contribution of Fe²⁺ cations, consistent with the expected cation distribution. A good agreement of the dielectric function line-shape between the SC and ZnX0 film is evident. The Verwey transition can be observed in the temperature dependence of the diagonal dielectric tensor element, namely below T_V the rate of change in low and high energy features is lower than above T_V .

5.2 Magneto-optical properties of $\text{Zn}_x\text{Fe}_{3-x}\text{O}_4$ thin films

The dependence of the predominant features in the optical spectrum on the magnetic field is achieved by examining the magneto-optical properties of the PLD-grown $\text{Zn}_x\text{Fe}_{3-x}\text{O}_4$ thin films. In this section, the diagonal and the off-diagonal dielectric function tensor elements are compared and the magnetic field dependence of the electronic transitions is presented and discussed [185].

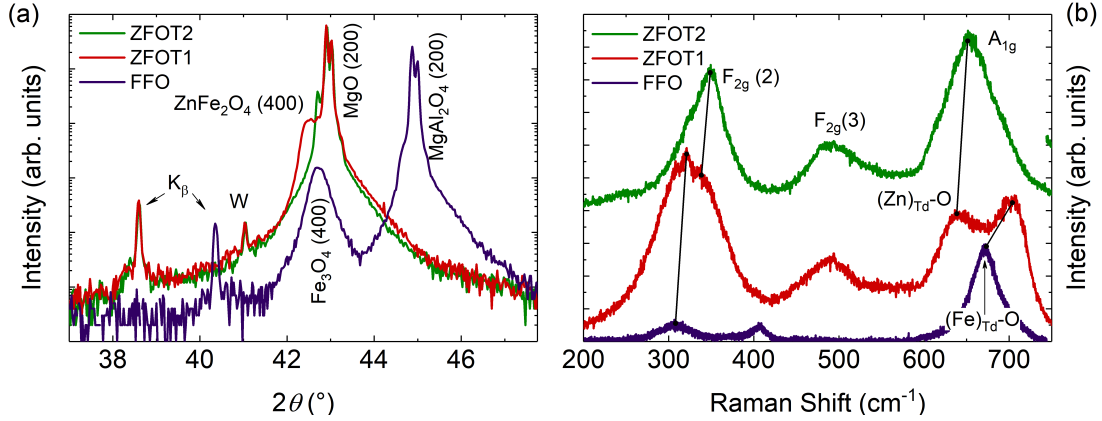


Figure 5.6: (a) XRD 2θ scans for ZFOT2, ZFOT1 and FFO samples. Substrate reflexes marked by K_β and W correspond to Cu K_β and W L_α spectral lines of the X-ray tube, respectively. (b) Raman spectra of the three films with phonon modes and cations involved as indicated.

For this purpose, ZnFe_2O_4 thin films were deposited at low (ZFOT1) and high (ZFOT2) temperature and oxygen partial pressure on an MgO substrate. The XRD spectra for both ZnFe_2O_4 films suggests a film of a single phase, ZnFe_2O_4 (400) reflex in Figure 5.6 (a). With increase in substrate temperature and partial pressure, a decrease in the lattice parameter from 8.53 to 8.46 Å for the ZFOT1 and ZFOT2 films is evident by the shift in the ZnFe_2O_4 XRD peak. The latter value is close to the bulk (8.44 Å) and is likely due to fewer defects present in the system. The FFO film, grown on a (100) MgAl_2O_4 substrate, also consists of a single phase Fe_3O_4 film, evident by the (400) reflex. The determined lattice parameter of 8.47 Å is higher than that expected for the bulk of 8.40 Å.

The Raman spectrum of the FFO film shows one clear phonon mode, located at 671 cm^{-2} , Figure 5.6 (b). This mode corresponds to the A_{1g} mode and likely involves the $\text{Fe}_{T_d}^{3+}$ cations [128]. From a Lorentzian fit, its width was determined to be 42.3 cm^{-2} . The two less pronounced features in the FFO spectrum correspond to the F_{2g} modes and are located at 308 and 406 cm^{-2} . The Raman spectrum

5.2. Magneto-optical properties of $\text{Zn}_x\text{Fe}_{3-x}\text{O}_4$ thin films

for ZFOT2 film contains three features that are located at 350, 490, as well as 650 cm^{-2} and correspond to two F_{2g} modes as well as an A_{1g} mode of ZnFe_2O_4 film, respectively. Interestingly, a combination of the low energy F_{2g} mode and the A_{1g} mode, which are present in the FFO and ZFOT2 film spectra, are observed in the ZFOT1 film spectrum. Spectrally resolved are the two contributions to the A_{1g} mode, which could suggest a possible tetrahedral coordination of two cations, namely Zn^{2+} and Fe^{3+} in the ZFOT1 film. The latter of which could be indicative of structural disorder in the normal spinel ZnFe_2O_4 thin film.

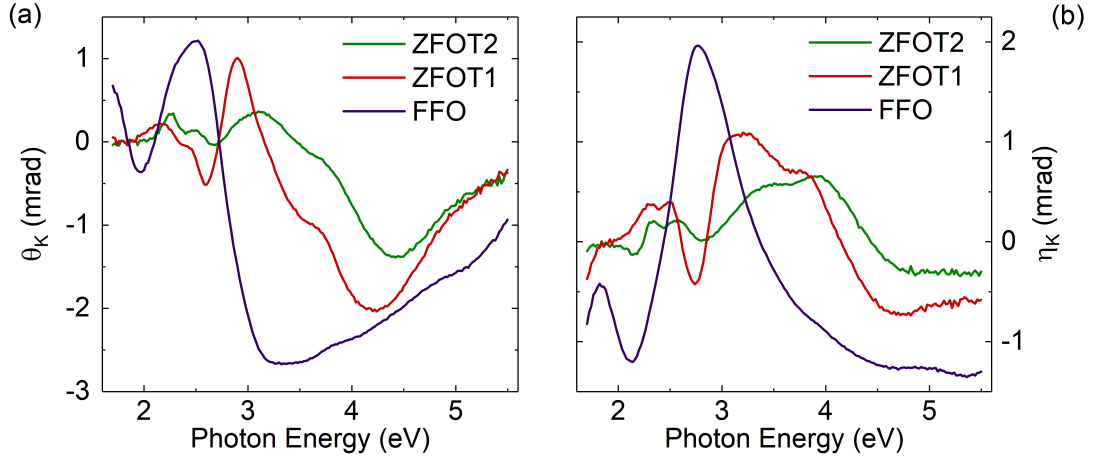


Figure 5.7: (a) Real θ_K and (b) imaginary component η_K of the measured MOKE spectra Φ_K at an applied magnetic field of 1.7 T for ZFOT2, ZFOT1 and FFO films.

The measured real (θ_K) and imaginary (η_K) components of the complex Φ_K MOKE spectra are presented in Figure 5.7 (a) and (b). The measured signal is highest for the FFO and lowest for the ZFOT2 thin film. The oscillations, visible below 2.5 eV in ZFOT2 and ZFOT1 spectra, are due to film thickness interference and are accounted for during the modeling procedure. The off-diagonal tensor elements were derived and described by the procedure presented in Section 4.5. Since this approach involves the diagonal dielectric tensor element approximation, similarities in transition assignment are anticipated.

The differences in the imaginary component of the diagonal dielectric tensor element ($\epsilon_{2,xx}$) between the ZFOT2 and ZFOT1 samples can be seen in Figure 5.8 (a). First and foremost, the low energy feature is apparent only for the ZFOT1 sample. As the transition at $\sim 1\text{ eV}$ involves Fe_{Oh}^{2+} cations, this feature corresponds well to the films deposited in a oxygen-poor environment. Additionally, the ZFOT1 film demonstrates weaker high energy feature $\sim 5.6\text{ eV}$, which exhibits a redshift as compared to the ZFOT2 spectra. This can be related to a decrease

5.2. Magneto-optical properties of $\text{Zn}_x\text{Fe}_{3-x}\text{O}_4$ thin films

in the Fe^{3+} cations of octahedral coordination with a decrease in deposition temperature. Furthermore, a rise in the amplitude of the feature, located at ~ 3.5 eV, is apparent for the ZFOT1 film as compared to the ZFOT2 film. This behavior is coincident with the real component of the off-diagonal dielectric tensor element, Figure 5.8 (b).

Since the off-diagonal dielectric tensor elements are sensitive to the applied magnetic field, the increase in strength of this feature is likely due to a higher concentration of magnetically active cations. As the magnetic moments of octahedrally coordinated Fe^{3+} cations is antiferromagnetically aligned and expected to be compensated in a normal spinel ferrite, the cation which is likely to exhibit a magnetic response in disordered spinel, grown at low temperature, is the Fe_{Td}^{3+} . Coincidentally, the change in amplitude of this feature is apparent in both the diagonal and off-diagonal dielectric tensor elements and therefore this feature can be assigned to a transition involving Fe_{Td}^{3+} cation orbitals. Another feature to increase in strength with the decrease in deposition temperature and pressure is located at ~ 4.7 eV. Since it is distinguished in the magneto-optical response, it can be considered to also correspond to cation disorder, likely caused by tetrahedral coordination of Fe^{3+} cations.

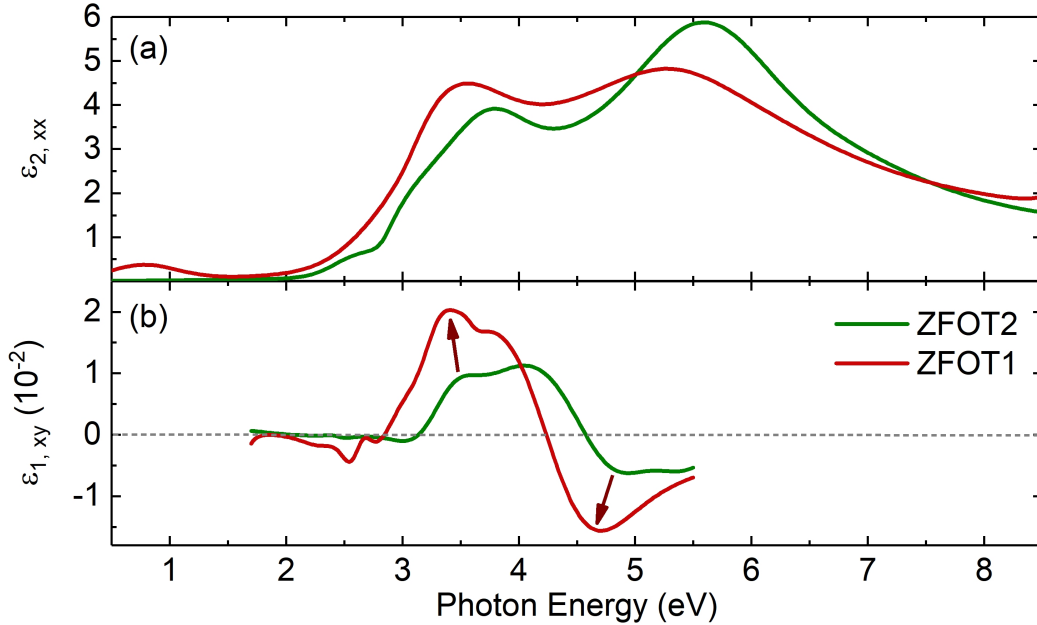


Figure 5.8: (a) Imaginary component of the diagonal dielectric tensor element ($\epsilon_{2,xx}$), approximated by the parametric approach. (b) Parametric approximation of the real component of the off-diagonal dielectric tensor element ($\epsilon_{1,xy}$). Horizontal dashed line indicates the zero for clarity. The arrows indicate an increase in feature amplitude with the decrease in deposition temperature and pressure.

5.2. Magneto-optical properties of $\text{Zn}_x\text{Fe}_{3-x}\text{O}_4$ thin films

The line-shape of the diagonal dielectric tensor element contains features consisting of overlapping transitions that involve bands of both Zn and Fe cations. The response in the off-diagonal dielectric tensor element is due to electronic transitions which are sensitive to the applied magnetic field. Both diagonal and off-diagonal dielectric tensor elements for magnetite are depicted in Figure 5.9 (a).

The real component of the measured MOKE spectra was recorded in dependence on applied magnetic field, Figure 5.9 (b) and (c). Similarly to the work presented by Zelis *et al.* [41], who examined the XMCD intensity as a function of applied field, we observe the MOKE response at 2.5 eV and 3.3 eV with the same and opposite sign with respect to the applied magnetic field, respectively. This confirms that the transitions of the corresponding energy of 2.5 eV and 3.3 eV involve cations whose magnetic moment is aligned antiferromagnetically. Such magneto-optical behavior further validates that the magnetic moment of octahedrally coordinated Fe cations would align along the applied magnetic field, while that of tetrahedral Fe cations would align against the direction of the applied magnetic field.

5.2. Magneto-optical properties of $\text{Zn}_x\text{Fe}_{3-x}\text{O}_4$ thin films

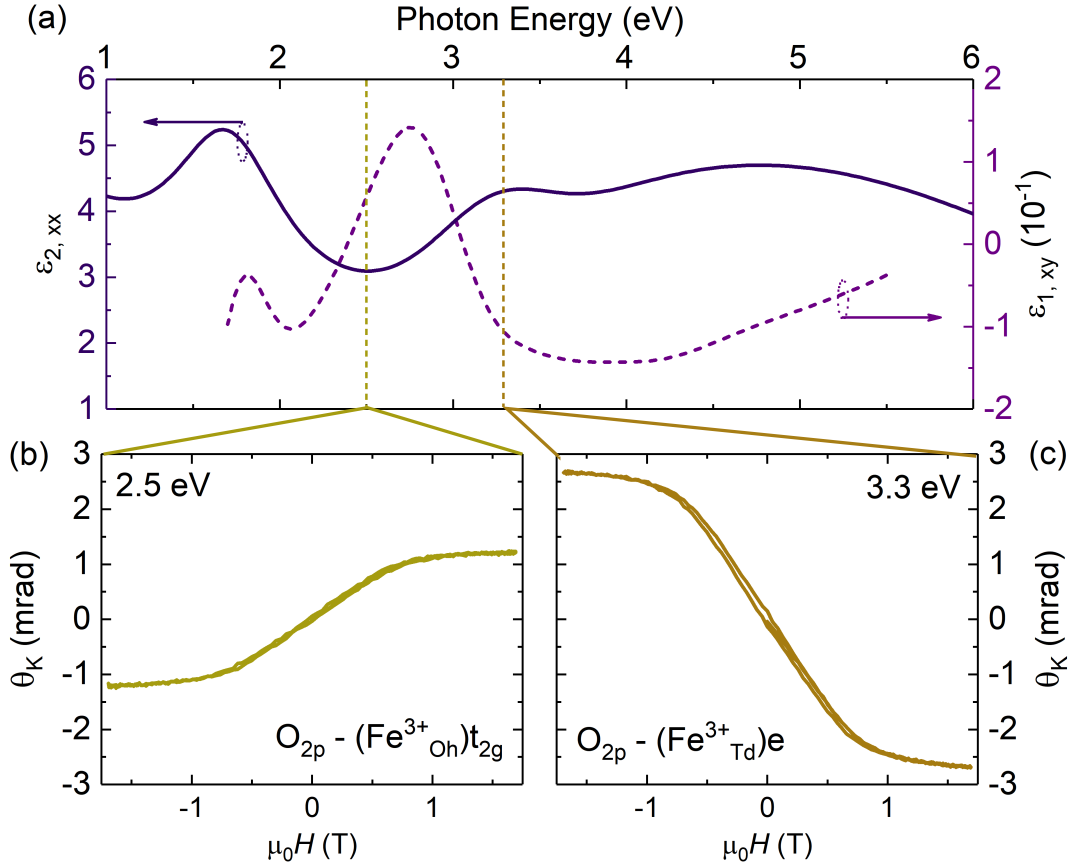


Figure 5.9: (a) Imaginary and real component of the diagonal and off-diagonal dielectric tensor element, respectively, for the FFO thin film. The real component θ_K of the measured MOKE spectra Φ_K as a function of applied magnetic field while being illuminated with light of (b) 2.5 eV and (c) 3.3 eV.

Summary:

In this section, the off-diagonal element of the dielectric tensor for a disordered film is examined in comparison to that of a normal spinel. The presence of disorder is evident by the increase in amplitude of a transition involving tetrahedrally coordinated Fe^{3+} . Therefore, the MOKE signal in the vicinity of this transition in the Fe_3O_4 film exhibits the opposite sign as the applied magnetic field, indicating an antiparallel alignment, while the transition involving octahedrally coordinated Fe^{3+} cations shows a parallel alignment to the applied field. This is consistent with previous studies and validates the accuracy of transition assignment.

5.3 Fabrication temperature dependent ferrimagnetic order

In this section, the properties of electronic transitions, observed in the dielectric function, are related to local cation disorder in ZnFe_2O_4 (ZFO) thin films and correlated with respect to the net magnetic response. The ZFO thin films were grown at 400 °C (ZFOT4), 500 °C (ZFOT5) and 600 °C (ZFOT6) by pulsed laser deposition on SrTiO_3 (100) substrates. The considerably high oxygen partial pressure of 0.016 mbar during fabrication was chosen in order to avoid formation of oxygen vacancies. The parameters, specific to the film fabrication, are listed in Table 3.1 of Chapter 3. The dielectric function feature, located at ~ 3.5 eV, is related to the transition involving tetrahedrally coordinated Fe^{3+} cations. The increase in transition amplitude with the decrease in substrate temperature during deposition shows a direct correlation to the enhancement of the ferrimagnetic order. The presence of tetrahedrally coordinated Fe^{3+} would enhance the dominating antiferromagnetic super-exchange interaction between tetrahedral and octahedral Fe^{3+} and is likely due to the inversion mechanism.

The XRD 2θ scans are shown in Figure 5.10 for the investigated thin films. Along with the substrate peak reflexes, the (400)- and (800)-reflexes of the spinel structure are observed with no additional secondary phases. An increase in the peak intensity is apparent with the increase in substrate temperature. This confirms highly oriented growth of the deposited films and an improvement of the crystal quality with increase in deposition temperature. A shift in the film peak towards higher angle (Figure 5.10 (b)) with the increase in growth temperature indicates a reduction of the lattice parameter. For 600 °C, the lattice constant is closest to the bulk value of 8.44 Å [94, 186–189]. The lattice constants were calculated by the Scherrer equation and extrapolated from $\cos^2(\theta)$, as described in Section 4.1.1, and are listed in Table 5.1. The variation in the lattice parameter and improvement in crystal quality are possibly due to the decrease in cation disorder. For example, a relaxation of the lattice in disordered normal spinel structure [49]. The changes are more evident for the increase in growth temperature from 400 °C to 500 °C, being smaller for further increase up to 600 °C. The film deposited at a substrate temperature of 300 °C was found to be X-ray amorphous.

Magnetization was measured at 5 K and 300 K as a function of applied magnetic field ($\mu_0 H$), and is shown in Figure 5.11 (a) and (b), respectively. The diamagnetic contribution from the substrate was subtracted from the presented

5.3. Fabrication temperature dependent ferrimagnetic order

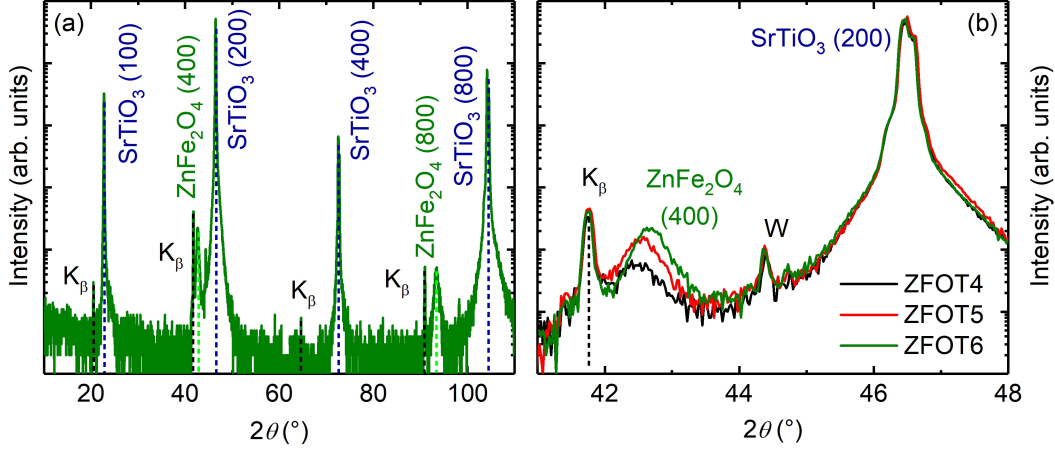


Figure 5.10: XRD 2θ scans for (a) ZFOT6 thin film grown at $\sim 600^\circ\text{C}$ and (b) for the ZFO thin films of different growth temperatures. Substrate reflexes, marked by K_β and W, correspond to Cu K_β and W L_α spectral lines of the X-ray tube, respectively.

Table 5.1: Calculated lattice parameter, thickness of the film and surface roughness, saturation magnetization M_S and remnant magnetization M_{Rem} measured at 5 K, transition energies for Gaussian (G) and critical point model (CPM₀) along with the amplitude of G_3 as well as the amplitude ratio, $G_3/(G_2+G_4)$, listed for each sample. The error, estimated for the specified values, is in the range of the last digit.

Sample	Lattice constant (Å)	Film thickness (nm)	Surface roughness (nm)	M_S (emu/g)	M_{Rem} (emu/g)	G_2 (eV)	CPM ₀ (eV)	G_3 (eV)	G_3 Amp ([1])	G_4 (eV)	Amp Ratio
ZFOT4	8.54	40.3	1.6	60.89	35.98	2.72	2.89	3.38	1.25	3.81	0.68
ZFOT5	8.51	41.7	1.3	27.80	15.73	2.51	2.72	3.49	0.44	3.98	0.46
ZFOT6	8.49	41.0	1.4	21.66	11.49	2.50	2.72	3.54	0.29	3.98	0.30

data. A ferrimagnetic order, exhibited by the three thin films, is evident by the magnetization hysteresis. The magnetization saturation was found to diminish with the increase in the deposition temperature (see Table 5.1). The rate of magnetization change was found to coincide with the variation in the crystallinity and the lattice parameter, observed in XRD, namely the variation is significant between the samples prepared at 400°C and 500°C , while a small decrease in magnetization with further increase in growth temperature (600°C) is visible only for measurements at 5 K (see Figure 5.11 (b)).

To understand the dependence of magnetization on the deposition temperature, the dielectric function was determined using spectroscopic ellipsometry. Based on the resonance energies, transitions were assigned from previous studies of the optical as well as magneto-optical properties of this material [48, 185, 190].

5.3. Fabrication temperature dependent ferrimagnetic order

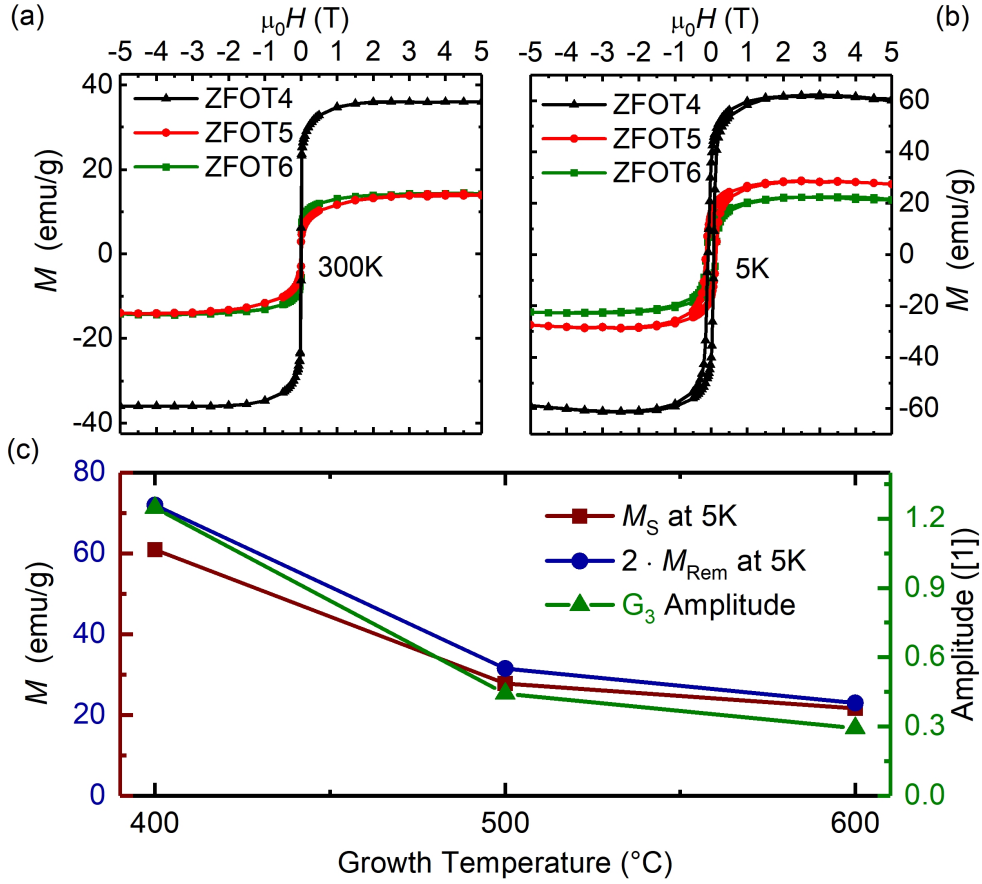


Figure 5.11: Magnetization as a function of applied magnetic field at (a) room temperature and at (b) 5 K. (c) Magnetization saturation and twice of remnant magnetization measured at 5 K as well as the amplitude of the transition involving tetrahedrally coordinated Fe^{3+} cations, obtained from the model dielectric function.

The absorption coefficient as well as the Kramers-Kronig consistent optical constants, calculated from the parametric MDF approximation, are shown in Figure 5.12 and 5.13, respectively. Transition energies for each oscillator and relevant amplitudes are listed in Table 5.1.

Figure 5.12 shows the absorption coefficient for the three thin films, deduced from the numerical approximation. A clear difference in the absorption bands is visible for the three films, with the main features located at ~ 3.9 eV and ~ 6.1 eV. In contrast to the Fe_3O_4 MDF spectra, Section 5.1, the low absorption below 2 eV indicates a low concentration of Fe^{2+} cations [48, 49, 185, 190]. The MDF spectra in the measured spectral range consists of transitions between the O 2p band and 3d and 4s bands of Fe^{3+} and Zn^{2+} cations, Figure 5.13 (top panel). While functions below ~ 4.5 eV are assigned to transitions involving 3d bands of

5.3. Fabrication temperature dependent ferrimagnetic order

Fe^{3+} cations, functions above ~ 4.5 eV correspond to transitions from O 2p band to 4s as well as higher lying bands of Fe^{3+} cation and to the 4s band of Zn^{2+} cation.

The red-shift of G_2 as well as a blue-shift of G_4 is evident with the decrease in deposition temperature from 400°C to 500°C , Figure 5.13 (inset). The two electronic bands arise from crystal field split of states with energy of Δ_{Oh} ($=10Dq$), which is related to the energy difference between transitions from the O 2p band to t_{2g} and e_g bands of the octahedral Fe^{3+} cations, see Section 2.2. The crystal field energy, Δ_{Oh} , was found to increase from ~ 1.09 eV to ~ 1.48 eV with the increase in deposition temperature from 400°C to 600°C . The latter value matches the one of the bulk spinel ferrite and indicates a well ordered spinel structure [191, 192].

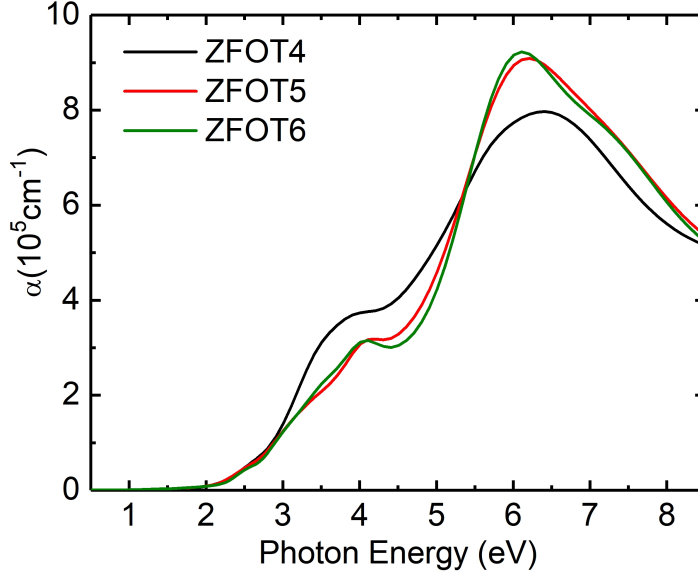


Figure 5.12: Absorption coefficient α , derived from the numerical dielectric function approximation.

The transition located at ~ 3.5 eV hints to the presence of Fe^{3+} on tetrahedral lattice sites, and serves as evidence for disorder within the normal spinel structure. In the previous section, this transition exhibited the strongest magneto-optical response for ZFO thin films grown at low temperature. Therefore, this transition involves tetrahedrally coordinated Fe^{3+} cation and can be assigned to an electronic transition from O 2p to tetrahedrally coordinated Fe^{3+} cation [30, 190]. This peak becomes more pronounced as the normal spinel becomes more inverted, and is highest for Fe_3O_4 inverse spinel [193, 194]. The increase in amplitude of this transition with decreasing substrate temperature is directly correlated to

5.3. Fabrication temperature dependent ferrimagnetic order

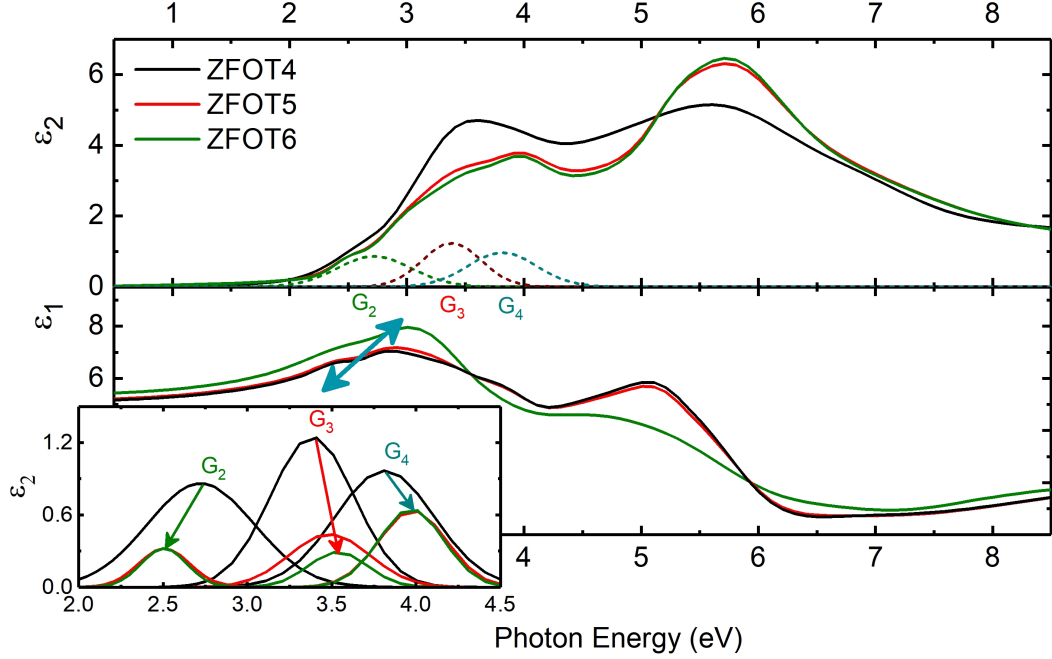
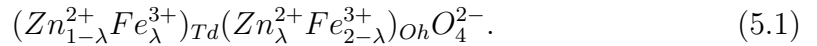


Figure 5.13: Real (bottom) and imaginary part (top) of the Kramers-Kronig consistent dielectric function, calculated from the parametric approximation for ZFO thin films. The inset shows changes in amplitude and energy of three oscillators, G_2 , G_3 , and G_4 , with respect to the deposition temperature.

the increase in magnetization saturation as well as the remnant magnetization, measured at 5 K (see Figure 5.11 (c) and Table 5.1).

Since the increase of the function amplitude of G_3 is greater than the amplitude increase of G_2 and G_4 with decreasing deposition temperature, see Figure 5.13 (inset) and amplitude ratio in Table 5.1, the following two phenomena are possible. Firstly, an inversion mechanism where Zn^{2+} moves to the octahedral site and Fe^{3+} moves to the tetrahedral site, with decreasing growth temperature, *Case 3* in Section 2.5. This follows Equation 5.1, where the corresponding degree of cation disorder is represented by the inversion coefficient λ .



On the other hand, presence of Fe^{3+} cations on nominally unoccupied tetrahedral sites is also possible, *Case 2* in Section 2.5, and has been investigated in previous works [29, 31, 33]. Nonetheless, the presence of tetrahedral Fe^{3+} cations results in the oxygen mediated antiferromagnetic super-exchange interaction between Fe^{3+} on two sites to dominate over the ferromagnetic coupling between octahedral Fe^{3+} cations. Therefore, the increase in tetrahedral Fe^{3+} cation allo-

5.3. Fabrication temperature dependent ferrimagnetic order

cation is directly correlated to the increase in the overall ferrimagnetic order with the decrease in deposition temperature.

Summary:

In this section, the variation of the magneto-static properties of ZnFe_2O_4 thin films was presented as a function of the substrate temperature during deposition. The changes in the octahedral and tetrahedral site occupancy are evident by the electronic transition amplitude in the model dielectric function spectra, obtained from spectroscopic ellipsometry. The increase in Fe^{3+} cation allocation to the tetrahedrally coordinated lattice sites is indicative of cation disorder and serves as a reasonable explanation for the observed increase in the ferrimagnetic order with the decrease in the fabrication temperature.

5.4 Thermally induced structural stabilization

In this section, the magnetic properties of disordered spinel ZnFe_2O_4 films are examined as a function of thermal treatment temperature and atmosphere. The changes in the MDF spectra provide an insight into the dominant magnetic interactions, responsible for the observed magnetic behavior. The creation of oxygen vacancies and spinel structure relaxation toward the normal configuration were determined to be responsible for the increase and decrease in the net magnetic response, respectively.

ZnFe_2O_4 films were fabricated at low temperature (300°C) as well as high (HP ZFO) and low (LP ZFO) oxygen partial pressures. The samples were then split into four pieces of roughly the same size. The pieces of HP ZFO and LP ZFO were annealed in the temperature range from 250 to 375°C in argon and oxygen atmospheres, respectively. The base pressure of the annealing chamber was kept constant at 100 mbar throughout the procedure. Further parameters, specific to the film fabrication and treatment, are listed in Table 3.1 of Chapter 3. The choice of low (high) deposition pressure and oxygen (argon) annealing atmosphere was made in order to eliminate (facilitate) oxygen vacancies in the thin films. In order to check the reproducibility of the sample magnetic response, induced by thermal annealing, magnetization of two nominally identical (Ar250) films was measured and a deviation within 4.7% was determined.

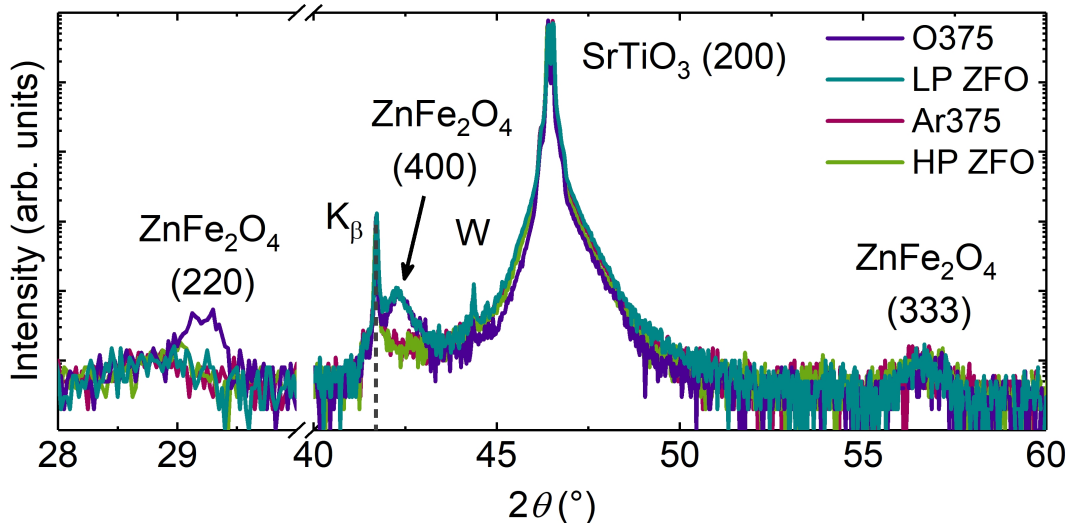


Figure 5.14: XRD wide-angle 2θ scans for as-deposited films and after annealing at 375°C . Substrate reflexes, marked by K_β and W , correspond to $\text{Cu } K_\beta$ and $\text{W } L_\alpha$ spectral lines of the X-ray tube, respectively.

5.4. Thermally induced structural stabilization

As mentioned in the previous section, the ZnFe_2O_4 films, deposited at the same temperature and high pressure, were found to be XRD-amorphous. As it is in this case, the HP ZFO is XRD-amorphous and shows no changes upon thermal treatment, Figure 5.14. The LP ZFO film, on the other hand, exhibits a phase of (100) orientation. After annealing at the highest temperature, the O375 film shows a possible secondary phase of (110) orientation, while the (400) reflex remains unperturbed by the treatment. Interestingly, an additional phase might be present in the films depicted in Figure 5.14, evident by the (333) reflex. However, the resolution of the used device is not sufficient to investigate the possible phases appropriately.

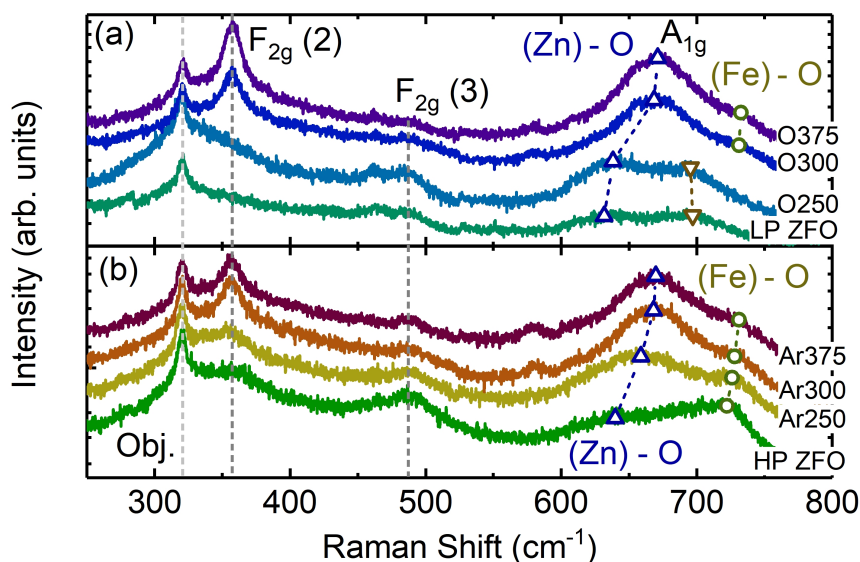


Figure 5.15: Raman spectra of films annealed in (b) argon and (c) oxygen atmosphere with temperatures indicated. The peak resulting from the objective used in the experimental set-up, F_{2g} modes as well as component contributions to the A_{1g} symmetry mode are indicated by the dashed lines and open symbols, respectively.

Raman scattering spectra demonstrates a considerable change in the phonon interactions with the increase in annealing temperature. In particular two Raman-active modes become clearly distinguished after annealing in either argon or oxygen atmosphere, namely the $\text{Fe}_{2g}(2)$ and A_{1g} modes, Figure 5.15. The $\text{Fe}_{2g}(3)$ Raman active mode, located at 356 cm^{-1} , is related to the asymmetric stretching of oxygen bonds of octahedral $(\text{Fe})_{Oh}\text{O}_6$ configuration [128, 131]. While the mode position remains constant with increase in annealing temperature, the increase in its intensity is most significant after thermal treatment in oxygen, as opposed to argon atmosphere.

5.4. Thermally induced structural stabilization

The broad A_{1g} Raman active mode, consists of possibly two components and is related to symmetric stretching of oxygen anions of tetrahedral $(Zn)_{Td}O_4$ and $(Fe)_{Td}O_4$ symmetry coordination, located at ~ 630 and $\sim 700\text{ cm}^{-1}$ in the LP ZFO spectra. The low energy A_{1g} symmetry mode component is visible for as-deposited films and exhibits a blue-shift to higher energies with increase in annealing temperature in both atmospheres. The high energy A_{1g} component is clearly distinguishable in the LP ZFO and O250 film spectra only. Additional high energy phonon mode, located at $\sim 720\text{ cm}^{-1}$, is also considered to be of A_{1g} symmetry and has previously been related to oscillations of oxygen in an uncompleted tetrahedral $(Fe)_{Td}O_4$ configuration [119, 131]. This mode is visible in the HP ZFO film spectra, and demonstrates a weak blue-shift with the increase in annealing temperature.

Interestingly, a significant change in the intensity of the A_{1g} mode occurs upon annealing at $250\text{ }^\circ\text{C}$, while of the $Fe_{2g}(2)$ mode occurs after annealing at $300\text{ }^\circ\text{C}$ in argon atmosphere. For the sample series annealed in oxygen, a clear difference in the Raman spectra occurs after annealing at $300\text{ }^\circ\text{C}$, at which temperature, both $Fe_{2g}(2)$ and A_{1g} modes become clearly distinguishable.

The surface morphology of the investigated thin films is depicted in Figure 5.16. Statistical grain analysis was applied to determine the relative grain distribution and the RMS roughness. Smooth surface with stepped-like structures and an RMS of 0.1 nm was found to cover the HP ZFO film. Annealing the film in argon resulted in gradual formation of needle-like structures with a highest RMS roughness of 3.5 nm for the Ar375 film. A rough surface with densely spaced needle-like structures was found for LP ZFO film. Upon annealing the film in oxygen, the RMS decreased from 4.9 nm to 0.3 nm for LP ZFO and O375, respectively. A systematic increase (decrease) in the surface roughness is visible with the increase in annealing temperature in argon (oxygen) atmosphere.

Figure 5.17 shows magnetization as a function of applied magnetic field, measured at room temperature as well as (inset) 5 K . It is important to note that after subtraction of the diamagnetic contribution, arising from the substrate, a paramagnetic component was observed for films annealed at temperatures $\geq 300\text{ }^\circ\text{C}$. Room temperature magnetization saturation as well as the "S" shape of the magnetic hysteresis with negligible coercive field was observed for as-deposited films and after annealing at $250\text{ }^\circ\text{C}$. Magnetization was found to increase after annealing the HP ZFO film in $250\text{ }^\circ\text{C}$ in argon atmosphere, when measured at room temperature and 5 K . Upon further annealing, the magnetic moment diminished and remained nearly constant for annealing temperatures $\geq 300\text{ }^\circ\text{C}$. The main dif-

5.4. Thermally induced structural stabilization

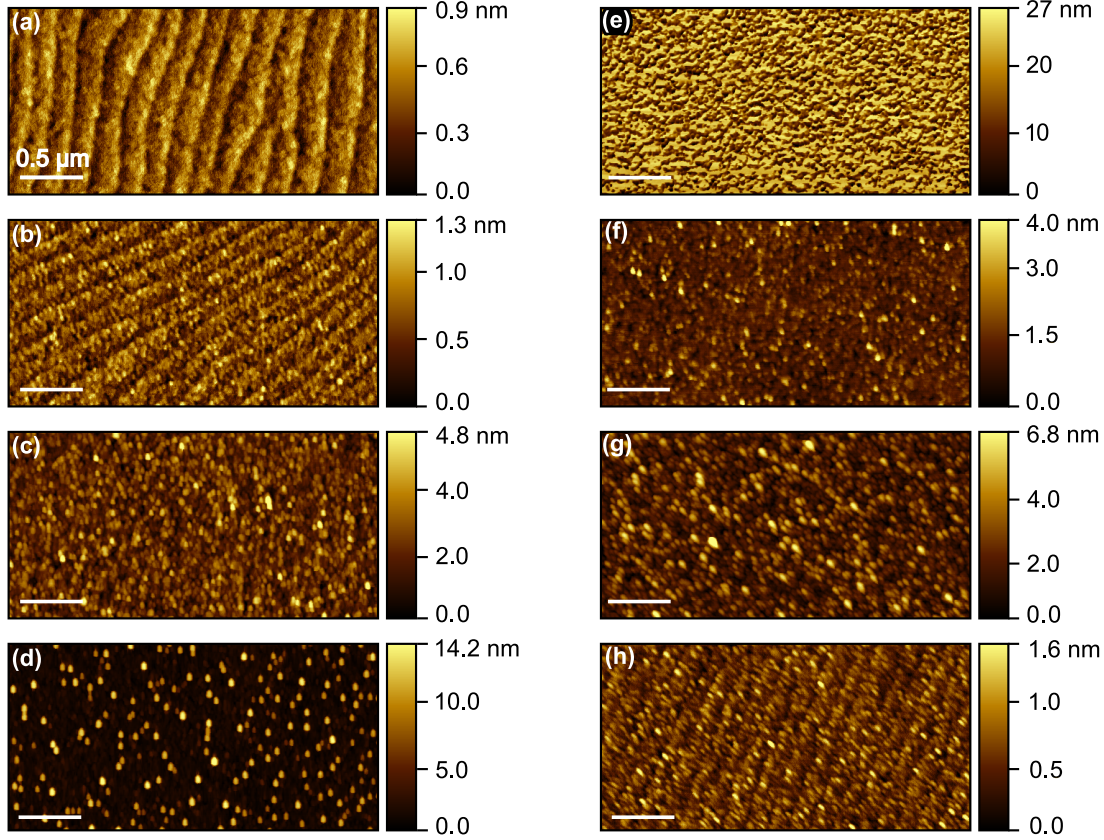


Figure 5.16: Surface morphology scans of (a) HP ZFO, (b-d) Ar250-Ar375, as well as (e) LP ZFO and (f-h) O250-O375 thin films. The lateral distance of $0.5 \mu\text{m}$ is indicated in each each scan.

ference in the hysteresis curve of LP ZFO and O250 is the more pronounced S shape of the room temperature hysteresis, Figure 5.17 (b), indicative of a more magnetically hard material. A decrease in magnetization was observed upon further increase in treatment temperature. The magnetization measurements at 5 K displayed a similar behavior to that of room temperature, apart from the stronger pronounced coercive field, listed in Table 5.2.

Volume magnetization was measured as a function of temperature in the FC and ZFC mode with an applied field of $\mu_0 H = 0.1 \text{ T}$, Figure 5.18. All samples showed magnetic irreversibility and a spin freezing temperature (T_{SF}) below room temperature. A significant magnetization increase was observed for the HP ZFO thin film upon annealing at 250°C in argon atmosphere. A convex magnetization behavior, a cusp, was exhibited by the ZFC curves below T_{SF} and becomes more pronounced with increase in annealing temperature in argon and oxygen atmosphere. Such behavior of the ZFC is characteristic of a near-to-bulk sample structure and a lack of magnetic moment is expected in the vicinity of the Néel

5.4. Thermally induced structural stabilization

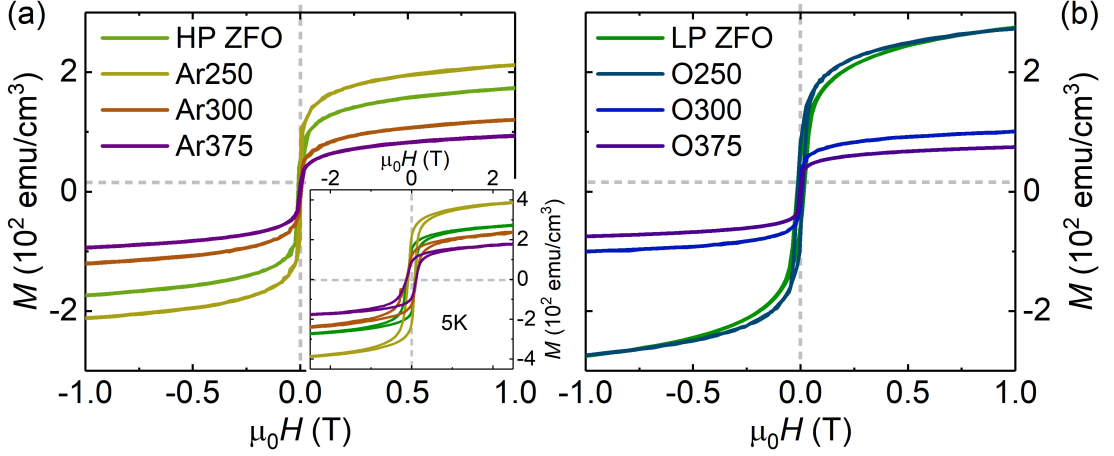


Figure 5.17: Volume magnetization measured at 300 K as a function of applied magnetic field, $\mu_0 H$, for HP and LP ZFO films annealed in (a) argon and (b) oxygen atmosphere, respectively. The inset shows measurements at 5 K for the samples annealed in argon.

temperature [31]. The FC curve, on the other hand, remains nearly constant or decreases with decreasing temperature, below T_{SF} . The irreversibility of the temperature dependent magnetization is characteristic of spin glass, cluster glass, or superparamagnetic material system [37, 38, 195]. With the increase in the thermal treatment temperature, a decrease in the difference between the ZFC and FC curves is observed.

Absorption coefficient was calculated from the numerical B-Spline approximation of the dielectric function, Figure 5.19. The spectra is dominated by a strong absorption at ~ 6 eV, which increases upon the increase in annealing temperature. The increase in absorption in the high energy range becomes significant after annealing the LP ZFO at temperatures ≥ 300 °C, while a gradual increase is observed with increase in temperature in argon atmosphere. The feature at ~ 4 eV, on the other hand, decreases with the increase in annealing temperature. In contrast to the spectra discussed in Section 5.3, absorption in the low energy range is apparent for the LP ZFO and O250 thin films, which is caused by the presence of Fe^{2+} cations arising from the low oxygen partial pressure during fabrication.

The imaginary component of the MDF is depicted in Figure 5.20. First and foremost, a clear difference in the MDF is visible between the as-deposited thin films. Most notably is the L_0 contribution to the MDF of the LP ZFO as compared to that of HP ZFO. The low energy absorption arises from the electronic transition between the d orbitals of Fe^{2+} cations, and therefore corresponds to the presence

5.4. Thermally induced structural stabilization

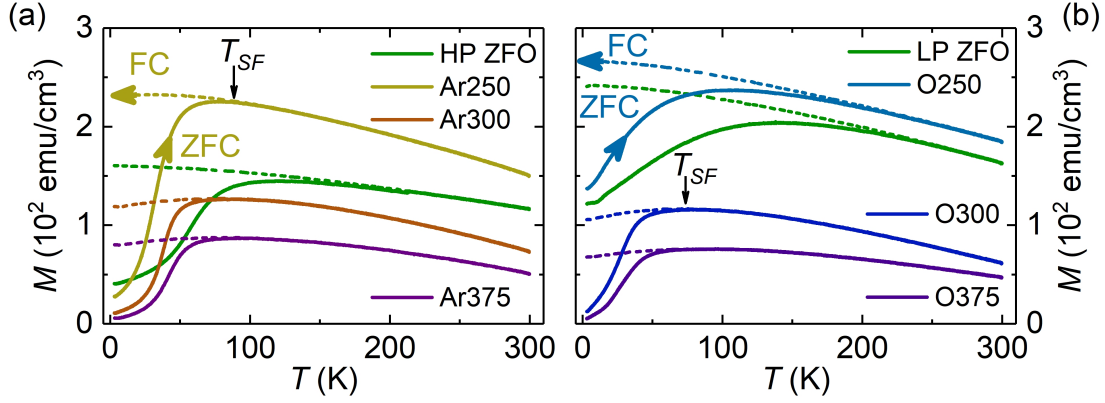


Figure 5.18: Volume magnetization as a function of temperature, at applied field of $\mu_0 H = 0.1$ T, for HP and LP ZFO films annealed in (a) argon and (b) oxygen atmosphere, respectively. The arrows correspond to the denoted FC or ZFC measurement mode and the spin freezing temperature T_{SF} is indicated.

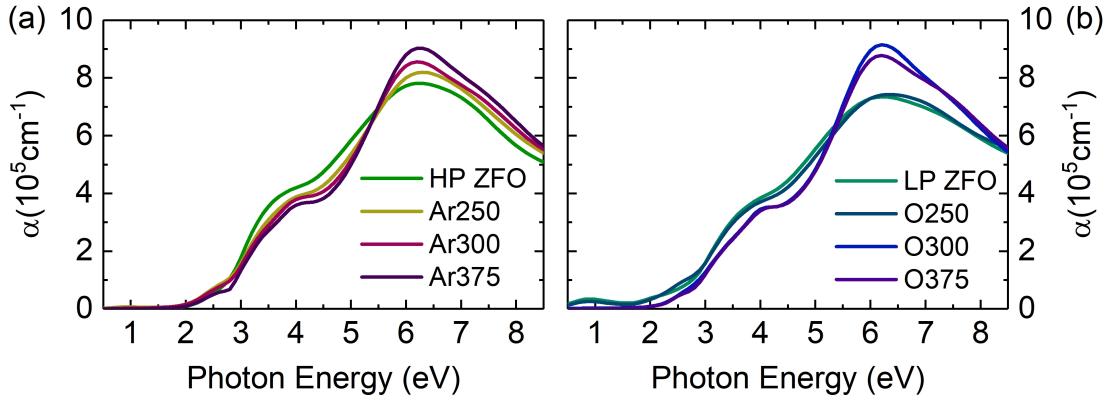


Figure 5.19: Absorption coefficient, determined from the numerical approximation, for HP and LP ZFO films annealed in (a) argon and (b) oxygen atmosphere, respectively.

of Fe^{2+} in the film deposited at a low oxygen pressure. In contrast to LP ZFO, the HP ZFO has a higher contribution from the G_3 function, depicted in Figure 5.20.

As the HP ZFO is annealed in argon, the G_3 peak decreases significantly. Since the G_3 function has previously been assigned to a transition involving Fe_{Td}^{3+} , its decrease would indicate a decrease in disorder on the tetrahedral site. Coincidentally, the spin freezing temperature also exhibits a decrease from 120 to 80 K, listed in Table 5.2 and depicted in Figure 5.21 (a). The decrease in T_{SF} has previously been correlated to a decrease in cation inversion [31], therefore a less disordered spinel configuration is expected in Ar250. Surprisingly, an increase in magnetization is observed, Figure 5.21. Simultaneously, the low energy L_0 peak

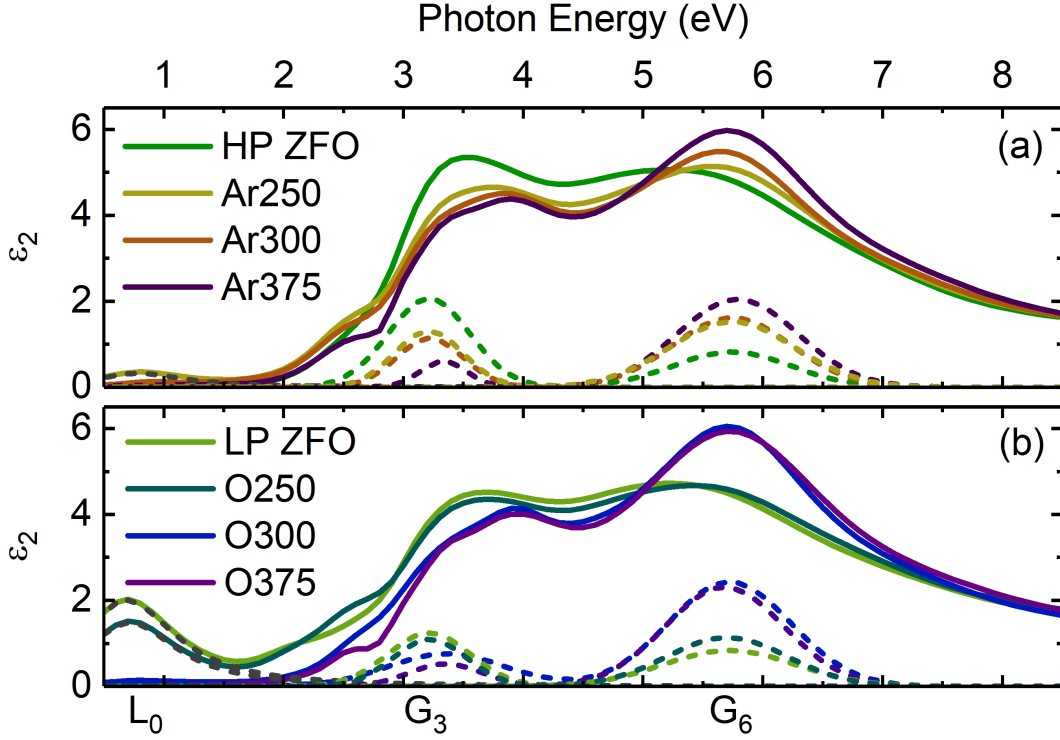


Figure 5.20: Imaginary component of the model dielectric function shown for LP and HP ZFO films annealed in (a) oxygen and (b) argon atmosphere, respectively. Contribution of the indicated functions is depicted by dashed lines. The L_0 function is indicated by gray dashed lines.

becomes apparent in the Ar250 MDF spectrum, indicating a possible presence of Fe^{2+} cations. Therefore, if we consider that the disordered HP ZFO follows the spin-glass behavior and exhibits geometrical frustration due to oxygen mediated AF SE interactions involving Fe_{Td}^{3+} cations, then annealing the film in argon would reduce this frustration by removing the mediating oxygen anions. As a consequence, the structure would go to a more relaxed state and the magnetic response would be mainly due to the oxygen vacancies, evident by increase in Fe^{2+} transition contribution to the MDF line-shape.

Upon annealing the LP ZFO film in oxygen, the O250 film exhibits only a slight increase in the M_{Rem} and a decrease in T_{SF} . This could be explained by a decrease in Fe^{2+} cation concentration, due to the oxygen atmosphere. At which point, the oxygen anions would contribute to the decrease in cation disorder by producing Fe_{Oh}^{3+} cations and strengthening the magnetic SE interaction caused by Fe_{Td}^{3+} .

5.4. Thermally induced structural stabilization

Annealing the LP ZFO film at 300 °C in oxygen results in the lowest value of T_{SF} as well as M_{Rem} and the crystal recrystallization toward a normal spinel configuration is apparent in MDF and in Raman spectra for O300. The MDF spectra exhibit a decrease in the G_3 and an increase in the G_6 function contribution, similar to the behavior discussed in Section 5.3. Interestingly, with the increase in annealing temperature ≥ 300 °C the T_{SF} as well as M_{Rem} of films annealed in oxygen displays an increase. For the films annealed in argon, the magnetic response remains nearly constant with further increase in annealing temperature. No significant changes in neither the Raman nor the MDF spectra are observed to explain this behavior. On the other hand, considerable increase in the magnetic response has been recently demonstrated for annealing in vacuum at temperatures ≥ 450 °C and attributed to oxygen deficient environment during the process of inversion recovery [195]. Furthermore, various theoretical calculations have been correlated to the experimental findings by the group of C. Rodriguez Torres in La Plata, Argentina. Interestingly, only recently they have considered $ZnFe_2O_4$ surface termination by Fe_{Td}^{3+} cation in relation to the various proposed magnetic behaviors.

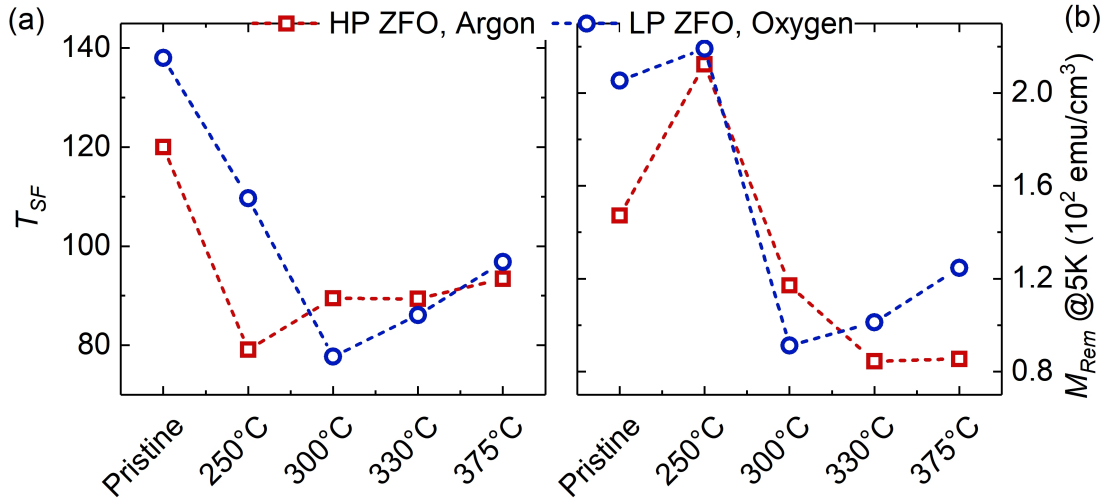


Figure 5.21: (a) Spin freezing temperature T_{SF} and magnetization remanence M_{Rem} , measured at 5 K, as a function of annealing temperature. The red squares correspond to HP ZFO annealed in argon, while blue circles are LP ZFO annealed in oxygen at specified temperatures.

5.4. Thermally induced structural stabilization

Table 5.2: Values of the RMS surface roughness (d_{SR}) determined by statistic grain analysis from AFM, coercivity field (H_{Coer}), magnetization remanence (M_{Rem}), both measured at 5 K and spin freezing temperature (T_{SF}) for the corresponding thin films.

Sample	d_{SR} (nm)	H_{Coer} (mT)	T_{SF} (K)	M_{Rem} (emu/cm ³)
HP ZFO	0.1	96.5	120.0	147.2
Ar250	0.2	82.8	79.1	212.3
Ar300	0.4	125.8	89.5	117.1
Ar330	0.7	119.1	89.4	84.5
Ar375	3.5	117.5	93.4	85.5
LP ZFO	5.0	103.8	138.0	205.3
O250	1.0	95.5	109.7	219.1
O300	0.7	104.9	77.7	91.2
O330	0.5	107.4	86.1	101.2
O375	0.3	132.1	96.8	124.7

Summary:

In conclusion, disordered ZnFe₂O₄ thin films, deposited at low and high oxygen partial pressures, demonstrated differences in their crystallinity, surface morphology and absorption. Upon annealing the HP ZFO in argon at 250 °C, the rise in magnetic response and the decrease in spin freezing temperature was attributed to a relaxation of a geometrically frustrated system. In this case, the degree of disorder would decline and the magnetic response would likely be due to the presence of oxygen vacancies, evident in the MDF spectra by the decrease and increase of the transitions involving Fe_{Td}³⁺ and Fe_{Oh}²⁺ cations, respectively. After annealing at 300 °C and above, both LP and HP ZFO would undergo structural relaxation towards a normal spinel, thereby initially diminishing the magnetic response. Since no direct correlation between the increase in the magnetic behavior and increase in surface roughness has been drawn, more information is necessary to determine the role of cation configuration distribution with the thin film sample on the net magnetic response.

5.5 Cation configuration in dependence on the Zn concentration

In this section, the deviation of cation configuration from the expected equilibrium state as well as its distribution within the thin film is related to the magnetic behavior, as the predominant bulk cation configuration transforms from inverse to normal spinel with the increase in Zn concentration. For this purpose, $\text{Zn}_x\text{Fe}_{3-x}\text{O}_4$ thin films were fabricated by PLD on TiN/(100)MgO substrates with a step-and-terrace surface morphology. The Zn concentration in films with $x = 0$ (ZnX0), 0.26 (ZnX1), 0.56 (ZnX2), 0.87 (ZnX3) and 1.26 (ZnX4) was determined by EDX. The chemical composition was estimated by theoretical approximation of the XPS Fe 2p and 3p core level surface spectra as well as of the bulk NIR-VUV dielectric function, dominated by electronic transitions from O 2p to Fe 3d and 4s orbitals. Magnetic strength demonstrates a strong dependence on cation distribution throughout the layered structure, with respect to the degree of inversion in the predominant cation configuration. The ZnX0 film exhibits a ferrimagnetic behavior, see also Section 5.1, and contains anti-phase boundaries. The ZnX4 film shows superparamagnetic behavior at room temperature, characteristic of nanostructure formation. The applied concept provides a predictable approach for manipulating the crystalline structure assembly and the results yield an adequate quantification of the surface and bulk cation site occupancy with respect to the net magnetic moment.

5.5.1 Structural property determination

First and foremost, the complexities involved in the fabrication of the films by PLD are examined, see also Section 3.1. Crystal quality and cation configuration distribution within the spinel oxide film strongly depends on the substrate and its surface as well as the oxidizing or reducing environment during deposition. This fabrication approach was chosen for the purpose of film integration in spintronic device application as well as to ensure an adequate formation of magnetite material for the $x = 0$ film [196]. The choice of a non-oxide buffer layer as well as argon atmosphere during deposition allows to influence the resulting structure in the following ways. Firstly, since the TiN buffer layer does not act as an oxygen reservoir during film crystallization, an oxygen-poor interface is expected. The TiN buffer layer on (100) MgO substrate was optimized prior to spinel film deposition [51]. Using argon atmosphere further ensures an oxygen poor fabrication environment during crystallization. Hence, the incorporation of oxygen

5.5. Cation configuration in dependence on the Zn concentration

anions, originating only from the target material, could be deterministic of the iron cation configuration distribution within the spinel film in dependence on the Zn concentration.

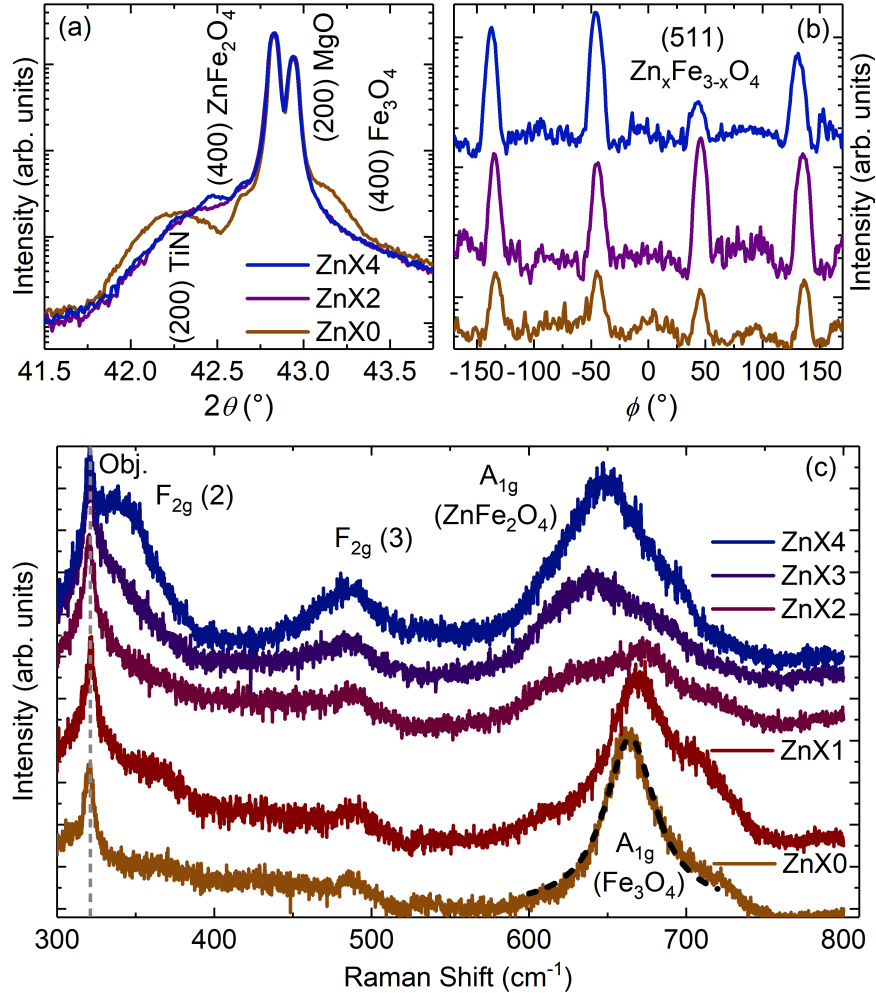


Figure 5.22: (a) XRD diagram (2θ scan) of $\text{Zn}_x\text{Fe}_{3-x}\text{O}_4$ films. (b) ϕ scan of asymmetric (511) $\text{Zn}_x\text{Fe}_{3-x}\text{O}_4$ peak. (c) Raman spectra, recorded for all thin films at room temperature, with F_{2g} and A_{1g} modes indicated. Lorentzian fit is presented for the A_{1g} (Fe_3O_4) mode. The peak, resulting from the objective used in the experimental set-up, is indicated by a vertical dashed line.

The 2θ XRD scan shows (100) orientation of the $\text{Zn}_x\text{Fe}_{3-x}\text{O}_4$ thin films and the fourfold symmetry of the (511) peak in the ϕ scan indicates epitaxial growth, see Figure 5.22(a) and (b). TiN buffer layer also shows a (100) orientation with the reflex in close vicinity of the (100) reflexes of the MgO substrate and spinel films. Due to the close vicinity of the TiN buffer layer, MgO substrate and the $\text{Zn}_x\text{Fe}_{3-x}\text{O}_4$ film reflexes in the 2θ scans, the discussion is restricted to a rough estimation of the film cubic lattice parameter. A lattice mismatch of $\pm 0.4\%$ is

5.5. Cation configuration in dependence on the Zn concentration

expected between Fe_3O_4 ($a \sim 8.39 \text{ \AA}$) as well as ZnFe_2O_4 ($a \sim 8.44 \text{ \AA}$) and the TiN buffer layer ($2 \times a \sim 8.42 \text{ \AA}$) [47]. The experimental lattice parameter of $x = 0$ film ($a \sim 8.38 \text{ \AA}$) matches the Fe_3O_4 literature value. With the increase in Zn concentration, the lattice constant for $x \geq 0.26$, ZnX1-4, ($8.50 - 8.54 \text{ \AA}$) does not follow the predicted increase, but is in the vicinity of values, determined for disordered ZnFe_2O_4 , see Section 5.3 [30, 32, 90].

A spinel structure of the $O_h^7 (Fd3m)$ space group is expected to exhibit five first order Raman active modes ($A_{1g} + E_g + 3F_{2g}$) at room temperature. In our case, however, only three phonon active modes are clearly visible, see Figure 5.22(c). The modes above 600 cm^{-1} (A_{1g}) mostly correspond to symmetric stretch of oxygen atoms of the tetrahedral (TdO_4) symmetry, while the low frequency modes correspond to the symmetric and asymmetric bending of oxygen with respect to the cations of octahedral (OhO_6) symmetry [128, 131, 132]. From a Lorentzian fit to the A_{1g} mode ($\omega = 664 \text{ cm}^{-1}$) for the ZnX0 film, its width (Γ) was determined to be 39.5 cm^{-1} . Both ω and Γ are slightly lower than the ones reported for a Fe_3O_4 film, exhibiting 2-D growth on (100) TiN and a good crystal quality with no phase boundaries [128]. With increase in the Zn concentration, the A_{1g} (Fe_3O_4) exhibits a blue-shift and a decrease in intensity, while the A_{1g} (ZnFe_2O_4) becomes more apparent and also exhibits a blue-shift to 649 cm^{-1} for the ZnX4 film. The A_{1g} (ZnFe_2O_4) mode position is in good agreement with the position reported in literature [131]. An overlap of the A_{1g} (Fe_3O_4) and A_{1g} (ZnFe_2O_4) for the films of intermediate Zn content values can be assumed. While the F_{2g} (3) mode, located at $\omega = 487 \text{ cm}^{-1}$, is visible for all films, the F_{2g} (2), $\omega = 338 \text{ cm}^{-1}$, is apparent only for the ZnX4 film. The broad nature of the phonon modes likely indicates the heterogeneous sublattice occupation of our film structures.

Lastly, the surface morphology of the previously optimized substrate layer consists of step-and-terrace structures [51]. The terrace length and step height are $\sim 0.2 \mu\text{m}$ and $\sim 0.2 \text{ nm}$, respectively. The uniform distribution of these structures on the substrate layer would induce a consistent break in the spinel crystallization periodicity and would facilitate the likely formation of phase boundary defects, as previously reported for Fe_3O_4 [46]. This is exactly the case for the ZnX0 film, where the TiN surface step height roughly corresponds to one fourth of the inverse spinel Fe_3O_4 cubic lattice parameter. The surface morphology of this film consists of densely and sparsely distributed porous and columnar structures, respectively, Figure 5.23(a). The distance between both types of structure was found to be a multiple of the substrate layer terrace length. The depth of the porous interface

5.5. Cation configuration in dependence on the Zn concentration

structures corresponds to approximately three ZnX0 unit cells (~ 2.5 nm). An intermixing layer of the interface was reported with similar thickness by Xiang *et al.* due to Ti diffusion into Fe_3O_4 [196]. The 2-D autocorrelation image, Section 4.2.1, of the coalesced columnar island structures, occupying 7.3% of the scanned area, allows an estimation of the layer boundary formation directions. The perpendicularity of the two predominant boundary directions indicates homogeneous material arrangement along the uniform TiN/(100)MgO substrate layer step-and-terrace structures. The root mean square (RMS) of the surface roughness was found to decrease from 9.9 to 2.3 nm with increase in Zn content from 0 to 0.56, see Figure 5.23(a - c). Interestingly, a smooth surface with an RMS of 0.1 nm was observed for the ZnX3 film with $x = 0.87$, Figure 5.23(d). Furthermore, the ZnX4 film with highest Zn concentration, $x = 1.26$, contains sparsely and irregularly spaced grain structures, RMS of 1.2 nm, on top of a stepped interface layer, Figure 5.23(e). Surface morphology of our films could suggest the nature of layer crystallization. For example, phase boundaries, resulting in island coalesce (ZnX0), a smooth surface, due to homogenous layer formation (ZnX3), or nanostructure formation, evident by a step-and-terrace interface (ZnX4), could be indicative of the cationic architecture of our films.

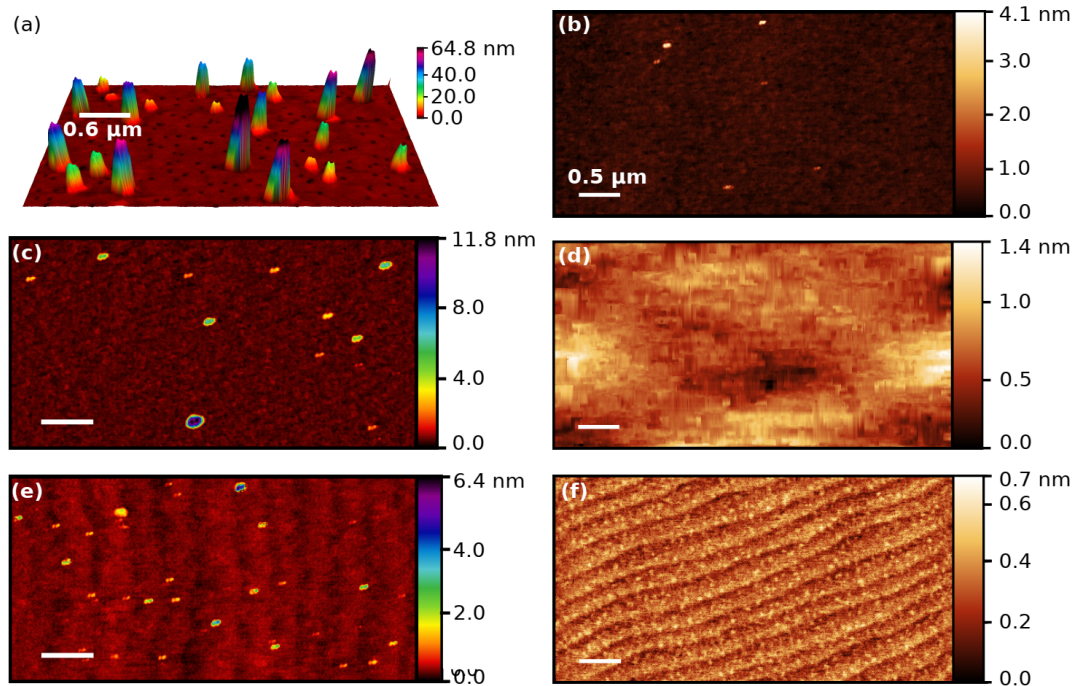


Figure 5.23: (a) Surface morphology of ZnX0 film with lateral distances between the island and porous interface structures indicated. Surface morphology of (b) ZnX1, (c) ZnX2, (d) ZnX3, (e) ZnX4 and (f) TiN/(100)MgO thin films.

5.5. Cation configuration in dependence on the Zn concentration

5.5.2 Composition characterization

The chemical composition in the near-surface region was estimated from the analysis of the Fe and Zn core-levels in the XPS spectra. The core level maximum binding energies of Fe 3p, 2p_{1/2} and 2p_{3/2} core levels for ZnX0 are in good agreement with those reported for Fe₃O₄ [138]. With the increase in Zn concentration from 0 to 1.26, the core level maximum binding energies of Fe 3p and 2p_{1/2} exhibit a blue-shift of 0.28 and 0.40 eV, respectively. The core level maximum of Zn 2p_{1/2}, on the other hand, shifts from 1021.4 eV [50] to lower binding energy by 0.17 eV as Zn content increases from 0.26 to 1.26. Furthermore, the final state shake feature formation, indicated by the arrow in Figure 5.24(a), located at ~ 719 eV, is due to the overlapping satellite contribution of each cation state. Therefore, the reduction in the diversity of Fe species strengthens the final shake feature. This is likely due to the decrease in Fe_{Oh}²⁺ cation contribution with Zn²⁺ incorporation into the lattice. In order to maintain neutrality of charge, as Zn²⁺ replaces Fe³⁺ on the tetrahedral lattice sites, the spinel ferrite undergoes an electronic charge redistribution, resulting in Fe_{Oh}²⁺ depletion. This is clearly demonstrated in the near-surface region by the diminishing intensity of the low-binding energy shoulder. Furthermore, the strong presence of the Fe_{Oh}³⁺ cation state was found to dominate both of the Fe core-level spectra. The relative ratio of trivalent cation concentrations on *Td*- to *Oh*-sites exhibits a monotonic decrease from 0.36 to 0.22 and then an increase to 0.27 with the increase in Zn substitution from 0 to 0.87 and to 1.26. The chemical composition of the film structures in the near-surface region was found to be abundant (deficient) in Fe_{Oh}³⁺ (Fe_{Td}³⁺) cation content, confirming the likely Fe_{Oh}³⁺ surface termination.

The chemical composition in the film bulk region was estimated by the theoretical approximation of the dielectric function spectra using line-shape MDF. Based on the patterns, arising from Zn²⁺ incorporation, we assigned the approximation functions ≥ 1 eV to electronic transitions involving 3d as well as 4s orbitals of Fe_{Td}³⁺, Fe_{Oh}³⁺ and Fe_{Oh}²⁺ cations. The transition ≤ 1 eV was assigned to a d-d orbital transition of Fe_{Oh}²⁺. It exhibits a blue-shift with increasing Zn content, and the decrease in peak intensity was previously related to a reduction in carrier concentration [32]. Individual bulk cation concentration, relative to the stoichiometric composition, was estimated by the 3d and 4s orbital transition contribution (oscillator strength) to the MDF line-shape, shaded regions in Figure 5.24(b). Preservation of charge neutrality in our system is more evident in the bulk than the near-surface region. The relative Fe²⁺ cation content was found to deplete nearly at a linear rate (-0.95) with the increase in Zn concentration,

5.5. Cation configuration in dependence on the Zn concentration

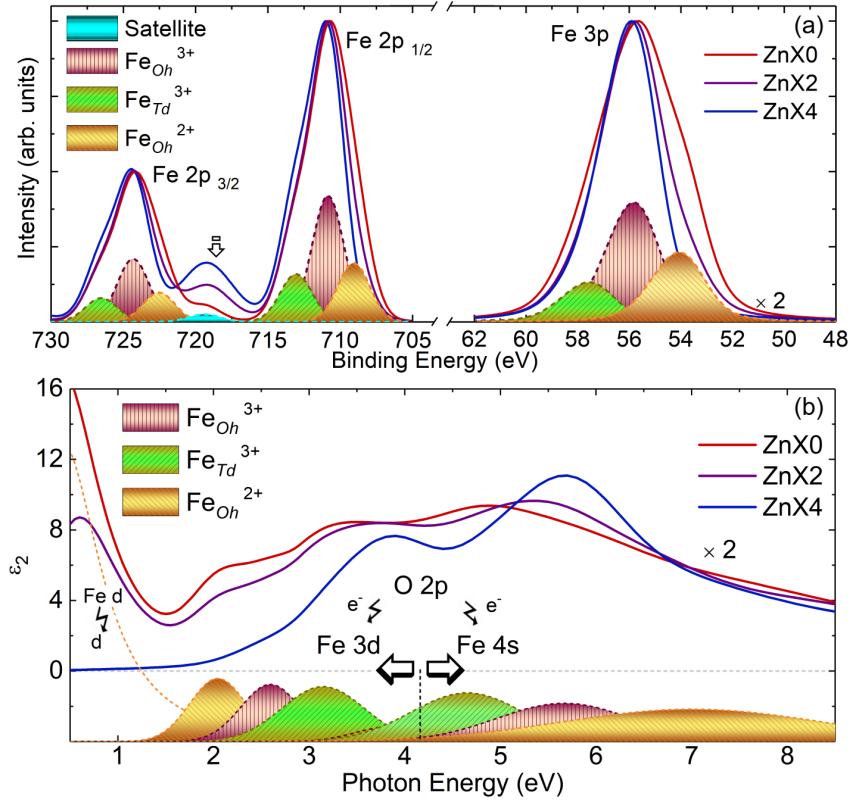


Figure 5.24: (a) Model approximation to the measured surface Fe 2p and 3p XPS core level spectra without the Shirley background and (b) the bulk MDF for ZnX0, ZnX2 and ZnX4 thin films. XPS intensity of the resulting fit and ϵ_2 approximation line-shapes are multiplied by a factor of two for clarity. The individual Fe cation contribution to the modeled spectra for chemical composition determination are indicated by the shaded areas for the ZnX0 film. The satellite contribution between the XPS Fe 2p_{3/2} and 2p_{1/2} core levels is indicated by an arrow.

see inset of Figure 5.25. The relative ratio of trivalent cation concentrations on *Td*- to *Oh*-sites decreases at a monotonic rate from 1.64 to 0.15 with the increase in Zn content from 0 to 1.26. The relative bulk and surface cation composition values for individual films of each Zn concentration are listed in Table 5.3. In contrast to the near-surface film region, the bulk chemical composition was found to contain an abundance (deficiency) of Fe_{*Td*}³⁺ (Fe_{*Oh*}³⁺) cations.

Relative divalent cation content in the near-surface region as a function of that in the bulk shows a nearly linear relationship with a plateau for the intermediate Zn concentration values, Figure 5.25. The deviation from linearity indicates a lack of monotonous distribution of Zn_{*Td*}²⁺ and Fe_{*Oh*}²⁺ cations throughout the film. Cation incorporation into the film structure is further illustrated by the relative

5.5. Cation configuration in dependence on the Zn concentration

Table 5.3: Relative bulk and surface cation composition, estimated from MDF and XPS spectra approximations, respectively. The values are percentages, depicted schematically in Figure 5.29(a). The corresponding uncertainties, determined from parametrization of the numerical MDF line-shape as well as considering cation contributions to both Fe 2p and 3p core level spectra, are listed in brackets.

EDX Zn (x)	MDF Fe _{Td} ³⁺	MDF Fe _{Oh} ²⁺	MDF Fe _{Oh} ³⁺	XPS Fe _{Td} ³⁺	XPS Fe _{Oh} ²⁺	XPS Fe _{Oh} ³⁺
0	36.9 (3.0)	40.5 (0.6)	22.6 (2.7)	18.9 (2.8)	27.9 (3.0)	53.2 (0.6)
0.26	36.9 (5.7)	34.2 (1.0)	28.9 (4.5)	19.7 (5.4)	14.6 (3.5)	65.6 (0.6)
0.56	38.0 (5.8)	26.3 (1.7)	35.7 (6.0)	17.8 (4.5)	14.1 (3.2)	68.1 (2.3)
0.87	27.8 (6.0)	18.2 (3.4)	54.0 (6.1)	15.0 (2.6)	17.4 (3.5)	67.6 (3.7)
1.26	12.9 (5.8)	0	87.1 (5.6)	21.1 (3.1)	0	78.9 (4.3)

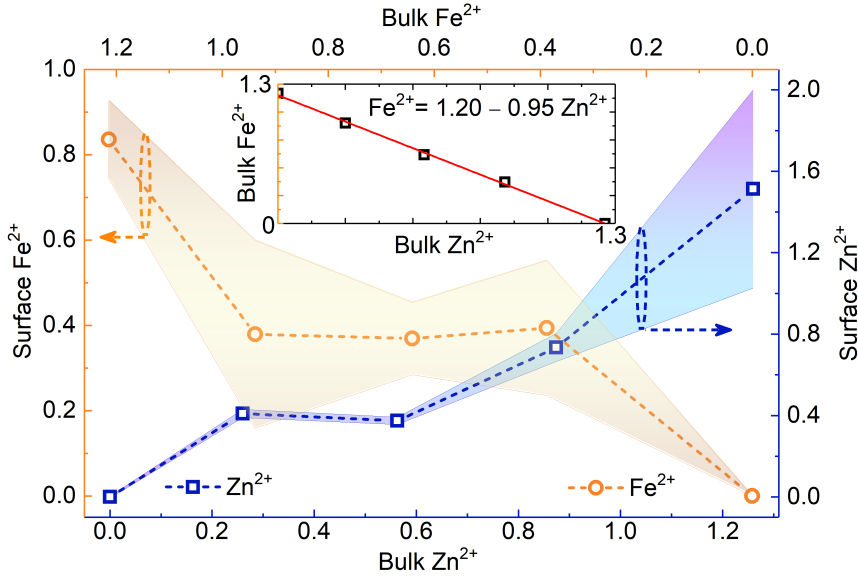


Figure 5.25: Relative surface concentration of Fe²⁺ and Zn²⁺ cations as a function of the bulk cation concentration. The inset shows bulk Fe_{Oh}²⁺ (from MDF) as a function of bulk Zn²⁺ (from EDX) with a linear function approximation. The errors are indicated by the shaded regions.

surface to bulk cation ratios, Figure 5.26. Evidently, Fe²⁺ is likely to be found in the bulk, rather than the near-surface region, with a nearly uniform distribution in the ZnX₃ film with x = 0.87. The octahedral and tetrahedral Fe³⁺ preferentially occupy the surface and bulk film regions, respectively. The surface to bulk cation ratio remains nearly constant as the Zn incorporation increases from x = 0 to 0.56. With further Zn substitution, the octahedral and tetrahedral Fe³⁺ cations tend towards a more even distribution within the film. A nearly homogeneous cation composition in the x = 0.87 film could possibly serve as a pivot Zn concentration, as the predominant structure evolves from an inverse to

5.5. Cation configuration in dependence on the Zn concentration

a normal spinel configuration [66]. At the highest Zn content, the cation distribution is reversed and the octahedral as well as tetrahedral trivalent cations primarily occupy the bulk as well as the surface film regions, respectively. Therefore, cation allocation within the film architecture could be characteristic of the prevailing nature of the spinel configuration. In particular, the bulk (surface) of spinel ferrite film in its predominantly inverse configuration, would be primarily occupied by Fe_{Td}^{3+} (Fe_{Oh}^{3+}), while that of a normal spinel film would be occupied by Fe_{Oh}^{3+} (Fe_{Td}^{3+}).

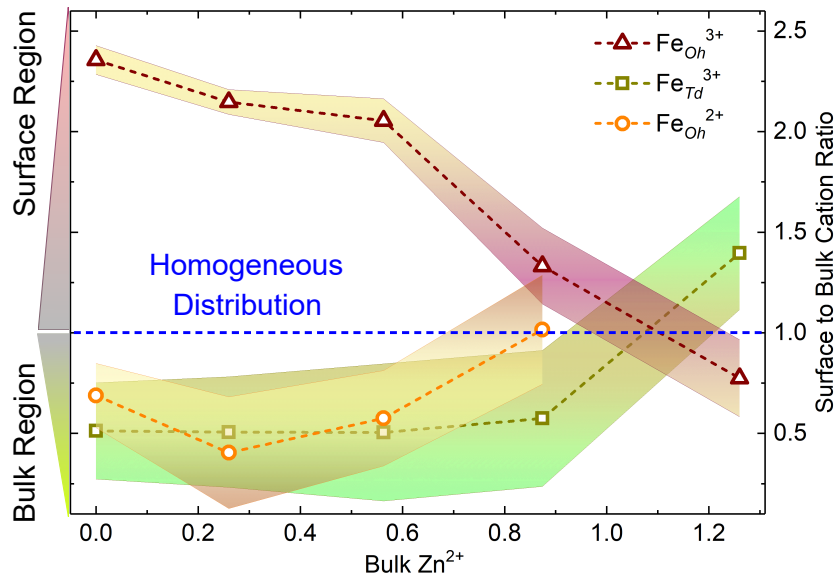


Figure 5.26: Relative surface to bulk cation concentration Fe ratio as a function of Zn^{2+} . The horizontal dashed line represents the ratio value for homogeneous distribution. The errors are indicated by the shaded regions.

5.5. Cation configuration in dependence on the Zn concentration

5.5.3 Magneto-static behavior

Room temperature hysteresis loops are depicted in Figure 5.27(a) and (b), where the diamagnetic contribution from the substrate was subtracted. Interestingly, the ZnX4 film with $x = 1.26$ shows a room temperature hysteresis with negligible coercive field, suggesting an easily reversible system, which is characteristic of nanoparticle formation. Furthermore, magnetization of all samples, measured in the temperature range 50 - 300 K, apart from ZnX0 film with $x = 0$, exhibit a linear behavior at $\mu_0 H \geq 0.1$ T. Previous studies attribute this effect to the canting of spins, where the AF and FM magnetic coupling in the spin chain is no longer parallel, giving rise to the paramagnetic component [31, 86, 197]. Additionally, the interface and the surface regions are known to exhibit magnetic anisotropy, also leading to the absence of saturation magnetization [86, 198]. Therefore, to account for these effects and to estimate saturation magnetization, the following approach is applied for $\mu_0 H \geq 0.1$ T:

$$M(\mu_0 H) = M_S \left[1 - \left(\frac{\alpha}{\mu_0 H} \right) - \left(\frac{\beta}{(\mu_0 H)^2} \right) \right] + \chi_d \mu_0 H \quad (5.2)$$

where M_S is the saturation magnetization and χ_d is the high-field paramagnetic differential susceptibility, due to non-collinear spins in the magnetic structure. The coefficients α and β are related to structural inhomogeneities and magnetic anisotropy, respectively [120]. In the case of homogeneous ferromagnetic layers, the saturation magnetization, as a function of temperature, is expected to follow the Bloch law: $M_S(T) = M_S(0) [1 - (T/T_C)^{3/2}]$, where T_C is the Curie temperature. However, in our case, only the ZnX3 film with $x = 0.87$ follows this relation in the measured temperature range, yielding a Curie temperature of 603.5 K. Saturation magnetization as a function of temperature is depicted in Figure 5.27(c) with a Bloch law approximation for the ZnX3 film. This indicates that the ZnX3 film with $x = 0.87$ is likely comprised of homogeneous ferromagnetic layers consistent with a smooth surface morphology as well as nearly equilibrium cation distribution.

The deviation from the Bloch law as well as the features, visible in the magnetization as a function of temperature, reveal the following nature of our layered structures. First and foremost, a magnetization maximum, of the ZnX0 film with $x = 0$ is observed at 112 K, in close proximity of the known Verwey transition temperature ($T_V = 120$ K) in bulk magnetite, see Section 5.1. Magnetization was measured while warming from 10 to 350 K in an applied field of $\mu_0 H = 0.1$ T after cooling at zero applied magnetic field (ZFC). This transition is also evident by

5.5. Cation configuration in dependence on the Zn concentration

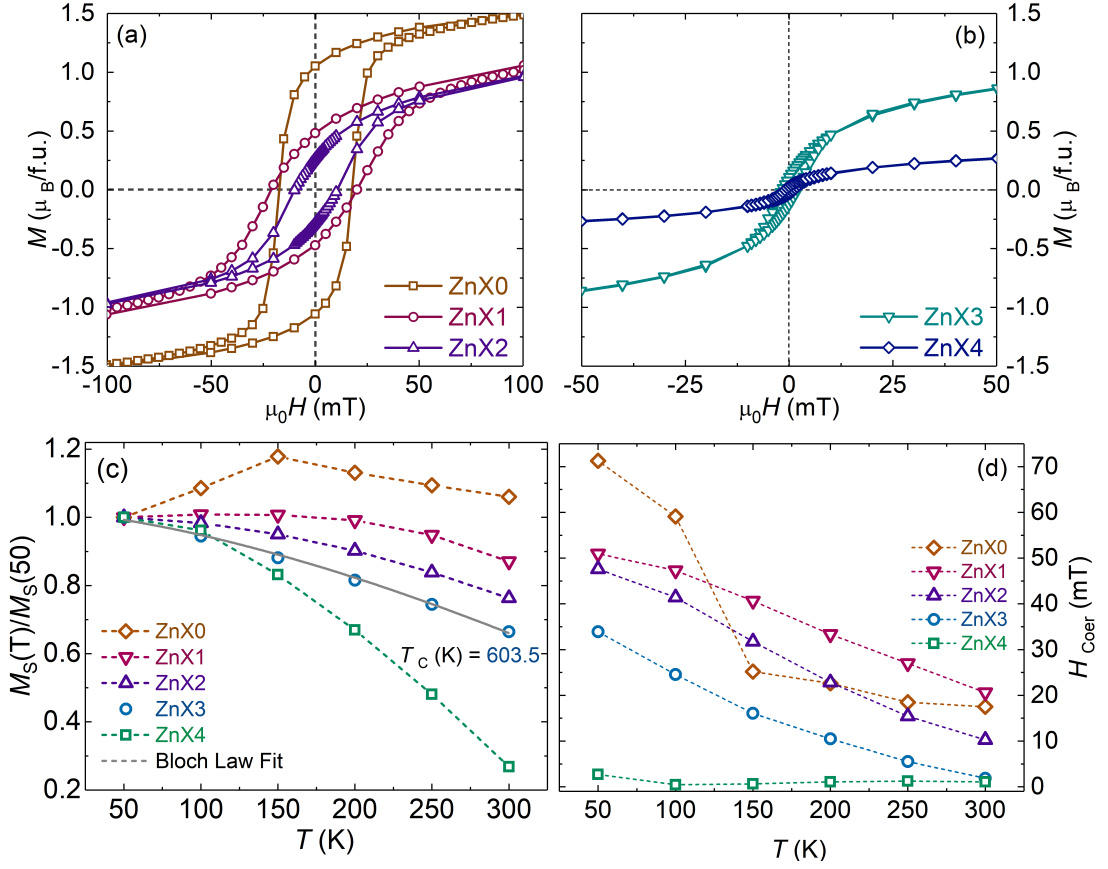


Figure 5.27: Room temperature magnetization as a function of applied magnetic field ($\mu_0 H$) for (a) ZnX0-2 films with $x \leq 0.56$ and (b) ZnX3-4 films with $x \geq 0.87$. (c) Saturation magnetization ($M_S(T)/M_S(50)$) and (d) coercive field ($H_{Coer}(T)$) as a function of temperature. The approximation fit of the Bloch law to $M_S(T)$ is shown for the ZnX3 film with $x = 0.87$ with the resulting Curie temperature as indicated.

the maximum of M_S ($2.21 \mu_B/\text{f.u.}$) and a sharp increase in coercivity field (from 25.2 to 59.1 mT) at and below 150 K, respectively, Figure 5.27(c) and (d). Below the Verwey phase transition temperature, the cations on the octahedral lattice sites are known to assume an ordered state and a sudden decrease in magnetic moment is expected, see Section 2.4. An abrupt magnetization decrease at T_V as well as a constant magnetization value at temperatures below, in the ZFC curve, would be indicative of high quality epitaxial (single crystal) magnetite material [32,42,199]. However, the weak magnetization drop at T_V , accompanied by a nearly monotonous $M(T)$ decrease at temperatures below T_V , likely hints to the presence of more than one magnetic state within the ZnX0 film of $x = 0$, Figure 5.28(a). Interestingly, the Verwey transition becomes less pronounced, evident by a smoother magnetization decrease at the T_V , as the Zn substitution

5.5. Cation configuration in dependence on the Zn concentration

increases from 0 to 0.56. Below the T_V , the increase in magnetization with increase in temperature is nearly monotonous, but exhibits different behavior with the increase in Zn content, shaded region in Figure 5.28.

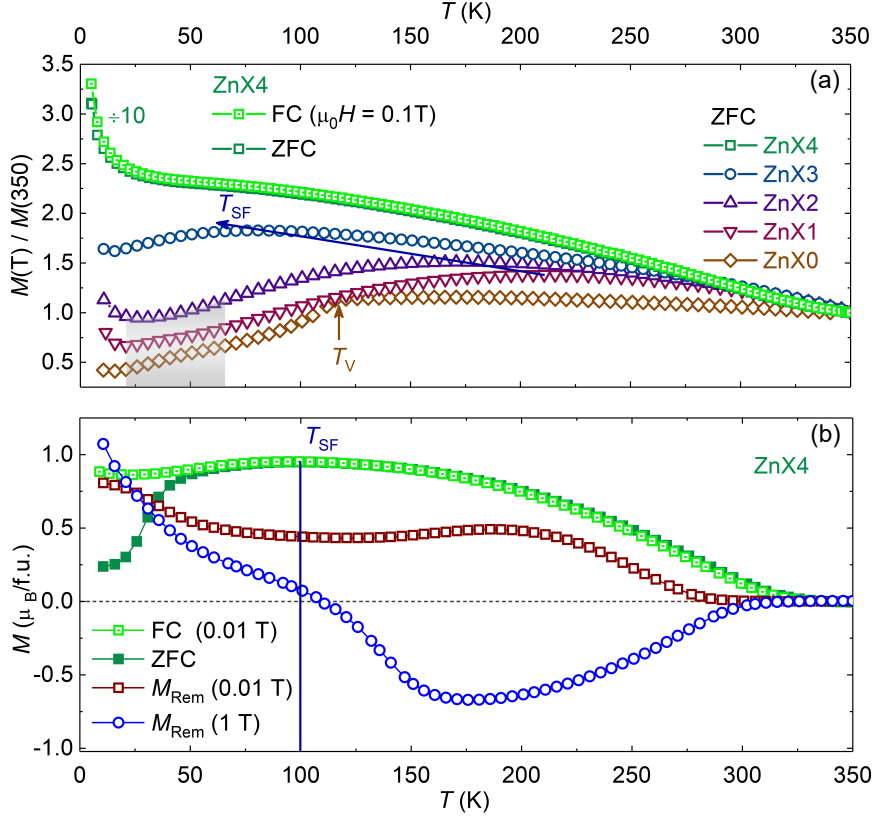


Figure 5.28: (a) Normalized magnetization measured at applied field of $\mu_0 H = 0.1$ T as a function of temperature after ZFC for all samples and after FC for the ZnX4 film with $x = 1.26$. ZFC and FC for the ZnX4 film is divided by a factor of 10 and shifted up by 1 for a clear comparison. T_{SF} and T_V are indicated, see text for more details. The shaded area highlights the low temperature magnetic behavior. (b) ZFC and FC at $\mu_0 H = 0.01$ T as well as remnant magnetization after $\mu_0 H = 0.01$ and 1 T as a function of temperature for the ZnX4 film. T_{SF} is depicted in the graph.

Furthermore, the temperature at which the ZFC ($\mu_0 H = 0.1$ T) magnetization exhibits its maximum value, known as the spin freezing temperature (T_{SF}), becomes visible for the ZnX1 film with $x = 0.26$ and shifts from 210 to 81 K with increase in Zn content from 0.26 to 0.87. The decrease of T_{SF} has been previously attributed to a decline of the degree of cation inversion, thus weakening the $Td-O-Oh$ AF coupling in disordered $ZnFe_2O_4$ thin films [31, 197]. The M_S , at 50 K, T_{SF} and H_{Coer} , at 300 K, are listed in Table 5.4. The magnetic behavior, that is characteristic of both inverse and normal spinel structure, is apparent in

5.5. Cation configuration in dependence on the Zn concentration

the ZnX0-2 films with $x \leq 0.56$. This would suggest a presence of more than one cation configuration and likely indicates a polycrystalline structure with diverse temperature dependent magnetic behavior.

Lastly, the low degree of cation inversion, in the normal zinc ferrite structure, manifests itself by a cusp around 10 K and a T_{SF} of 100 K in the ZFC ($\mu_0 H = 0.01$ T) of the $x = 1.26$ film, Figure 5.28(b) [31]. Furthermore, this film demonstrates a reversible ZFC and field cooled (FC) magnetization at an applied field of $\mu_0 H = 0.1$ T. Interestingly, depending on the strength of the magnetic field, applied prior to measurement, either a positive magnetization with an upward hump (after a weak $\mu_0 H = 0.01$ T) or a negative magnetization with a downward hump (after a strong $\mu_0 H = 1$ T) is observed in $M_{Rem}(T)$. The magnetization reversal can be attributed to a bimodal magnetization state, formed by nanostructure surface and core spins in a structure of high surface to volume ratio [122]. This is due to the evolving balance and changing dominance among anisotropy energy, Zeeman energy and antiferromagnetic coupling energy under different field and temperature conditions [123]. Under an applied magnetic field, which is not strong enough to saturate both the core and surface spins, the anisotropy energy is dominant. In this case, the surface spins can fluctuate along their easy axis and a mutual alignment to the core spins, which are frozen upon removal of the applied field, is sustained. When the applied field is sufficiently large, both core and surface spins align along the applied field and the Zeeman energy is dominant. Upon removal of the strong magnetic field, the antiparallel alignment of the core and surface spins results in a negative total magnetization [122]. The concentration of Fe_{Td}^{3+} , being higher in the film surface than in the bulk, is also consistent with zinc ferrite films grown under low oxygen pressure in previous studies [29, 40, 66]. Additionally, the superparamagnetic behavior at room temperature, as well as a low T_C , would support the presence of a large number of magnetic nanostructures with a low degree of cation disorder. This assumption is consistent with the substrate step-and-terrace surface morphology, retained by the interface of the ZnX4 film with $x = 1.26$, as well as higher Fe_{Td}^{3+} cation concentration in the surface than in the bulk.

5.5. Cation configuration in dependence on the Zn concentration

Table 5.4: Film thickness (d_{TF}) with the maximum error of 3 nm, determined from the numerical approximation of the dielectric function. Saturation magnetization (M_S) for hysteresis measured at 50 K. Spin freezing temperature (T_{SF}) was measured during warming with applied field of $\mu_0 H = 0.1$ T after ZFC. Coercive field was measured at room temperature.

EDX Zn (x)	d_{TF} (nm)	M_S at 50 K (μ_B /f.u.)	T_{SF} (K) (ZFC at $\mu_0 H = 0.1$ T)	H_{Coer} (mT) at 300 K
0	61	1.88	165.7	175
0.26	45	1.81	210.8	206
0.56	41	1.98	170.8	103
0.87	40	2.23	80.8	19
1.26	35	1.87	–	11

5.5.4 Section summary and discussion

We finally relate room temperature saturation (M_S) and remnant (M_{Rem}) magnetization to Zn concentration and relative bulk Fe_{Td}^{3+} to Fe_{Oh}^{3+} cation ratio, see Figure 5.29(b). The relative iron cation content in the surface and bulk region is schematically depicted in Figure 5.29(a) and listed in Table 5.3. The experimentally determined M_S value of $2.0 \mu_B$ /f.u. is lower than the value of $2.7 \mu_B$ /f.u., as calculated based on the bulk cation composition of the ZnX0 film with $x = 0$. Interestingly, a value of $3.2 \mu_B$ /f.u. has been reported for a film of similar growth conditions, but with a significantly lower phase boundary volume concentration, determined from conduction measurements, than in our film [47]. This suggests that the magnetic coupling between the adjacent island structures is superior to the local AF and FM interactions. Additionally, the deficiency of the Fe_{Oh}^{3+} cations in the bulk structure would weaken both the AF and FM magnetic interactions. The resulting magnetic moment would then deviate from the expected equation of a spinel in its equilibrium state [32]:

$$(Zn_x^{2+} Fe^{3+}(5\mu_B)_{1-x})_A (Fe^{3+}(5\mu_B)_{1+x} Fe^{2+}(4\mu_B)_{1-x})_B O_4^{2-} \quad (5.3)$$

As Zn^{2+} content increases to 0.56, both M_S and M_{Rem}/M_S exhibit a decrease. The experimentally determined magnetization values of 1.57 and $1.51 \mu_B$ /f.u. are 59 and 66% of the values anticipated for homogeneous $x = 0.26$ and 0.56 film structures, respectively. Such discrepancy as well as the M_{Rem}/M_S ratio (0.2) values correspond well to those reported for an $x = 0.3$ thin film with a non-uniform cation configuration arrangement [42].

The maximum degree of inversion as well as the critical value between the inverse and normal spinel structure, according to the O’Neil-Navrotsky model [66], is predicted to occur when $x = 0.67$ and the bulk $Fe_{Td}^{3+}/Fe_{Oh}^{3+}$ ratio is roughly equivalent to 0.87. The ZnX3 film with $x = 0.87$, in predominantly normal spinel

5.5. Cation configuration in dependence on the Zn concentration

configuration, exhibits a low M_{Rem}/M_S ratio value of 0.07. However, the comparatively high magnetization value of $1.48 \mu_B/\text{f.u.}$ is likely due to the strong presence of Fe_{Td}^{3+} , roughly half of Fe_{Oh}^{3+} bulk content, in the nearly homogeneous film architecture, see Figure 5.29(a). We would like to note that the aforementioned Equation 5.3 is no longer valid for thin films of normal spinel configuration ($x \geq 0.67$). This could possibly be attributed to the depletion of FM ($\text{Fe}_{Oh}^{2+}\text{-Fe}_{Oh}^{3+}$) double exchange interaction giving rise to oxygen mediated AF ($\text{Fe}_{Td}^{3+}\text{-O-Fe}_{Oh}^{3+}$) or FM ($\text{Fe}_{Oh}^{3+}\text{-O-Fe}_{Oh}^{3+}$) super-exchange interaction, see Section 2.5.

The magnetic moment of $0.5 \mu_B/\text{f.u.}$ is exhibited by the ZnX4 film with $x = 1.26$ of predominantly normal spinel structure. This value is strikingly similar to the magnetization reported for ZnFe_2O_4 nanoparticles and is attributed to the presence of local defects [29]. The magnetic response of this film likely originates from the tetrahedrally coordinated Fe^{3+} cations. The Fe_{Td}^{3+} cations would contribute to the AF interaction between the lattice sites, due to *Case 2* and/or *Case 3* in Section 2.5. The tetrahedral Fe cations are more likely to occupy the film near-surface region, rather than the bulk, consistent with previous reports [29, 37, 40].

In summary, this section reveals the nature of cation crystallization in the layered $\text{Zn}_x\text{Fe}_{3-x}\text{O}_4$ spinel system. A deficiency (abundance) of Fe^{3+} on the octahedral (tetrahedral) sublattice is found in the bulk, as opposed to the near-surface region, of the film with predominantly inverse cation configuration ($x \leq 0.56$). The presence of phase boundaries ($x = 0$ film) as well as inhomogeneous cation architecture ($x \leq 0.56$ films) leads to a weakened ferrimagnetic response at room temperature. The $x = 0.87$ film exhibits a nearly uniform cation distribution, consistent with a smooth surface morphology and Bloch law temperature dependence of saturation magnetization. The surface of the $x = 1.26$ film, however, was found to contain a higher concentration of Fe_{Td}^{3+} cations than the bulk. The room temperature superparamagnetic behavior as well as the step-and-terrace surface morphology suggests nanostructure formation, with local defect (Fe_{Td}^{3+}) induced magnetic response.

5.5. Cation configuration in dependence on the Zn concentration

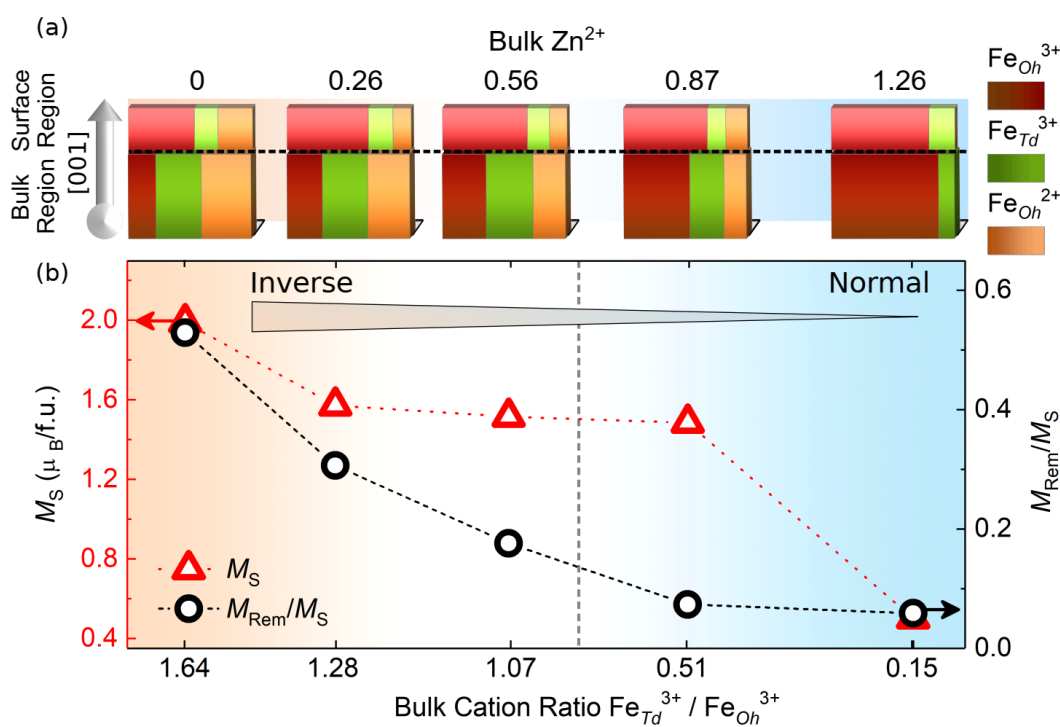


Figure 5.29: (a) Comparative schematic of the relative surface and bulk iron content, estimated from XPS and MDF, respectively. (b) Room temperature saturation magnetization (M_S) and ratio of remnant (M_{Rem}) to M_S as a function of bulk Td - to Oh -site Fe^{3+} cation ratio. The critical value, between the inverse and normal spinel structure according to the O'Neil-Navrotsky model, is depicted by the dashed vertical line.

Chapter 6

Summary and outlook

Remarkable capabilities of iron oxides are realized by the virtue of versatile ion arrangement within the lattice structure which makes them an attractive material for a wide range of applications. ZnFe_2O_4 crystallizes in a normal configuration where the Zn^{2+} and Fe^{3+} cations occupy tetrahedral and octahedral lattice sites, respectively. Although it is considered to be an antiferromagnetic insulator with a Néel temperature of 10 K, spinel-type ZnFe_2O_4 exhibits ferrimagnetic order at room temperature. The underlying mechanism behind this phenomenon was attributed to the presence of local cation disorder and intrinsic defects, but still remains a controversial topic in the condensed matter community. Magnetite (Fe_3O_4), on the other hand, crystallizes in an inverse spinel structure, where the tetrahedral lattice sites are occupied by Fe^{3+} and the octahedral sites by both Fe^{2+} and Fe^{3+} cations. The diminished magnetic response was shown to be due to macroscopic defects, but is yet to be fully understood. Furthermore, determination of the cation distribution remains a technically challenging task, thus limiting our understanding of the magnetic nature in spinel ferrite thin films.

In this work, $\text{Zn}_x\text{Fe}_{3-x}\text{O}_4$ ($0 \leq x \leq 1.26$) thin films were fabricated by pulsed laser deposition and consequently annealed at different temperatures as well as atmospheres. The structural properties were obtained by various methods to examine the crystalline quality. The crystallographic order within the cubic lattice thin film bulk was determined by the means of parametric approximation of the dielectric function in a wide spectral range. Electronic transitions between d orbitals of Fe^{2+} (≤ 1 eV) and transitions from O 2p to 3d and 4s orbitals of Fe and Zn cations (≥ 2 eV) were assigned, based on empirically determined energies of dielectric function approximation. The presence of tetrahedral Fe^{3+} and octahedral Fe^{2+} cations is determined experimentally and serves as evidence of disorder within the normal ZnFe_2O_4 spinel lattice.

6. Summary and outlook

The increase in the amplitude of the approximation function (located at ~ 3.5 eV) is observed in both optical and magneto-optical spectra with the decrease in the substrate temperature during fabrication. The corresponding increase in the ferrimagnetic order of the ZnFe_2O_4 thin films is thereby related to the role of tetrahedral Fe^{3+} in altering the local magnetic interactions. Thermal annealing at temperatures above the deposition temperature results in a decline in the net magnetic moment due to a redistribution in cation order toward a normal spinel configuration. The facilitation of oxygen vacancies enables a significant increase in the magnetic response and is evident in the dielectric function spectra of ZnFe_2O_4 films.

The cation distribution in the thin film near-surface region was estimated from the approximation of Fe 2p and 3p core levels of XPS spectra. A deficiency (abundance) of Fe^{3+} of octahedral (tetrahedral) coordination is found in the bulk, as opposed to the near-surface region, of the films with predominantly inverse cation configuration ($x \leq 0.56$), in contrast to those of predominantly normal spinel configuration. The inhomogeneous cation configuration distribution in spinels of inverse structure likely leads to a weak magnetic response. In films of normal spinel structure, however, the likely presence of tetrahedral Fe^{3+} cations in the surface region could be responsible for the observed ferrimagnetic order. Therefore, spectroscopically determined defect rich cation configuration distribution underlines the role of intrinsic and macroscopic defects in spinel ferrite thin films.

This work sheds light on the prevailing nature behind the magnetic response of the spinel ferrite thin films. The discussed results would serve as a reasonable starting point for theoretical electronic structure calculations. The presented description of the diagonal dielectric tensor elements allows an approximation of the bulk crystallographic structure in ferrite oxide thin films. Based on our approach, the presence of valence- and site-specific Fe cation concentration in ferrite systems can be estimated by using spectroscopic ellipsometry. The application of this technique to other spinel ferrites of normal configuration could lead to similar discoveries. Further work on improving the model approximation parameters is essential for a more accurate description of the dielectric function. The presence of local defects is spectroscopically evident and manipulated in order to promote and alter the magnetic behavior. Whether the magnetic response is improved or diminished, depends strongly on the distribution of the local configuration within the film, in response to fabrication or treatment procedure. Therefore, a wider choice of deposition and modification parameters as well as complemen-

tary methods such as XMCD and XAS could yield constructive validation of the observed effects. The determined nature behind the macroscopic structure formation provides a deeper insight into the volatile structure-property relationship, which should facilitate further investigation of magnetic semiconductors from a different perspective and pave way to their use in a wider scope of technological applications.

Bibliography

- [1] R. M. CORNELL AND U. SCHWERTMANN, *The Iron Oxides: Structure, Properties, Reactions, Occurrences and Uses*, Wiley-VCH Verlag GmbH & Co. KGaA, Weinheim, 2nd ed., (2003).
- [2] P. BERTELSEN, W. GOETZ, M. B. MADSEN, K. M. KINCH, S. F. HVIID, J. M. KNUDSEN, H. P. GUNNLAUGSSON, J. MERRISON, P. NØRNBERG, S. W. SQUYRES, J. F. BELL, K. E. HERKENHOFF, S. GOREVAN, A. S. YEN, T. MYRICK, G. KLINGELHÖFER, R. RIEDER, AND R. GELLERT, *Magnetic properties experiments on the mars exploration rover spirit at gusev crater*, *Science*, **305**, 5685 (2004).
- [3] J. L. KIRSCHVINK, A. KOBAYASHI-KIRSCHVINK, AND B. J. WOODFORD, *Magnetite biomineralization in the human brain*, *Proc. Natl. Acad. Sci. U.S.A.*, **89**, 16 (1992).
- [4] D. A. KISHKINEV AND N. S. CHERNETSOV, *Magnetoreception systems in birds: a review of current research*, *Zh. Obshch. Biol.*, **75**, 2 (2014).
- [5] S. A. GILDER, M. WACK, L. KAUB, S. C. ROUD, N. PETERSEN, H. HEINSEN, P. HILLENBRAND, S. MILZ, AND C. SCHMITZ, *Distribution of magnetic remanence carriers in the human brain*, *Sci. Rep.*, **8**, 1 (2018).
- [6] E. J. VERWEY, *Electronic conduction of magnetite (Fe_3O_4) and its transition point at low temperatures*, *Nature*, **144**, 3642 (1939).
- [7] L. NÉEL, *Antiferromagnetism and ferrimagnetism*, *Proc. Phys. Soc. A*, **65**, 11 (1952).
- [8] G. S. PARKINSON, *Iron oxide surfaces*, *Surf. Sci. Rep.*, **71**, 1 (2016).
- [9] P. TARTAJ, M. P. MORALES, T. GONZALEZ-CARREÑO, S. VEINTEMILLAS-VERDAGUER, AND C. J. SERNA, *The iron ox-*

BIBLIOGRAPHY

- ides strike back: From biomedical applications to energy storage devices and photoelectrochemical water splitting*, *Adv. Mater.*, **23**, 44 (2011).
- [10] N. GUIJARRO, P. BORNOZ, M. S. PRÉVOT, X. YU, X. ZHU, M. JOHNSON, X. A. JEANBOURQUIN, F. LE FORMAL, AND K. SIVULA, *Evaluating spinel ferrites MFe_2O_4 ($M = Cu, Mg, Zn$) as photoanodes for solar water oxidation: prospects and limitations*, *Sustainable Energy Fuels*, **2**, 1 (2018).
- [11] F. F. ABDI AND S. P. BERGLUND, *Recent developments in complex metal oxide photoelectrodes*, *J. Phys. D*, **50**, 19 (2017).
- [12] S. CHU, W. LI, Y. YAN, T. HAMANN, I. SHIH, D. WANG, AND Z. MI, *Roadmap on solar water splitting: current status and future prospects*, *Nano Futures*, **1**, 2 (2017).
- [13] A. VARZI, D. BRESSER, J. VON ZAMORY, F. MÜLLER, AND S. PASSERINI, *$ZnFe_2O_4$ -C/ $LiFePO_4$ -CNT: A novel high-power lithium-ion battery with excellent cycling performance*, *Adv. Energy Mater.*, **4**, 10 (2014).
- [14] R. ZHANG, X. YANG, D. ZHANG, H. QIU, Q. FU, H. NA, Z. GUO, F. DU, G. CHEN, AND Y. WEI, *Water soluble styrene butadiene rubber and sodium carboxyl methyl cellulose binder for $ZnFe_2O_4$ anode electrodes in lithium ion batteries*, *J. of Power Sources*, **285**, 227 (2015).
- [15] G. WEI, L. WEI, D. WANG, Y. CHEN, Y. TIAN, S. YAN, L. MEI, AND J. JIAO, *Reversible control of the magnetization of spinel ferrites based electrodes by lithium-ion migration*, *Sci. Rep.*, **7**, 1 (2017).
- [16] T. YANG, W. ZHANG, L. LI, B. JIN, E. JIN, S. JEONG, AND Q. JIANG, *In-situ synthesized $ZnFe_2O_4$ firmly anchored to the surface of MWCNTs as a long-life anode material with high lithium storage performance*, *Appl. Surf. Sci.*, **425**, 978 (2017).
- [17] D. YOO, J. H. LEE, T. H. SHIN, AND J. CHEON, *Theranostic magnetic nanoparticles*, *Acc. of Chem. Res.*, **44**, 10 (2011).
- [18] J. H. LEE, J. W. KIM, AND J. CHEON, *Magnetic nanoparticles for multi-imaging and drug delivery*, *Mol. Cells*, **35**, 4 (2013).
- [19] A. MEIDANCHI, O. AKHAVAN, S. KHOEI, A. A. SHOKRI, Z. HAJIKARIMI, AND N. KHANSARI, *$ZnFe_2O_4$ nanoparticles as radiosensitizers*

- in radiotherapy of human prostate cancer cells*, Mater. Sci. Eng. C, **46**, 394 (2015).
- [20] E. A. PÉRIGO, G. HEMERY, O. SANDRE, D. ORTEGA, E. GARAIO, F. PLAZAOLA, AND F. J. TERAN, *Fundamentals and advances in magnetic hyperthermia*, Appl. Phys. Rev., **2**, 4 (2015).
- [21] V. J. SAWANT, S. R. BAMANE, R. V. SHEJWAL, AND S. B. PATIL, *Comparison of drug delivery potentials of surface functionalized cobalt and zinc ferrite nanohybrids for curcumin in to MCF-7 breast cancer cells*, J. Magn. Magn. Mater., **417**, 222 (2016).
- [22] J. J. VERSLUIJS, M. A. BARI, AND J. M. D. COEY, *Magnetoresistance of half-metallic oxide nanocontacts*, Phys. Rev. Lett., **87**, 026601 (2001).
- [23] D. J. HUANG, C. F. CHANG, J. CHEN, L. H. TJENG, A. D. RATA, W. P. WU, S. C. CHUNG, H. J. LIN, T. HIBMA, AND C. T. CHEN, *Spin-resolved photoemission studies of epitaxial Fe_3O_4 (1 0 0) thin films*, J. Magn. Magn. Mater., **239**, 1 (2002).
- [24] U. LÜDERS, A. BARTHÉLÉMY, M. BIBES, K. BOUZEHOANE, S. FUSIL, E. JACQUET, J. P. CONTOUR, J. F. BOBO, J. FONTCUBERTA, AND A. FERT, *$NiFe_2O_4$: A versatile spinel material brings new opportunities for spintronics*, Adv. Mater., **18**, 13 (2006).
- [25] D. S. MATHEW AND R. S. JUANG, *An overview of the structure and magnetism of spinel ferrite nanoparticles and their synthesis in microemulsions*, Chem. Eng. J., **129**, 1 (2007).
- [26] J. B. MOUSSY, *From epitaxial growth of ferrite thin films to spin-polarized tunnelling*, J. Phys. D, **46**, 14 (2013).
- [27] A. HIROHATA AND K. TAKANASHI, *Future perspectives for spintronic devices*, J. Phys. D, **47**, 19 (2014).
- [28] K. E. SICKAFUS AND J. M. WILLS, *Structure of Spinel*, J. Am. Ceram. Soc., **82**, 12 (2004).
- [29] C. E. RODRÍGUEZ TORRES, F. GOLMAR, M. ZIESE, P. ESQUINAZI, AND S. P. HELUANI, *Evidence of defect-induced ferromagnetism in $ZnFe_2O_4$ thin films*, Phys. Rev. B, **84**, 6 (2011).

BIBLIOGRAPHY

- [30] V. ZVIAGIN, Y. KUMAR, I. LORITE, P. ESQUINAZI, M. GRUNDMANN, AND R. SCHMIDT-GRUND, *Ellipsometric investigation of $ZnFe_2O_4$ thin films in relation to magnetic properties*, Appl. Phys. Lett., **108**, 13 (2016).
- [31] S. NAKASHIMA, K. FUJITA, K. TANAKA, K. HIRAO, T. YAMAMOTO, AND I. TANAKA, *First-principles XANES simulations of spinel zinc ferrite with a disordered cation distribution*, Phys. Rev. B, **75**, 17 (2007).
- [32] J. TAKAOBUSHI, M. ISHIKAWA, S. UEDA, E. IKENAGA, J. J. KIM, M. KOBATA, Y. TAKEDA, Y. SAITOH, M. YABASHI, Y. NISHINO, D. MIWA, K. TAMASAKU, T. ISHIKAWA, I. SATOH, H. TANAKA, K. KOBAYASHI, AND T. KAWAI, *Electronic structures of $Fe_{3-x}M_xO_4$ ($M=Mn, Zn$) spinel oxide thin films investigated by x-ray photoemission spectroscopy and x-ray magnetic circular dichroism*, Phys. Rev. B, **76**, 205108 (2007).
- [33] J. H. SHIM, S. LEE, J. H. PARK, S.-J. HAN, Y. H. JEONG, AND Y. W. CHO, *Coexistence of ferrimagnetic and antiferromagnetic ordering in Fe-inverted zinc ferrite investigated by NMR*, Phys. Rev. B, **73**, 064404 (2006).
- [34] Y. KUMAR, I. LORITE, M. LORENZ, P. ESQUINAZI, AND M. GRUNDMANN, *Effect of annealing on the magnetic properties of zinc ferrite thin films*, Mater. Lett., **195**, 89 (2017).
- [35] C. E. RODRÍGUEZ TORRES, G. A. PASQUEVICH, P. M. ZÉLIS, F. GOLMAR, S. P. HELUANI, S. K. NAYAK, W. A. ADEAGBO, W. HERGERT, M. HOFFMANN, A. ERNST, P. ESQUINAZI, AND S. J. STEWART, *Oxygen-vacancy-induced local ferromagnetism as a driving mechanism in enhancing the magnetic response of ferrites*, Phys. Rev. B, **89**, 10 (2014).
- [36] K. KAMAZAWA, Y. TSUNODA, K. ODAKA, AND K. KOHN, *Spin liquid state in $ZnFe_2O_4$* , J. Phys. Chem. Solids, **60**, 1261 (1999).
- [37] K. L. SALCEDO RODRÍGUEZ, M. HOFFMANN, F. GOLMAR, G. PASQUEVICH, P. WERNER, W. HERGERT, AND C. E. RODRÍGUEZ TORRES, *Producing $ZnFe_2O_4$ thin films from ZnO/FeO multilayers*, Appl. Surf. Sci., **393**, 256 (2017).
- [38] K. KAMAZAWA, Y. TSUNODA, H. KADOWAKI, AND K. KOHN, *Magnetic neutron scattering measurements on a single crystal of frustrated $ZnFe_2O_4$* , Phys. Rev. B, **68**, 024412 (2003).

-
- [39] K. L. SALCEDO RODRIGUEZ, F. GOLMAR, AND C. E. RODRIGUEZ TORRES, *Magnetic properties of Zn-ferrites obtained from multilayer film deposited by sputtering*, IEEE Trans. Magn., **49**, 8 (2013).
- [40] S. J. STEWART, S. J. FIGUEROA, J. M. RAMALLO LÓPEZ, S. G. MARCHETTI, J. F. BENGOA, R. J. PRADO, AND F. G. REQUEJO, *Cationic exchange in nanosized $ZnFe_2O_4$ spinel revealed by experimental and simulated near-edge absorption structure*, Phys. Rev. B, **75**, 7 (2007).
- [41] P. MENDOZA ZÉLIS, G. A. PASQUEVICH, K. L. SALCEDO RODRÍGUEZ, F. H. SÁNCHEZ, AND C. E. RODRÍGUEZ TORRES, *Surface magnetic contribution in zinc ferrite thin films studied by element- and site-specific XMCD hysteresis-loops*, J. Magn. Magn. Mater., **419**, 98 (2016).
- [42] N. JEDRECY, C. HEBERT, J. PERRIERE, M. NISTOR, AND E. MILLON, *Magnetic and magnetotransport properties of $Zn_xFe_{3-x}O_{4-y}$ thin films*, Journal of Applied Physics, **116**, 213903 (2014).
- [43] E. GOERING, *Large hidden orbital moments in magnetite*, Phys. Status Solidi B, **248**, 2345 (2011).
- [44] D. GILKS, Z. NEDELKOSKI, L. LARI, B. KUERBANJIANG, K. MATSUZAKI, T. SUSAKI, D. KEPAPTSOGLU, Q. RAMASSE, R. EVANS, K. MCKENNA, AND V. K. LAZAROV, *Atomic and electronic structure of twin growth defects in magnetite*, Sci. Rep., **6**, 20943 (2016).
- [45] K. P. MCKENNA, F. HOFER, D. GILKS, V. K. LAZAROV, C. CHEN, Z. WANG, AND Y. IKUHARA, *Atomic-scale structure and properties of highly stable antiphase boundary defects in Fe_3O_4* , Nat. Commun., **5**, 5740 (2014).
- [46] W. EERENSTEIN, T. T. PALSTRA, T. HIBMA, AND S. CELOTTO, *Origin of the increased resistivity in epitaxial Fe_3O_4 films*, Phys. Rev. B, **66**, 20 (2002).
- [47] D. VENKATESHVARAN, M. ALTHAMMER, A. NIELSEN, S. GEPRÄGS, M. S. RAMACHANDRA RAO, S. T. GOENNENWEIN, M. OPEL, AND R. GROSS, *Epitaxial $Zn_xFe_{3-x}O_4$ thin films: A spintronic material with tunable electrical and magnetic properties*, Phys. Rev. B, **79**, 13 (2009).

BIBLIOGRAPHY

- [48] T. BÖNTGEN, K. BRACHWITZ, R. SCHMIDT-GRUND, M. LORENZ, AND M. GRUNDMANN, *Vacuum ultraviolet dielectric function of $ZnFe_2O_4$ thin films*, J. Appl. Phys., **113**, 7 (2013).
- [49] K. BRACHWITZ, T. BÖNTGEN, M. LORENZ, AND M. GRUNDMANN, *On the transition point of thermally activated conduction of spinel-type MFe_2O_4 ferrite thin films ($M = Zn, Co, Ni$)*, Appl. Phys. Lett., **102**, 17 (2013).
- [50] M. WELKE, K. BRACHWITZ, M. LORENZ, M. GRUNDMANN, K.-M. SCHINDLER, A. CHASSÉ, AND R. DENECKE, *Structure and cation distribution of $(Mn_{0.5}Zn_{0.5}Fe_2O_4)$ thin films on $SrTiO_3$ (001)*, J. Appl. Phys., **121**, 225305 (2017).
- [51] M. BONHOLZER, M. LORENZ, AND M. GRUNDMANN, *Layer-by-layer growth of TiN by pulsed laser deposition on in-situ annealed (100) MgO substrates*, Phys. Status Solidi A, **211**, 11 (2014).
- [52] M. LORENZ, M. BRANDT, K. MEXNER, K. BRACHWITZ, M. ZIESE, P. ESQUINAZI, H. HOCHMUTH, AND M. GRUNDMANN, *Ferrimagnetic $ZnFe_2O_4$ thin films on $SrTiO_3$ single crystals with highly tunable electrical conductivity*, Phys. Status Solidi - RRL, **5**, 12 (2011).
- [53] K. PERSSON, *Materials Data on Fe_3O_4 (SG:227) by Materials Project*, (2015), <https://doi.org/10.17188/1194194>. Data set, LBNL Materials Project; Lawrence Berkeley National Laboratory, Berkeley, California.
- [54] K. MOMMA AND F. IZUMI, *VESTA3 for three-dimensional visualization of crystal, volumetric and morphology data*, J. of Appl. Crystallogr., **44**, 6 (2011).
- [55] S. POPINET, *Inkscape*. Copyright © Free Software Foundation, Inc., Boston, Massachusetts, (2018).
- [56] W. BRAGG, *XXX. The structure of the spinel group of crystals*, Lond. Edinb. Dubl. Phil. Mag., **30**, 176 (1915).
- [57] M. GRUNDMANN, *The Physics of Semiconductors*, Springer International Publishing, Switzerland, 2nd ed., (2010).
- [58] K. E. SICKAFUS AND J. M. WILLS, *Structure of Spinel*, J. Am. Ceram. Soc., **82**, 12 (1999).

- [59] K. BRACHWITZ, *Defekt-induzierte Leitungsmechanismen und magnetische Eigenschaften spinellartiger Ferrite*, PhD thesis, Universität Leipzig, (2014).
- [60] J. D. DUNITZ AND L. E. ORGEL, *Electronic properties of transition-metal oxides-II. Cation distribution amongst octahedral and tetrahedral sites*, J. Phys. Chem. Solids, **3**, 3 (1957).
- [61] C. JANIAK, T. KLAPÖTKE, H.-J. MEYER, AND R. ALSFASSER, *Moderne Anorganische Chemie*, Berlin, Boston: De Gruyter, 3rd ed., (2007).
- [62] Z. SZOTEK, W. M. TEMMERMAN, D. KÖDDERITZSCH, A. SVANE, L. PETIT, AND H. WINTER, *Electronic structures of normal and inverse spinel ferrites from first principles*, Phys. Rev. B, **74**, 17 (2006).
- [63] S. KUTOLIN, V. P. TISHCHENKO, V. I. KOTYUKOV, AND N. L. KOTLEVSKAYA, *Computer modeling of disordering in spinels as a function of their components electronic structures*, Inorg. Mater., **23**, 268 (1987).
- [64] V. STEVANOVIĆ, M. D’AVEZAC, AND A. ZUNGER, *Simple point-ion electrostatic model explains the cation distribution in spinel oxides*, Phys. Rev. Lett., **105**, 7 (2010).
- [65] X. ZHANG AND A. ZUNGER, *Diagrammatic separation of different crystal structures of A_2BX_4 compounds without energy minimization: A pseudopotential orbital radii approach*, Adv. Funct. Mater., **20**, 12 (2010).
- [66] H. S. C. O’NEILL AND A. NAVROTSKY, *Cation Distributions and Thermodynamic Properties of Binary Spinel Solid Solutions*, Am. Mineral., **69**, 6-8 (1984).
- [67] V. STEVANOVIĆ, M. D’AVEZAC, AND A. ZUNGER, *Universal electrostatic origin of cation ordering in A_2BO_4 spinel oxides*, J. Am. Chem. Soc., **133**, 30 (2011).
- [68] A. YANASE AND N. HAMADA, *Electronic Structure in High Temperature Phase of Fe_3O_4* , J. Phys. Soc. Jpn., **68**, 1607 (1999).
- [69] A. YANASE AND K. SIRATORI, *Band Structure in the High Temperature Phase of Fe_3O_4* , J. Phys. Soc. Jpn., **53**, 312 (1984).

BIBLIOGRAPHY

- [70] M. FONIN, Y. S. DEDKOV, R. PENTCHEVA, U. RÜDIGER, AND G. GÜNTHERODT, *Magnetite: A search for the half-metallic state*, J. Phys. Condens. Matter, **19**, 31 (2007).
- [71] H.-T. JENG, G. Y. GUO, AND D. J. HUANG, *Charge-orbital ordering in low-temperature structures of magnetite: GGA + U investigations*, Phys. Rev. B, **74**, 19 (2006).
- [72] C. H. PATTERSON, *Hybrid DFT calculation of ^{57}Fe NMR resonances and orbital order in magnetite*, Phys. Rev. B, **90**, 075134 (2014).
- [73] D. FRITSCH, *Electronic and optical properties of spinel zinc ferrite: Ab initio hybrid functional calculations*, J. Phys. Condens. Matter, **30**, 9 (2018).
- [74] D. J. SINGH, M. GUPTA, AND R. GUPTA, *Density-functional description of spinel ZnFe_2O_4* , Phys. Rev. B, **63**, 205102 (2001).
- [75] S. SOLIMAN, A. ELFALAKY, G. H. FECHER, AND C. FELSER, *Electronic structure calculations for ZnFe_2O_4* , Phys. Rev. B, **83**, 8 (2011).
- [76] V. ZIAEI AND T. BREDOW, *Ab-initio optical properties and dielectric response of open-shell spinel zinc ferrite*, Eur. Phys. J. B, **90**, 2 (2017).
- [77] G. S. PARKS AND K. K. KELLEY, *The heat capacities of some metallic oxides*, J. Phys. Chem., **30**, 30(1) (1925).
- [78] W. C. HAMILTON, *Neutron Diffraction Investigation of the 119°K Transition in Magnetite*, Phys. Rev., **110**, 1050 (1958).
- [79] M. IIZUMI, T. F. KOETZLE, G. SHIRANE, S. CHIKAZUMI, M. MATSUI, AND S. TODO, *Structure of magnetite (Fe_3O_4) below the Verwey transition temperature*, Acta Cryst., **B38**, 2121 (1982).
- [80] W. HAUBENREISSER, *Zur Theorie der Elektronenleitung im stöchiometrischen Fe_3O_4 -Kristall (Magnetit) oberhalb des Übergangspunktes $T_{\ddot{u}} = 119,4^\circ\text{K}$* , Phys. Status Solidi B, **1**, 6 (1961).
- [81] J. R. CULLEN AND E. CALLEN, *Collective electron theory of the metal-semiconductor transition in magnetite*, J. Appl. Phys., **41**, 879 (1970).
- [82] D. IHLE AND B. LORENZ, *Small-polaron band versus hopping conduction in Fe_3O_4* , J. Phys. Condens. Matter, **18**, 21 (1985).

- [83] F. WALZ, *The verwey transition - a topical review*, J. Phys. Condens. Matter., **14**, 12 (2002).
- [84] J. GARCÍA AND G. SUBÍAS, *The Verwey transition - A new perspective*, J. Phys. Condens. Matter., **16**, 7 (2004).
- [85] M. S. SENN, I. LOA, J. P. WRIGHT, AND J. P. ATTFIELD, *Electronic orders in the verwey structure of magnetite*, Phys. Rev. B, **85**, 125119 (2012).
- [86] Y. YAFET AND C. KITTEL, *Antiferromagnetic arrangements in ferrites*, Phys. Rev., **87**, 290 (1952).
- [87] R. TOPKAYA, A. BAYKAL, AND A. DEMIR, *Yafet-Kittel-type magnetic order in Zn-substituted cobalt ferrite nanoparticles with uniaxial anisotropy*, J. Nanoparticle Res.h, **15**, 1 (2013).
- [88] M. UHL AND B. SIBERCHICOT, *A first-principles study of exchange integrals in magnetite*, J. Phys. Condens. Matter, **7**, 22 (1995).
- [89] P. WANG, Z. KAKOL, M. WITTENAUER, AND J. M. HONIG, *Electrical properties of zinc ferrites $Fe_{3-x}Zn_xO_4$ with $0 \leq x < 0.3$* , Phys. Rev. B, **42**, 7 (1990).
- [90] J. TAKAOBUSHI, H. TANAKA, T. KAWAI, S. UEDA, J. J. KIM, M. KOBATA, E. IKENAGA, M. YABASHI, K. KOBAYASHI, Y. NISHINO, D. MIWA, K. TAMASAKU, AND T. ISHIKAWA, *$Fe_{3-x}Zn_xO_4$ thin film as tunable high Curie temperature ferromagnetic semiconductor*, Appl. Phys. Lett., **89**, 24 (2006).
- [91] K. BRACHWITZ, T. BÖNTGEN, M. LORENZ, AND M. GRUNDMANN, *On the transition point of thermally activated conduction of spinel-type MFe_2O_4 ferrite thin films ($M = Zn, Co, Ni$)*, Appl. Phys. Lett., **102**, 17 (2013).
- [92] F.-L. SCHEIN, M. WINTER, T. BÖNTGEN, H. VON WENCKSTERN, AND M. GRUNDMANN, *Highly rectifying p-ZnCo₂O₄/n-ZnO heterojunction diodes*, Appl. Phys. Lett., **104**, 2 (2014).
- [93] H. J. KIM, I. C. SONG, J. H. SIM, H. KIM, D. KIM, Y. E. IHM, AND W. K. CHOO, *Electrical and magnetic properties of spinel-type magnetic semiconductor $ZnCo_2O_4$ grown by reactive magnetron sputtering*, J. of Appl. Phys., **95**, 11 (2004).

BIBLIOGRAPHY

- [94] T. R. PAUDEL, A. ZAKUTAYEV, S. LANY, M. D'AVEZAC, AND A. ZUNGER, *Doping rules and doping prototypes in A_2BO_4 spinel oxides*, *Advanced Functional Materials*, **21**, 23 (2011).
- [95] J. YAO, Y. LI, AND X. ZHU, *First-Principles Study of the Geometric and Electronic Structures of Zinc Ferrite with Vacancy Defect*, *Metall Mater. Trans. A*, **47**, 7 (2016).
- [96] M. OPEL, *Spintronic oxides grown by laser-MBE*, *J. Phys. D*, **45**, 3 (2012).
- [97] L. MARTIN, Y.-H. CHU, AND R. RAMESH, *Advances in the growth and characterization of magnetic, ferroelectric, and multiferroic oxide thin films*, *Mater. Sci. and Eng. R Rep.*, **68**, 4 (2010).
- [98] S. PRUCNAL, Y. BERENCÉN, M. WANG, J. GRENZER, M. VOELSKOW, R. HÜBNER, Y. YAMAMOTO, A. SCHEIT, F. BÄRWOLF, V. ZVIAGIN, R. SCHMIDT-GRUND, M. GRUNDMANN, J. ŽUK, M. TUREK, A. DROŹDZIEL, K. PYSZNIAK, R. KUDRAWIEC, M. P. POLAK, L. REBOHLE, W. SKORUPA, M. HELM, AND S. ZHOU, *Strain and Band-Gap Engineering in Ge-Sn Alloys via P Doping*, *Phys. Rev. Appl.*, **10**, 064055 (2018).
- [99] S. A. CHAMBERS, *Epitaxial growth and properties of thin film oxides*, *Surf. Sci. Rep.*, **39**, 5 (2000).
- [100] S. MAHIEU, P. GHEKIERE, D. DEPLA, AND R. DE GRyse, *Biaxial alignment in sputter deposited thin films*, *Thin Solid Films*, **515**, 4 (2006).
- [101] L. MARTÍN-GARCÍA, R. GARGALLO-CABALLERO, M. MONTI, M. FORSTER, J. F. MARCO, L. ABALLE, AND J. DE LA FIGUERA, *Spin and orbital magnetic moment of reconstructed $\sqrt{2} \times \sqrt{2}$ $R45^\circ$ magnetite (001)*, *Phys. Rev. B*, **91**, 2 (2015).
- [102] S. CELOTTO, W. EERENSTEIN, AND T. HIBMA, *Characterization of anti-phase boundaries in epitaxial magnetite films*, *Eur. Phys. J. B*, **36**, 2 (2003).
- [103] W. EERENSTEIN, T. HIBMA, AND S. CELOTTO, *Mechanism for superparamagnetic behavior in epitaxial Fe_3O_4 films*, *Phys. Rev. B*, **70**, 18 (2004).
- [104] A. M. BATAILLE, L. PONSON, S. GOTA, L. BARBIER, D. BONAMY, M. GAUTIER-SOYER, C. GATEL, AND E. SNOECK, *Characterization of antiphase boundary network in Fe_3O_4 (111) epitaxial thin films: Effect on anomalous magnetic behavior*, *Phys. Rev. B*, **74**, 15 (2006).

-
- [105] C. CHEN, H. LI, T. SEKI, D. YIN, G. SANCHEZ-SANTOLINO, K. INOUE, N. SHIBATA, AND Y. IKUHARA, *Direct determination of atomic structure and magnetic coupling of magnetite twin boundaries*, ACS Nano, **12**, 3 (2018).
- [106] I. BERNAL-VILLAMIL AND S. GALLEGO, *Electronic phase transitions in ultrathin magnetite films*, J. Phys. Condens. Matter, **27**, 29 (2015).
- [107] A. LAK, M. KRAKEN, F. LUDWIG, A. KORNOWSKI, D. EBERBECK, S. SIEVERS, F. J. LITTERST, H. WELLER, AND M. SCHILLING, *Size dependent structural and magnetic properties of FeO-Fe₃O₄ nanoparticles*, Nanoscale, **5**, 24 (2013).
- [108] D. GILKS, L. LARI, K. MATSUZAKI, H. HOSONO, T. SUSAKI, AND V. K. LAZAROV, *Structural study of Fe₃O₄ (111) thin films with bulk like magnetic and magnetotransport behaviour*, J. of Appl. Phys., **115**, 17 (2014).
- [109] J. DE LA FIGUERA, Z. NOVOTNY, M. SETVIN, T. LIU, Z. MAO, G. CHEN, A. T. N'DIAYE, M. SCHMID, U. DIEBOLD, A. K. SCHMID, AND G. S. PARKINSON, *Real-space imaging of the Verwey transition at the (100) surface of magnetite*, Phys. Rev. Bs, **88**, 16 (2013).
- [110] K. JORDAN, A. CAZACU, G. MANAI, S. F. CEBALLOS, S. MURPHY, AND I. V. SHVETS, *Scanning tunneling spectroscopy study of the electronic structure of Fe₃O₄ surfaces*, Phys. Rev. B, **74**, 8 (2006).
- [111] I. BERNAL-VILLAMIL AND S. GALLEGO, *Charge order at magnetite Fe₃O₄ (0 0 1): Surface and Verwey phase transitions*, J. Phys. Condens. Matter, **27**, 1 (2015).
- [112] Z. ŁODZIANA, *Surface verwey transition in magnetite*, Phys. Rev. Lett., **99**, 20 (2007).
- [113] R. BLIEM, J. PAVELEC, O. GAMBA, E. MCDERMOTT, Z. WANG, S. GERHOLD, M. WAGNER, J. OSIECKI, K. SCHULTE, M. SCHMID, P. BLAHA, U. DIEBOLD, AND G. S. PARKINSON, *Adsorption and incorporation of transition metals at the magnetite Fe₃O₄ (001) surface*, Phys. Rev. B, **92**, 7 (2015).
- [114] R. BLIEM, E. MCDERMOTT, P. FERSTL, M. SETVIN, O. GAMBA, J. PAVELEC, M. A. SCHNEIDER, M. SCHMID, U. DIEBOLD, P. BLAHA,

BIBLIOGRAPHY

- L. HAMMER, AND G. S. PARKINSON, *Subsurface cation vacancy stabilization of the magnetite (001) surface*, Science, **346**, 6214 (2014).
- [115] G. S. PARKINSON, Z. NOVOTNÝ, P. JACOBSON, M. SCHMID, AND U. DIEBOLD, *A metastable Fe(A) termination at the Fe₃O₄ (001) surface*, Surf. Sci., **605**, 15 (2011).
- [116] G. S. PARKINSON, T. A. MANZ, Z. NOVOTNÝ, P. T. SPRUNGER, R. L. KURTZ, M. SCHMID, D. S. SHOLL, AND U. DIEBOLD, *Antiphase domain boundaries at the Fe₃O₄ (001) surface*, Phys. Rev. B, **85**, 19 (2012).
- [117] M. ZAJAC, K. FREINDL, T. ŚLEZAK, M. ŚLEZAK, N. SPIRIDIS, D. WILGOCKA-ŚLEZAK, AND J. KORECKI, *Electronic and magnetic properties of ultra-thin epitaxial magnetite films on mgo (001)*, Thin Solid Films, **519**, 16 (2011).
- [118] R. SAI, S. D. KULKARNI, S. S. M. BHAT, N. G. SUNDARAM, N. BHAT, AND S. A. SHIVASHANKAR, *Controlled inversion and surface disorder in zinc ferrite nanocrystallites and their effects on magnetic properties*, RSC Adv., **5**, 14 (2015).
- [119] R. ZAMIRI, S. A. SALEHIZADEH, H. A. AHANGAR, M. SHABANI, A. REBELO, J. SURESH KUMAR, M. J. SOARES, M. A. VALENTE, AND J. M. FERREIRA, *Optical and magnetic properties of ZnO/ZnFe₂O₄ nanocomposite*, Mater. Chem. Phys., **192**, 330 (2017).
- [120] J. Z. JIANG, G. F. GOYA, AND H. R. RECHENBERG, *Magnetic properties of nanostructured CuFe₂O₄*, J. Phys. Condens. Matter, **11**, 4063 (1999).
- [121] C. YAO, Q. ZENG, G. F. GOYA, T. TORRES, J. LIU, H. WU, M. GE, Y. ZENG, Y. WANG, AND J. Z. JIANG, *ZnFe₂O₄ nanocrystals: Synthesis and magnetic properties*, J. Phys. Chem. C, **111**, 12274 (2007).
- [122] S. GU, W. HE, M. ZHANG, T. ZHUANG, Y. JIN, H. ELBIDWEIHY, Y. MAO, J. H. DICKERSON, M. J. WAGNER, E. D. TORRE, AND L. H. BENNETT, *Physical justification for negative remanent magnetization in homogeneous nanoparticles*, Sci. Rep., **4**, 6267 (2014).
- [123] H. KACHKACHI AND H. MAHBOUB, *Surface anisotropy in nanomagnets: Transverse or Néel?*, J. Magn. Magn. Mater., **278**, 334 (2004).

- [124] N.-Y. CHAN, *Study of barium strontium zirconate titanate thin films and their microwave device applications*, PhD thesis, Hong Kong Polytechnic University, (2010).
- [125] K. ELLMER, A. KLEIN, AND B. RECH, *Transparent Conductive Zinc Oxide*, Springer-Verlag Berlin Heidelberg, (2008).
- [126] L. SPIESS, G. TEICHERT, R. SCHWARZER, H. BEHNKEN, AND C. GENZEL, *Moderne Röntgenbeugung*, Vieweg Teubner Verlag, Springer Fachmedien Wiesbaden GmbH, Wiesbaden, (2009).
- [127] M. F. TONEY AND C. THOMPSON, *X-ray reflectivity on perfluoropolyether polymer molecules on amorphous carbon*, J. Chem. Phys., **92**, 6 (1990).
- [128] A. KUMAR, D. K. PANDYA, AND S. CHAUDHARY, *Structural, electronic, and magnetic behavior of two dimensional epitaxial $Fe_3O_4/TiN/Si(100)$ system*, Appl. Phys. Lett., **102**, 15 (2013).
- [129] W. P. GRIFFITH, *Raman Spectroscopy of Minerals*, Mineralogical Society of Great Britain and Ireland, (1974).
- [130] C. KRANERT, *Investigation of wide-bandgap semiconductors by UV Raman spectroscopy: resonance effects and material characterization*, PhD thesis, Universität Leipzig, (2015).
- [131] Z. WANG, D. SCHIFERL, Y. ZHAO, AND H. S. C. O'NEILL, *High pressure Raman spectroscopy of spinel-type ferrite $ZnFe_2O_4$* , J. Phys. Chem. Solids, **64**, 12 (2003).
- [132] Z. WANG, P. LAZOR, S. K. SAXENA, AND G. ARTIOLI, *High-pressure Raman spectroscopic study of spinel ($ZnCr_2O_4$)*, J. Solid State Chem., **165**, 165 (2002).
- [133] *XEI-150 User's Manual*, Copyright © 2011 Park Systems Corporation, version 1.8.0 ed., (2011).
- [134] D. NEČAS AND P. KLAPETEK, *Gwyddion: an open-source software for spm data analysis*, Cent.l Eur. J. Phys., **10**, 1 (2012).
- [135] U. QUERÉTARO AND A. HERRERA-GOMEZ, *The Peak-Shirley Background*, tech. report, Center for Research and Advanced Studies of the National Polytechnic Institute, (2012).

BIBLIOGRAPHY

- [136] R. HESSE, *Unifit for Windows Spectrum Processing, Analysis and Presentation Software for XPS, XAS and AES*, tech. report, Unifit Scientific Software GmbH, Leipzig Germany, (2017).
- [137] R. P. GUPTA AND S. K. SEN, *Calculation of multiplet structure of core p-vacancy levels*, Phys. Rev. B, **12**, 1 (1975).
- [138] N. S. MCINTYRE AND D. G. ZETARUK, *X-ray photoelectron spectroscopic studies of iron oxides*, Anal. Chem., **49**, 1521 (1977).
- [139] T. FUJII, F. M. F. D. GROOT, AND G. A. SAWATZKY, *In situ XPS analysis of various iron oxide films grown by NO₂-assisted molecular-beam epitaxy*, Phys. Rev. B, **59**, 3195 (1999).
- [140] T. AGHAVNIAN, J. B. MOUSSY, D. STANESCU, R. BELKHOUE, N. JEDRECY, H. MAGNAN, P. OHRESSER, M. A. ARRIO, P. SAINCTAVIT, AND A. BARBIER, *Determination of the cation site distribution of the spinel in multiferroic CoFe₂O₄/BaTiO₃ layers by X-ray photoelectron spectroscopy*, J. Electron Spectros. Relat. Phenomena, **202**, 16 (2015).
- [141] H. YUAN, E. LIU, Y. YIN, W. ZHANG, P. K. WONG, J. G. ZHENG, Z. HUANG, H. OU, Y. ZHAI, Q. XU, J. DU, AND H. ZHAI, *Enhancement of magnetic moment in Zn_xFe_{3-x}O₄ thin films with dilute Zn substitution*, Appl. Phys. Lett., **108**, 23 (2016).
- [142] A. P. GROSVENOR, B. A. KOBE, M. C. BIESINGER, AND N. S. MCINTYRE, *Investigation of multiplet splitting of Fe 2p XPS spectra and bonding in iron compounds*, Surf. Interface Anal., **36**, 1564 (2004).
- [143] T. YAMASHITA AND P. HAYES, *Analysis of XPS spectra of Fe²⁺ and Fe³⁺ ions in oxide materials*, Appl. Surf. Sci., **254**, 2441 (2008).
- [144] P. DRUSKA AND U. STEINIKE, *Surface structure of mechanically activated and of mechanothesized zinc ferrite*, J. Solid State Chem., **21**, 13 (1999).
- [145] P. Y. YU AND M. CARDONA, *Fundamentals of Semiconductors: Physics and Materials Properties*, Springer-Verlag Berlin Heidelberg, 4th ed., (2010).
- [146] H. G. TOMPKINS AND E. A. IRENE, *Handbook of Ellipsometry*, William Andrew, Inc., Norwich, New York, (2005).

-
- [147] H. G. TOMPKINS AND W. A. MCGAHAN, *Spectroscopic Ellipsometry and Reflectometry: A User's Guide*, John Wiley and Sons, New York, 1st ed., (1999).
- [148] P. DRUSKA AND U. STEINIKE, *Optical constants of ZnO*, Jpn. J. Appl. Phys., **36**, 6237 (1997).
- [149] R. SCHMIDT-GRUND, T. LÜHMANN, T. BÖNTGEN, H. FRANKE, D. OPPER, M. LORENZ, AND M. GRUNDMANN, *Temperature dependent dielectric function in the near-infrared to vacuum-ultraviolet ultraviolet spectral range of alumina and yttria stabilized zirconia thin films*, J. Appl. Phys., **114**, 22 (2013).
- [150] T. TIWALD, *Guide to Using WVASE32*, J. A. Woollam Co., Inc., Lincoln, Nebraska, Lincoln, NE, (2010).
- [151] K.-E. PEIPONEN AND E. M. VARTIAINEN, *Kramers-kronig relations in optical data inversion*, Phys. Rev. B, **44**, 8301 (1991).
- [152] J. MACK, M. J. STILLMAN, AND N. KOBAYASHI, *Application of MCD spectroscopy to porphyrinoids*, Coordin. Chem. Rev., **251**, 3 (2007).
- [153] M. FRONK, B. BRÄUER, J. KORTUS, O. G. SCHMIDT, D. R. ZAHN, AND G. SALVAN, *Determination of the Voigt constant of phthalocyanines by magneto-optical Kerr-effect spectroscopy*, Phys. Rev. B, **79**, 23 (2009).
- [154] J. ZAK, E. R. MOOG, C. LIU, AND S. D. BADER, *Magneto-optics of multilayers with arbitrary magnetization directions*, Phys. Rev. B, **43**, 6423 (1991).
- [155] T. HAIDER, *A review of magneto-optic effects and its application*, Int. J. Electrom. Appl., **7**, 17 (2017).
- [156] S. VISNOVSKY, *Optics in Magnetic Multilayers and Nanostructures*, CRC Press Taylor and Francis Group, Florida, 1st ed., (2006).
- [157] N. LEICK, J. W. WEBER, A. J. M. MACKUS, M. J. WEBER, M. C. M. VAN DE SANDEN, AND W. M. M. KESSELS, *In situ spectroscopic ellipsometry during atomic layer deposition of Pt, Ru and Pd*, J. Phys. D, **49**, 115504 (2016).
- [158] M. SCHUBERT, *Infrared Ellipsometry on Semiconductor Layer Structures*, Springer-Verlag Berlin Heidelberg, (2004).

BIBLIOGRAPHY

- [159] M. SCHUBERT, *Another century of ellipsometry*, Annal. Phys. (Le), **15**, 7-8 (2006).
- [160] M. SCHUBERT, *Generalized ellipsometry and complex optical systems*, Thin Solid Films, **313**, 323 (1998).
- [161] R. AZZAM AND N. BASHARA, *Ellipsometry and Polarized Light*, North-Holland Publ. Co., Amsterdam, (1984).
- [162] G. JELLISON, *Data analysis for spectroscopic ellipsometry*, Thin Solid Films, **234**, 416 (1993).
- [163] F. H, *Spectroscopic Ellipsometry - Principles and Applications*, John Wiley and Sons, New York, (2003).
- [164] B. JOHS AND J. S. HALE, *Dielectric function representation by B-splines*, Phys. Status Solidi A, **205**, 715 (2008).
- [165] J. W. WEBER, T. A. R. HANSEN, M. C. M. VAN DE SANDEN, AND R. ENGELN, *B-spline parametrization of the dielectric function applied to spectroscopic ellipsometry on amorphous carbon*, J. Appl. Phys., **106**, 123503 (2009).
- [166] E. KRÜGER, V. ZVIAGIN, C. YANG, C. STURM, R. SCHMIDT-GRUND, AND M. GRUNDMANN, *Temperature dependence of the dielectric function of thin film CuI in the spectral range (0.6–8.3) eV*, Appl. Phys. Lett., **113**, 172102 (2018).
- [167] D. LIKHACHEV, *Spectroscopic ellipsometry data analysis using penalized splines representation for the dielectric function*, Thin Solid Films, **669**, 174 (2019).
- [168] T. HERRMANN, K. LÜDGE, W. RICHTER, K. G. GEORGARAKIS, P. POULOPOULOS, R. NÜNTHEL, J. LINDNER, M. WAHL, AND N. ESSER, *Optical anisotropy and magneto-optical properties of Ni on pre-oxidized Cu (110)*, Phys. Rev. B, **73**, 134408 (2006).
- [169] W. LI, *Magneto-optical Kerr Effect Spectroscopy Study of Ferromagnetic Metal/Organic Heterostructures*, PhD thesis, Technische Universität Chemnitz, (2010).

- [170] D. SCHMIDT, T. HOFMANN, C. M. HERZINGER, E. SCHUBERT, AND M. SCHUBERT, *Magneto-optical properties of cobalt slanted columnar thin films*, Appl. Phys. Lett., **96**, 091906 (2010).
- [171] J. MACK AND N. KOBAYASHI, *Recent applications of MCD spectroscopy to porphyrinoids*, Pan Stanford, New York, 1st ed., (2012).
- [172] S. SCHNEIDER, S. B. PIEPHO, AND P. SCHATZ, *Group Theory in Spectroscopy With Applications to Magnetic Circular Dichroism: Wiley Interscience Monographs in Chemical Physics*, John Wiley and Sons, New York, (1984).
- [173] *User's Manual 7300 Series VSM System*, Lake Shore Cryotronics, Inc., (2001).
- [174] X. XU, A. SUN, X. JIN, H. FAN, AND X. YAO, *Method for calculating the induced voltage in a vibrating sample magnetometer detection coil system*, Rev. Sci. Instrum., **67**, 3914 (1996).
- [175] *Basic Laboratory Materials, Materials Science and Engineering, M106 Vibrating Sample Magnetometry*, (2016). Manual.
- [176] J. P. C. BERNARDS, *Design of a detection coil system for a biaxial vibrating sample magnetometer and some applications*, Rev. Sci. Instrum., **64**, 1918 (1993).
- [177] *PPMS Vibrating sample magnetometer*, <http://www.qdusa.com>. Application note.
- [178] J. LI, Y. JIANG, Y. LI, D. YANG, Y. XU, AND M. YAN, *Origin of room temperature ferromagnetism in MgO films*, Appl. Phys. Lett., **102**, 072406 (2013).
- [179] Y. ZHANG, J. HU, E. CAO, L. SUN, AND H. QIN, *Vacancy induced magnetism in SrTiO_3* , J. Magn. Magn. Mater., **324**, 1770 (2012).
- [180] M. CAO, Y. MA, X. WANG, C. MA, W. ZHOU, X. WANG, W. TAN, AND J. DU, *Point defects and magnetic properties of neutron irradiated MgO single crystal*, AIP Advances, **7**, 056413 (2017).
- [181] J. P. SINGH AND K. H. CHAE, *d^0 Ferromagnetism of Magnesium Oxide*, Condens. Matter, **2(4)**, 36 (2017).

BIBLIOGRAPHY

- [182] S. G. EBBINGHAUS, H. KRAUSE, D.-K. LEE, AND J. JANEK, *Single Crystals of C12A7 ($Ca_{12}Al_{14}O_{33}$) Substituted with 1 mol % Iron*, Cryst. Growth Des., **14**, 2240 (2014).
- [183] W. F. J. FONTIJN, P. J. VAN DER ZAAG, M. A. C. DEVILLERS, V. A. M. BRABERS, AND R. METSELAAR, *Optical and magneto-optical polar Kerr spectra of Fe_3O_4 and Mg^{2+} - or Al^{3+} -substituted Fe_3O_4* , Phys. Rev. B, **56**, 5432 (1997).
- [184] P. V. D. ZAAG AND W. FONTIJN, *A study of the magneto-optical Kerr spectra of bulk and ultrathin Fe_3O_4* , J. Appl. Phys., **79**, 5936 (1996).
- [185] V. ZVIAGIN, P. RICHTER, T. BÖNTGEN, M. LORENZ, M. ZIESE, D. R. ZAHN, G. SALVAN, M. GRUNDMANN, AND R. SCHMIDT-GRUND, *Comparative study of optical and magneto-optical properties of normal, disordered, and inverse spinel-type oxides*, Phys. Status Solidi B, **253**, 429 (2016).
- [186] A. TIMOPHEEV, A. AZEVEDO, N. SOBOLEV, K. BRACHWITZ, M. LORENZ, M. ZIESE, P. ESQUINAZI, AND M. GRUNDMANN, *Magnetic anisotropy of epitaxial zinc ferrite thin films grown by pulsed laser deposition*, Thin Solid Films, **527**, (2013).
- [187] H. YAO AND C. H. YAN, *Anisotropic optical responses of sapphire ($-Al_2O_3$) single crystals*, J. Appl. Phys., **85**, 6717 (1999).
- [188] SPENCER, CHARLES D. AND SCHROEER, DIETRICH, *Mössbauer study of several cobalt spinels using Co^{57} and Fe^{57}* , Phys. Rev. B, **9**, 3658 (1974).
- [189] J. D. HANAWALT, H. W. RINN, AND L. K. FREVEL, *Chemical analysis by X-ray diffraction*, Ind. Eng. Chem. Anal. Ed., **10**, 457 (1938).
- [190] E. LIŠKOVA-JAKUBISOVA, VIŠŇOVSKÝ, P. ŠIROKÝ, D. HRABOVSKÝ, J. PIŠTORA, S. C. SAHOO, S. PRASAD, N. VENKATARAMANI, M. BOHRA, AND R. KRISHNAN, *Nanocrystalline zinc ferrite films studied by magneto-optical spectroscopy*, J. Appl. Phys., **117**, 17 (2015).
- [191] C. HIMCINSCHI, I. VREJOIU, G. SALVAN, M. FRONK, A. TALKENBERGER, D. R. ZAHN, D. RAFAJA, AND J. KORTUS, *Optical and magneto-optical study of nickel and cobalt ferrite epitaxial thin films and submicron structures*, J. Appl. Phys., **113**, 8 (2013).

-
- [192] K. J. KIM, H. S. LEE, M. H. LEE, AND S. H. LEE, *Comparative magneto-optical investigation of $d-d$ charge-transfer transitions in Fe_3O_4 , $CoFe_2O_4$, and $NiFe_2O_4$* , J. Appl. Phys., **91**, 9974 (2002).
- [193] S. VISOVSKÝ, N. P. THUY, J. STEPANEK, V. PROSSER, AND R. KRISHNAN, *Magneto-optical spectra of $Y_3Fe_5O_{12}$ and $Li_{0.5}Fe_{2.5}O_4$ between 2.0 and 5.8 eV*, J. Appl. Phys., **50**, 7466 (1979).
- [194] S. VISNOVSKY, V. PROSSER, R. KRISHNAN, V. PARIZEK, K. NITSCH, AND L. SVOBODOVA, *Magneto-optical polar kerr effect in ferrimagnetic garnets and spinels*, IEEE Trans. Magn., **17**, 3205 (1981).
- [195] K. L. SALCEDO RODRÍGUEZ, S. J. STEWART, P. M. MENDOZA ZÉLIS, G. A. PASQUEVICH, AND C. E. RODRÍGUEZ TORRES, *Role of defects on the magnetic behaviour of the geometrically frustrated spinel $ZnFe_2O_4$* , J. Alloy. Compd., **752**, 289 (2018).
- [196] H. XIANG, F. SHI, M. S. RZCHOWSKI, P. M. VOYLES, AND Y. A. CHANG, *Epitaxial growth and magnetic properties of Fe_3O_4 films on TiN buffered $Si(001)$, $Si(110)$, and $Si(111)$ substrates*, Appl. Phys. Lett., **97**, 092508 (2010).
- [197] C. JIN, P. LI, W. MI, AND H. BAI, *Structure, magnetic, and transport properties of epitaxial $ZnFe_2O_4$ films: An experimental and first-principles study*, J. Appl. Phys., **115**, 213908 (2014).
- [198] H. YUAN, J. G. ZHENG, Y. YIN, E. LIU, Z. HUANG, Y. ZHAI, J. DU, AND H. ZHAI, *Effect of Zn substitution in (111)-textured $Zn_xFe_{3-x}O_4$ thin films on magnetization dynamics*, J. Alloy. Compd., **690**, 369 (2017).
- [199] M. ZIESE, R. HÖHNE, H. C. SEMMELHACK, H. RECKENTIN, N. H. HONG, AND P. ESQUINAZI, *Mechanism of grain-boundary magnetoresistance in Fe_3O_4 films*, Eur. Phys. J. B, **28**, 415 (2002).

List of article contributions

1. K. Mok, C. Scarlat, G. Kovacs, L. Li, V. Zviagin, J. McCord, M. Helm, and H. Schmidt, *Thickness independent magneto-optical coupling constant of nickel films in the visible spectral range*, J. Appl. Phys., **110**, 123110 (2011).
2. R. Schmidt-Grund, C. Kranert, H. v. Wenckstern, V. Zviagin, M. Lorenz, and M. Grundmann, *Dielectric function in the spectral range (0.5–8.5)eV of an $(Al_x Ga_{1-x})_2O_3$ thin film with continuous composition spread*, J. Appl. Phys., **117**, 165307 (2015).
3. V. Zviagin, P. Richter, T. Böntgen, M. Lorenz, M. Ziese, D. R. T. Zahn, G. Salvan, M. Grundmann, and R. Schmidt-Grund, *Comparative study of optical and magneto-optical properties of normal, disordered and inverse spinel type oxides*, Phys. Status Solidi B, **253**, 429 (2016).
4. V. Zviagin, Y. Kumar, I. Lorite, P. Esquinazi, M. Grundmann, and R. Schmidt-Grund, *Ellipsometric investigation of $ZnFe_2O_4$ thin films in relation to magnetic properties*, Appl. Phys. Lett., **108**, 131901 (2016)
5. M. Wille, E. Krüger, S. Blaurock, V. Zviagin, R. Deichsel, G. Benndorf, L. Trefflich, V. Gottschalch, H. Krautscheid, R. Schmidt-Grund, and M. Grundmann, *Lasing in cuprous iodine microwires*, Appl. Phys. Lett., **111**, 031105 (2017)
6. C. Sturm, R. Schmidt-Grund, V. Zviagin, and M. Grundmann, *Temperature dependence of the dielectric tensor of monoclinic Ga_2O_3 single crystals in the spectral range 1.0–8.5 eV*, Appl. Phys. Lett., **111**, 082102 (2017)
7. E. Krüger, V. Zviagin, C. Yang, C. Sturm, R. Schmidt-Grund, and M. Grundmann, *Temperature dependence of the dielectric function of thin film CuI in the spectral range (0.6–8.3) eV*, Appl. Phys. Lett., **113**, 172102 (2018)

List of article contributions

8. S. Prucnal, Y. Berencén, M. Wang, J. Grenzer, M. Voelskow, R. Hübner, Y. Yamamoto, A. Scheit, F. Bärwolf, V. Zviagin, R. Schmidt-Grund, M. Grundmann, J. Žuk, M. Turek, A. Drożdziel, K. Pyszniak, R. Kudrawiec, M. P. Polak, L. Rebohle, W. Skorupa, M. Helm, and S. Zhou, *Strain and band-gap engineering in Ge-Sn alloys via P doping*, Phys. Rev. Appl., **10**, 064055 (2018)
9. C. Sturm, V. Zviagin, and M. Grundmann, *Applicability of the constitutive equations for the determination of the material properties of optically active materials*, Opt. Lett., **44**, 1351 (2019)
10. V. Zviagin, P. Huth, M. Bonholzer, C. Sturm, A. Setzer, J. Lenzner, R. Denecke, P. Esquinazi, M. Grundmann, and R. Schmidt-Grund, and M. Grundmann, *Ferrimagnetic order in crystallographic surface and bulk spinel ferrite thin films ($Zn_xFe_{3-x}O_4$)*, manuscript submitted for publication (March 2019).

Selbstständigkeitserklärung

Hiermit versichere ich,

- dass die vorliegende Arbeit ohne unzulässige Hilfe und ohne Benutzung anderer als der angegebenen Hilfsmittel angefertigt wurde, und dass die aus fremden Quellen direkt oder indirekt übernommenen Gedanken in der Arbeit als solche kenntlich gemacht wurden;
- dass alle Personen in der Dissertation genannt wurden, von denen ich bei der Auswahl und Auswertung des Materials sowie bei der Herstellung des Manuskripts Unterstützungsleistung erhalten habe;
- dass keine weiteren Personen bei der geistigen Herstellung der vorliegenden Arbeit beteiligt waren;
- dass dritte Personen weder unmittelbar noch mittelbar geldwerte Leistungen für Arbeiten erhielten, die im Zusammenhang mit dem Inhalt der vorgelegten Dissertation stehen;
- dass die vorgelegte Arbeit weder im Inland noch im Ausland in gleicher oder in ähnlicher Form einer anderen Prüfungsbehörde zum Zwecke einer Promotion oder eines anderen Prüfungsverfahrens vorgelegt und in ihrer Gesamtheit noch nicht veröffentlicht wurde;
- dass keine früheren erfolglosen Promotionsversuche stattgefunden haben.

Mit meiner Unterschrift erkläre ich, dass ich die Promotionsordnung der Fakultät für Physik und Geowissenschaften der Universität Leipzig, in der Fassung vom 24. August 2016, und die obengennante Selbstständigkeitserklärung anerkenne.

Ort, Datum

Vitaly Zviagin

Acknowledgments

First and foremost, I would like to express my sincerest gratitude to Prof. Dr. Marius Grundmann for providing me with the opportunity to continue working with Spectroscopic Ellipsometry to investigate this interesting material in much greater detail. I realize that the time spent gathering information and going over my results has significantly strengthened the theories and patterns, which were only slightly probable in the beginning. Also for allowing me to go to interesting conferences, where exchange of knowledge and experiences were essential to this topic and other currently investigated phenomena.

I will be forever grateful to Dr. Rüdiger Schmidt-Grund for guiding me ever since my B. Sc., for nearly daily discussions and for inspiring me to explore alternative options whenever I reached a dead end or went off on a tangent.

I am also very grateful to Prof. Dr. Pablo Esquinazi for rather short, but very productive discussions, which led to significant improvements in the presented work.

Furthermore, I would like to express my gratitude to Prof. Dr. Reinhard Denecke for fruitful discussions and for acknowledging the potential in this topic.

I am very grateful to Anja Heck and Birgit Wendisch for taking care of everything related to the formalities and organizational procedures.

Also, I would like to thank Jörg Lenzner for prompt measurements and for technical support with the spectroscopic ellipsometer system. Holger Hochmuth for very quick production of various thin films, which accelerated this investigation significantly. Monica Hahn for substrate preparation and the treatment procedures.

Furthermore, I would like to thank the members of the optics group, Prof. Dr. Bernd Rheinländer, Chris Sturm, Oliver Herrfurth, Evgeny Krüger, Lukas Trefflich, it is a pleasure working with you and I can not imagine a more productive and close team. Also my office mates, Andreas Müller, Sebastian Henn, Ron Hildebrandt, Fabian Schöppach, for rather short but still positive interactions. Stefan Hohenberger for the coffee breaks. Furthermore, I would like to express

Acknowledgments

my gratitude to the rest of the HLP group members for countless interesting discussions, PGs, cooperation and support.

Additionally, I would like to thank the former group members Steffen Richter, Tammo Böntgen, Kerstin Brachwitz, Michael Bonholzer, Alexander Shkurmanov, Tom Michalsky, Marcel Wille, Martin Thunert, Christian Kranert, Krzysztof Dorywalski.

Also all the people who have contributed to this topic, Paula Huth, Peter Richter, Annette Setzer, Yogesh Kumar, Israel Lorite.

I also would like to thank B. Zagidullin, B. Zilinsky, M. v. Sach., I. Matyash, T. Pyrin, B. Semenenko, S. Rifalow, M. Pax, M. Msasi, J. Jama, I. Stewart, A. Kulykiv for their support and who in one way or another helped shape the results and theories presented in this work.

Last, but not least, I would like to thank my parents for their support and for guiding me, not only since the very beginning but also throughout this journey.

This work is within the framework of the Deutsche Forschungsgemeinschaft (DFG, German Research Foundation) – Projektnummer 31047526 – SFB 762, projects B1, B3, A7.